TUNNELLING CURRENT EXCITED ON-CHIP PLASMON SOURCE BASED ON PROTRUDED METAL INSULATOR METAL STRUCTURE

PHUA WEE KEE

NATIONAL UNIVERSITY OF SINGAPORE

2016

TUNNELLING CURRENT EXCITED ON-CHIP PLASMON SOURCE BASED ON PROTRUDED METAL INSULATOR METAL STRUCTURE

PHUA WEE KEE

(B.Eng. (Hons.), NTU)

A THESIS SUBMITTED

FOR THE DEGREE OF DOCTOR OF PHILOSOPHY
DEPARTMENT OF ELECTRICAL AND COMPUTER ENGINEERING
NATIONAL UNIVERSITY OF SINGAPORE

2016

DECLARATION

I hereby declare that this thesis is my original work and it has been written by me in its entirety. I have duly acknowledged all the sources of information which have been used in the thesis.

This thesis has also not been submitted for any degree in any university previously

Phua Wee Kee
28th October 2016

Acknowledgements

It has been a long but exciting journey for me throughout these years as I sought greater knowledge and learned a lot more about the subject area of plasmonics. I would not have been where I am now without the selfless help of all those around me who did not hesitate to provide me with guidance and advice throughout all my years of studies.

First and foremost I would like to thank all my colleagues at the Institute of High Performance Computing (IHPC), particularly colleagues from Electronics and Photonics (EP) department and in the NanoPhotonics and Plasmonics (NPP) capability group, most notably Dr. Koh Wee Shing, Dr. Wu Lin, Dr. Yuriy Akimov, Dr. Chu Hong son, Dr. Khoo Eng Huat and Dr. Hor Yew Li who have provided me with invaluable advice, encouragement, and most importantly opportunities for me to shine and contribute during our daily interactions and discussions. I would also like to thank Dr. Jason Png Ching Eng, EP's department director for always believing in me and putting trust and faith in my abilities, always providing me with new opportunities to learn and grow. Apart from colleagues in IHPC, I would like to thank my experimental collaborators from Prof. Christian A. Nijhuis's group in NUS and Dr. Liu Yan Jun and Dr. Eunice Leong in IMRE.

Next I would like to thank my lunch buddies in IHPC for always being very friendly, kind and supportive, lending a listening ear when I'm down, supporting me whenever there's a need and providing me with a very conducive environment to work in. They include Dr. Tandiono, Dr. Geraldine Lim Song Len, Dr. Ong Jun Rong, Dr. Thomas Ang and Dr. Lee Hui Min.

Every discussion and chit chat sessions during lunch always provided me with an opportunity to de-stress and clear my mind from clutter.

While my companions at work provide me with a source of support, I would like to show my deepest appreciation and gratitude to my main supervisor Dr. Aaron Danner, my co-supervisor Dr. Bai ping and my ex main supervisor Dr. Dan Pickard for always being there for me, for providing me directions when I was lost and for lending a listening ear when I faced problems in my research. Without their guidance and great tolerance for my ignorance, I would not have reached where I am now.

Lastly, I would like to thank my family and all my close friends for always being very supportive of my decision to pursue further studies, to be understanding whenever I placed greater emphasis on studies resulting in less bonding time. I really appreciate their encouragements whenever I met obstacles along the way, knowing that I can bravely continue on my journey in the quest for greater knowledge with them supporting me from behind.

Very hearty thanks to all others who have helped me in one way or another. I really appreciate all your kind help and effort and would definitely strive to be a great researcher so as not to let all of you down.

Table of Contents

Summary

Recent technologies lean towards low cost, high speed, lightweight and compact devices. This is particularly true for nanoscale optoelectronic integrated circuits with applications in on-chip data communications. While scaling has been possible for most of the components necessary for optoelectronic integrated circuits, the achievement of a compact light source suitable for plasmonic applications remains challenging. Often such sources require small device footprints, high efficiency, low power inputs, ease of fabrication, high directionality and tunable operating wavelengths. This thesis is related to the construction of such a compact light source.

A compact tunable source of plasmon polaritons based on a protruded metal-insulator-metal (pMIM) structure has been proposed. The pMIM structure consists of a protruded segment and a metal-insulator-metal (MIM) waveguiding segment. The protruded tip forms a nanometre gap and allows a low voltage bias to generate a localised tunnelling current. This tunnelling current excites plasmon polaritons which can be coupled onto an MIM waveguiding segment which has a much larger gap than the tip gap. As such, the excited plasmon polaritons are able to propagate a long distance which is a key feature of this source, and is challenging to achieve.

The protruded tip enhances the total amount of emitted power from the tunnelling current while the tip's profile enhances the coupling efficiency of excited plasmon polaritons from the protruded segment to the MIM waveguiding segment. From a range of possible practical tip profiles with different contact areas and slope gradients, the concave tip profile is seen to exhibit the highest coupling efficiency.

By applying a voltage bias, the protruded tip will excite eigenwaves which can be coupled to the MIM waveguiding segment to form long propagating surface plasmon-polaritons (SPPs). Among all excited modes, the single and dual mode operation allows highly efficient excitation of long travelling SPPs with propagation length of up to 30 μm. In order to use such pMIM structures for on-chip applications, the metal substrate has to be relatively thin and undesired leakage radiation could arise. For an Au-SiO_2-Au pMIM structure, the Au thickness should be larger than 100 nm. Working with experimental collaborators, the undesired leakage radiation can be used to detect excited propagating SPPs in practical pMIM structures.

To achieve an ideal highly directional on-chip source, the protruded segment was manipulated to implement asymmetric directivity by harnessing excited surface eigenmodes on a metal nanostructure placed below the protruded tip, forming a double protruded metal-insulator-metal (p^2MIM) structure. There exists a correlation between surface eigenmodes excited by tunnelling current with the circular dichroism (CD) signature of optically excited nanostructures. Using the plasmon hybridisation method as a tool, excited surface eigenmodes on basic and complex nanostructures can be predicted, allowing for the design of a nanostructure that can create a desired surface eigenmode profile which induces asymmetric directivity.

The electrical excitation of SPPs using pMIM and p^2MIM structures opens up the possibility of integrating plasmon sources onto nanoscale optoelectronic integrated circuits to facilitate on-chip data communications, and these structures have shown significant promise as a result of the work shown in this thesis.

List of Figures

List of Symbols

a: atto (10^{-18})
$a_{grating}$: Period of grating
A_n: Decomposition coefficient
β: Wavevector in propagation direction
$\bar{B}$: Magnetic flux density/Magnetic induction
c: Speed of light
dVol: Differential volume
$\bar{D}$: Electric displacement field
ξ: Coupling
ε: Permittivity of material
ε_d: Permittivity of dielectric
ε_m: Permittivity of metal
$\varepsilon_{medium}(\varepsilon_1/\varepsilon_2)$: Permittivity of material in medium 1 or 2
ε_0: Permittivity of free space
ε_r: Relative permittivity/dielectric constant of material
E; ħω: Energy
$\bar{E}$: Electric field
E_{loss}: Energy lost by penetrating electrons
f: femto (10^{-15})
$g_{grating}$: Reciprocal vector of grating
h: Planck's constant
$\hbar$: Reduced Planck's constant
$\bar{H}$: Magnetic field
H_{int}: Interaction energy
I: Integrated power flux
I_n: Integrated power flux for the eigenfields
I_0: Integrated power flux for excited electromagnetic fields
$\bar{J}$: Electric current density
Δk: Change in wavevector
k: Wavevector
k_{inc}: Wavevector in incident medium along direction of incident excitation
k_0: Wavevector in free space
k_p: Wavevector in plasma
k_{scat}: Wavevector along direction of scattered electrons
k_{SPP}: Wavevector of excited SPPs
k_x: Wavevector along the x direction
source (EM wave/penetrating electrons)
L_{eff}: Effective propagation length
m_e: Mass of each electron
$\bar{M}$: Magnetisation density
$\hat{n}$: Unit vector
n: Density of conduction electrons
n_{eff}: Effective mode index/normalised propagation constant
$n_{eff}{}'$: Real part of effective mode index
$n_{eff}{}''$: Imaginary part of effective mode index
n_{medium}: Refractive index of medium

θ_{inc}: Angle along direction of incident excitation source (EM wave/penetrating electrons)
θ_{scat}: Angle along direction of scattered electrons away from normal
p: Dipole moment
ρ: Electric charge density
$\bar{p}$: Momentum
$\bar{P}$: Polarisation density
P(ω): Power
P_{loss}: Probability of energy loss
$q; e$: Charge of each electron
S_{rn}: Time average poynting vector in radial direction for eigenfields with mode number n
$S_{r\emptyset}$: Time average poynting vector in radial direction for excited eigenwaves
μ_0: Permeability of free space
μ_r: Relative permeability of material
μ: Permittivity of material
v_{eff}: Effective propagation speed
V: Voltage bias
Vol: Volume
ω: Angular frequency
ω_{SPP}: Angular frequency of excited SPPs
ω_p: Plasma frequency
γ: Interaction index
γ_g: Damping constant; electron scattering rate (inverse of collision time for conduction electrons)
λ_{eff}: Effective wavelength
λ_{inc}: Wavelength of incident excitation source (EM wave/penetrating electrons)
λ_{SPP}: Wavelength of excited SPPs
z: zepto (10^{-21})

List of Abbreviations

Al: Aluminium
Al_2O_3: Aluminium Oxide
Ag: Silver
ATR: Attenuated total reflection
Au: Gold
CCD: Charge coupled device
CD: Circular dichroism
CMOS: Complementary metal-oxide-semiconductor
Cu: Copper
DT: Direct tunnelling
EELS: Electron energy loss spectroscopy
EGaIn: Eutectic Gallium Indium
EM: Electromagnetic
EMCCD: Electron multiplying CCD
Fc: Ferrocenyl
FDTD: Finite-difference time-domain
FEM: Finite element method
F.T: Fourier transform
FWHM: Full width half maximum
HOMO: Highest occupied molecular orbital
IM: Insulator-metal
IMI: Insulator-metal-insulator
LCP: Left handed circularly polarised
LED: Light emitting diode
LSP: Localised SPPs
LSPR: Localised surface plasmon resonance
LUMO: Lowest unoccupied molecular orbital
MIM: Metal-insulator-metal
Ni: Nickel
NIR: Near infra-red
OA: Optical adhesive
OLED: Organic light emitting diode
PDMS: Polydimethylsiloxane
pMIM: Protruded metal-insulator-metal
p^2MIM: Double protruded metal-insulator-metal
PML: Perfectly matched layer
Pt: Platinum
RCP: Right handed circularly polarised
SAM: Self assembled monolayer
SC_n: $S(CH_2)_{n-1}CH_3$
Si_3N_4: Silicon Nitride
SiO_2: Silicon dioxide
S-OPE-Fc: (4-((4-(ferrocenyl)phenyl)ethynyl)phenyl)methanethiol
SPP: Surface plasmon polariton
ST: Sequential tunnelling
STM: Scanning tunnelling microscopy
TE: Transverse electric

TEM: Transmission electron microscope
TM: Transverse magnetic
TMM: Transfer matrix method
TIR: Total internal reflection
UV: Ultraviolet
VIS: Visible

Chapter 1. Introduction

1.1. Background

Continuous downward scaling of semiconductor technologies has been prompted by an ever increasing demand for efficient electronic devices with smaller dimensions and reduced propagation delays, allowing for faster information transfer. Bottlenecks, however are presented by electrical interconnects in electrical circuits, thereby limiting operation to less than 10 GHz [1.1, 1.2]. To resolve this limitation, prospects lie in the combination of electrical and optical devices, making use of optical devices to provide superior operational bandwidth [1.3, 1.4] and data transmission capabilities. Photons have very little interaction with their surrounding environment [1.5], which is the primary reason that bandwidth can be greater, along with the fact that commonly used frequencies are so high that modulation bandwidths can theoretically be much higher than the use of electrons in electronic circuits.

So-called optoelectronic integrated circuits make use of the best of optics and electronics. In optoelectronic integrated circuits [1.6], electrical signals are converted into digital light signals for data transmission at the transmitting end of the data buses. At the receiving end of the data buses, the light containing digital information is converted back to electrical signals, thereby ramping up the speed and accuracy of information transfer.

Optical device dimensions, however, are limited by the law of diffraction, resulting in an incompatibility between nanometre scale

electronics and micrometre scale photonics elements. Such incompatibility paves the way for the emergence of plasmonics which merges the high bandwidth offered by photonics and the nanoscale integration offered by nanoelectronics [1.7], particularly in the area of integrated circuits. Plasmonics applications [1.8] in optoelectronic integrated circuits, in a broad sense, involve the ability to make use of plasmon polaritons which are collective charge oscillations formed by coupling the photon energy with the free electron gas. These plasmon polaritons capture and confine light in nanostructures which can then be coupled out using waveguiding structures as a medium of communication. One key attribute of the use of plasmon polaritons in interconnects is that they are able to surpass the speed limitation of electrical interconnects once translation between electrical and plasmonic signals is possible.

1.2. Motivation

With the exception of a compact light source, downwards scaling has been possible for most optical components necessary for optoelectronic integrated circuits, including waveguides [1.9-1.12], modulators [1.13-1.15] and detectors [1.8, 1.16-1.18]. Optical components such as these photonics devices allow for faster information transfer and higher operation bandwidth but they are of sizes limited by the laws of diffraction. One way to scale these photonics devices is to make use of plasmon polaritons to bridge the difference in size between nanometer scale electronics and micrometer scale photonic elements. While plasmon polaritons present a solution to downscale these optical devices, there is a challenge in scaling the optical source, which is the reason for the proposed electrically excited plasmon source. The design of this source is critical, and is the main body of work in this thesis.

Plasmon sources [1.19, 1.20] make use of surface plasmon polaritons (SPPs). SPPs are actually true surface eigenmodes [1.21, 1.22] that occur at the interfaces of metals and dielectrics and they are able to confine light in subwavelength dimensions, thereby allowing plasmon sources to serve as compact light sources.

While the excitation of surface plasmon polaritons by external light sources at metal interfaces has been widely studied and fairly well understood, the advantages of plasmon polaritons can only be truly exploited by integrating them on a single chip. Current methods of plasmon generation using optical means inherently limit the use of plasmon polaritons in optoelectronic integrated circuits.

In order to create a compact light source, plasmonics has to be integrated with existing electronics to create a device that is able to facilitate direct electrical excitation as a means to generate plasmon polaritons on-chip, as opposed to that requiring external excitation [1.23, 1.24]. Further, with lasers being the brightest sources of high frequency electromagnetic radiation, lasers built from plasmon sources could ultimately enable the exploration of nanometre-scale science and applications geared towards deep subwavelength optics for the development of high performance devices [1.25].

Electrically excited plasmon sources can be configured in the form of scanning tunnelling microscopy (STM) [1.26-1.30], transmission electron microscopy (TEM) [1.31-1.33], organic light emitting diodes (OLEDs) [1.34], semiconductor LEDs [1.9, 1.35-1.36], silicon nanocrystals [1.37], semiconductor nanowires [1.38, 1.39], semiconductor quantum cascaded laser [1.40] and quantum well hybrid structures [1.41, 1.42]. Of the state of the art electrically excited plasmon sources studied prior to this work, the simplest structure is the metal insulator metal (MIM) structure. The MIM structure however, has very thin insulating structures which are necessary to generate plasmon polaritons, but which impedes propagation length.

Many other recent electrically excited plasmon source designs also face technical problems which include their inability to meet low power consumption and small size requirements, complexity of fabrication, inefficiency of plasmon polariton generation, low out coupling efficiency, uncontrollable directionality of the excited plasmon polaritons and too-short propagation lengths due to heavy damping. It is hence difficult to translate electrically excited plasmon sources to practical applications involving

optoelectronics integrated circuits. Low melting temperatures of materials such as OLEDs also serve as an impediment.

Optoelectronic integrated circuits are often compact with various components sharing the same power source, leading to low power requirements that serve as a limitation for plasmon polariton generation. Power and size limitations pose different challenges involving the redesign of existing structures which would allow electrical excitation and structures which have the potential to be scaled down.

In this thesis, the protruded MIM structure was proposed, which addresses many of these challenges, including low input power, generation and outcoupling efficiency, and controllability of the directionality of the excited plasmon polaritons.

1.3. Thesis outline

The main objective to be achieved from this study is to design a compact, efficient and tunable on-chip plasmon source for data communications in nanoscale optoelectronic integrated circuits. To achieve this objective, Chapter 1 will review the background and motivation behind the need for such an on-chip plasmon source. To design such a plasmon source, a brief review of plasmons and plasmon polaritons is given in Chapter 2, including surface and volume plasmon polaritons. Recent advances and current state of the art in the design of plasmon sources are also discussed, either via optical or electrical excitations in the form of an electron beam or a tunnelling current. The relevance of electrical excitation as an avenue for on-chip sources in optoelectronic integrated circuits is investigated as well.

From the current state of the art, MIM structures align most closely with the requirement for an electrically excited an on-chip plasmon source but it limits propagation distances of plasmon polaritons due to the thinness of the insulator. In Chapter 3, a compact and tunable source of plasmon polaritons is proposed based on a protruded metal-insulator-metal (pMIM) structure which consists of a protruded tip segment and a metal-insulator-metal (MIM) waveguiding segment. Emitted power from the tunnelling current generated in the protruded tip segment excites plasmon polaritons. To enhance this emitted power, different rectangular, convex, triangular and concave tip profiles are investigated. To tune the resonant peaks of this emitted power, the gap thickness at the tip is also studied. Since excited plasmon polaritons have to be

coupled from the protruded tip segment to the MIM waveguiding segment, the coupling efficiency is investigated as well.

In Chapter 4, the excited eigenwaves in the MIM waveguiding segment are studied. These eigenwaves are made up of different intrinsic eigenmodes. The various eigenmodes that can be supported are identified and classified into different operating regimes with various cut-off energies. Using a theoretical formulation to decompose the excited eigenwaves into the individual eigenmodes, long travelling plasmon polaritons can be identified and excited with high efficiencies. To adopt the proposed pMIM structure for use in on-chip applications, the metal thickness is investigated in Chapter 5. The limited thickness results in leakage radiation which is not desired since it reduces the plasmon polaritons' propagation length. The leakage radiation detection method is described and various metal thicknesses are studied to investigate the minimum allowable metal thickness with negligible leakage radiation. While leakage radiation is not desired, it can be used as a means to detect excited plasmon polaritons for pMIM structures.

A preliminary experimental study is conducted by experimental collaborators on the proposed pMIM design in Chapter 6. Practical materials are selected for the pMIM structure to aid the experimental fabrications. To detect excited plasmon polaritons from the pMIM structure, real and back focal plane images are examined. Using a proposed theoretical formalism, the leakage radiation spectra can be linked to the excitation of propagating SPPs.

pMIM structures allow symmetric directivity of highly efficient plasmon polaritons and provide a basis for the design of an ideal plasmon source which is highly directional. This symmetric directivity can be improved

to obtain asymmetric directivity in chapter 7, where the protruded segment is manipulated by placing a metal nanostructure below the protruded tip to form a double protruded metal-insulator-metal (p^2MIM) structure. The tunnelling current generated at the protruded tip excites surface eigenmodes on the metal nanostructure. The profile of these surface eigenmodes affects the dominant propagation direction of the excited plasmon polaritons in the MIM waveguiding segment. The profile of these surface eigenmodes excited by a tunnelling current can be correlated with the circular dichroism (CD) signature of nanostructures which are excited optically. This correlation allows the surface eigenmode profile on basic circular, triangular, square and rectangular nanostructures to be predicted using the plasmon hybridisation theory. This theory can be further extended to predict surface eigenmode profiles in complex nanostructures such as the gammadion nanostructure.

The main finding from this work is that electrical excitation of SPPs using pMIM and p^2MIM structures are indeed possible and can be used as a basis of design for a compact, efficient and tunable on-chip plasmon source for data communications in nanoscale optoelectronic integrated circuits. Apart from these findings, much work remains to be done to advance the field of on-chip plasmon sources which is also discussed.

1.4. Original contributions

The original contributions of the research are summarised as follows:

1. ***Designed a protruded MIM (pMIM) structure to excite long propagating surface plasmon polaritons.***

   By applying a low voltage bias, the protruded tip of the pMIM generates a tunnelling current which excites plasmon polaritons and couples them onto a metal-insulator-metal (MIM) waveguiding segment. These coupled plasmon polaritons propagate a longer distance of up to 30 μm due to the thick insulator layer in the MIM waveguiding segment as compared to the gap separation under the protruded tip . The protruded tip profile can be modified to enhance the emitted power from the tunnelling current. The concave tip mimics the ideal long and narrow tip profile most closely and enhances emitted power most.

2. ***Proposed an efficient approach to excite long travelling plasmon polaritons by identifying the contribution of each excited eigenmode in the MIM waveguiding segment.***

   The MIM waveguiding segment supports different eigenmodes with varying applied voltage bias. By identifying the contribution of each individual eigenmodes via decomposition of excited eigenwaves, the applied bias voltage can be controlled to excite long travelling surface plasmon polaritons with high efficiency, particularly in the single and dual mode operation regime.

3. ***Proposed guidelines for finite metal thicknesses of pMIM structures for on-chip applications and the use of leakage radiation to detect excited plasmon polaritons.***

   Leakage radiation arises when the metal substrate thickness is reduced beyond a critical value. For on-chip applications, this leakage radiation is undesired. For a Au-SiO_2-Au pMIM structure, leakage radiation remains negligible when the bottom Au substrate is larger than 150% of the skin depth of Au. Detected leakage radiation can be used to account for excited plasmon polaritons.

4. ***Designed a double protruded metal-insulator-metal (p^2MIM) structure to improve the directivity of excited plasmon polaritons.***

   In pMIM, the protruded tip acts as a localised source which excites plasmon polaritons with symmetric directivity. By placing metal nanostructures below the protruded tip segment to form the p^2MIM, excited surface eigenmode profile on these metal nanostructures could control the direction of the outwards propagating plasmon polaritons, thereby achieving asymmetric directivity. These surface eigenmode profiles can be predicted by using a correlation established between surface eigenmodes excited by the tunnelling current and the circular dichroism signature of the nanostructures.

1.5. Publications

1. W.S. Koh, C.H. Gan, **W.K. Phua**, Y.A. Akimov and P. Bai, "The potential of graphene as an ITO replacement in organic solar cells: An optical perspective", IEEE Journal of selected topics in quantum electronics, 20(1), 36-42 (2014)
2. **W.K. Phua**, Y.L. Hor, E.S.P. Leong, Y.J. Liu and E.H. Khoo, "Study of circular dichroism modes through decomposition of planar nanostructures", Plasmonics, 1-9 (2015)
3. E.S.P. Leong, J. Deng, E.H. Khoo, S.J. Wu, **W.K. Phua** and Y.J. Liu, "Fabrication of suspended, three-dimensional chiral plasmonic nanostructures with single-step electron beam lithography", RSC Advances, 5(117), 96366-96371 (2015)
4. E.H. Khoo, E.S.P. Leong, S.J. Wu, **W.K. Phua**, Y.L. Hor and Y.J. Liu, "Effects of asymmetric nanostructures on the extinction difference properties of actin biomolecules and filaments", Scientific reports, 6, 19658 (2016)
5. W. Du, T. Wang, H.S. Chu, L. Wu, R. Liu, S. Sun, **W.K. Phua**, L. Wang, N. Tomczak and C.A. Nijhuis, "On-chip molecular electronic plasmon sources based on self-assembled monolayer tunnel junctions", Nature Photonics, 10(4), 274-280 (2016)
6. Y.L. Hor, **W.K. Phua** and E.H. Khoo, "Chirality switching via rotation of bilayer fourfold meta-structure", Plasmonics, 1-5 (2016)
7. **W.K. Phua**, Y. Akimov, L. Wu, H.S. Chu, P. Bai and A. Danner, "Highly efficient tunable and localised on-chip electrical plasmon

source using protruded metal-insulator-metal structure", Optics Express, 24(10), 10663-10674 (2016)

8. **W.K. Phua**, Y. Akimov, L. Wu, H.S. Chu, P. Bai and A. Danner, "Diagnosis of localised and propagating surface plasmon polaritons generated in pMIM structures", In preparation (2016)

9. **W.K. Phua**, E.H. Khoo and A. Danner, "Creating circular dichroism inversion in basic nanostructures via rotation", In preparation (2016)

1.6. References

[1.1] H. Grabinski, *Interconnects in VLSI Design*, 222 (Springer Science and Business Media, 2012)

[1.2] S. Mishra, N.K. Chaudhary and K. Singh, "Overview of optical interconnect technology", 3(4) (2013)

[1.3] E. Ozbay, "Plasmonics: Merging photonics and electronics at nanoscale dimensions", Science, 311, 189-193 (2006)

[1.4] M.J. Kobrinsky, B.A. Block, J.F. Zheng, B.C. Barnett, E. Mohammed, M. Reshotko, F. Robertson, S. List, I. Young, and K. Cadien, "On chip optical interconnects", Intel Technology Journal, 8, 129-141 (2004)

[1.5] T.E. Northup and R. Blatt, "Quantum information transfer using photons", Nature Photonics, 8(5), 356-363 (2014)

[1.6] O. Wada, *Optoelectronics Integration: Physics, technology and applications* (Springer)

[1.7] S.A. Maier, *Plasmonics: Fundamentals and Applications* (Springer, 2007)

[1.8] O. Benson, "Assembly of hybrid photonic architectures from nanophotonic constituents," Nature, 480(7376), 193–199 (2011).

[1.9] P. Neutens, L. Lagae, G. Borghs and P.V. Dorpe, "Electrical excitation of confined surface plasmon polaritons in metallic slot waveguides", Nano letters, 10, 1429-1432 (2010)

[1.10] M.P. Nielsen, L. Lafone, A. Rakovich, T.P.H. Sidiropoulos, M. Rahmani, S.A. Maier and R.F. Oulton, "Adiabatic nanofocusing in hybrid gap plasmon waveguides on the silicon-on-insulator platform", Nano Letters, 16(2), 1410-1414 (2016)

[1.11] I. Goykhman, B. Desiatov and U. Levy, “Experimental demonstration of locally oxidised hybrid silicon-plasmonic waveguide”, Applied Physics Letters, 97(141106), 1-4 (2010)

[1.12] Z. Han, A.Y. Elezzabi and V. Van, “Experimental realisation of subwavelength plasmonic slot waveguides on a silicon platform” Optics Letters, 35(4), 502-504 (2010)

[1.13] A.L. Koh, K. Bao, I. Khan, W.E. Smith, G. Kothleitner, P. Nordlander, S.A. Maier and D.W. McComb, “Electron energy loss spectroscopy of surface plasmons in single silver nanoparticles and dimers”, ACS Nano, 3, 10, 3015 (2009)

[1.14] A. Melikyan, L. Alloatti, A. Muslija, D. Hillerkuss, P.C. Schindler, J. Li, R. Palmer, D. Korn, S. Muehlbrandt, D. Van Thourhout, B. Chen, R. Dinu, M. Sommer, C. Koos, M. Kohl, W. Freude and J. Leuthold, “High speed plasmonic phase modulators”, Nature Photonics, 8, 229-233 (2014)

[1.15] A. Melikyan, N. Lindenmann, S. Walheim, P.M. Leufke, S. Ulrich, J. Ye, P. Vincze, H. Hahn, T. Schimmel, C. Koos, W. Freude and J. Leuthold, “Surface plasmon polariton absorption modulator”, Optics Express, 19(9), 8855-8869 (2014)

[1.16] M.W. Ryu, J.S. Lee, K.S. Kim, K. Park, J.R. Yang, S.T. Han and K.R. Kim, “High performance plasmonic THz detector based on asymmetric FET with vertically integrated antenna in CMOS technology”, IEEE Transactions on electron devices, 63(4), 1742-1748 (2016)

[1.17] T. Watanabe, S.B. Tombet, Y. Tanimoto, Y. Wang, H. Minamide, H. Ito, D. Fateev, V. Popov, D. Coquillat, W. Knap, Y. Meziani and T.

Otsuji, “Ultrahigh sensitive plasmonic terahertz detector based on an asymmetric dual-grating gate HEMT structure”, Solid state electronics, 78, 109-114 (2012)

[1.18] J. Rosenberg, R.V. Shenoi, T.E. Vandervelde, S. Krishna and O. Painter, “A multi-spectral and polarisation-selective surface plasmon resonant mid infrared detector”, Applied Physics, 95, 161101 (2009)

[1.19] C.S. Kim, I. Vurgaftman, R.A. Flynn, M.Kim, J.R. Lindle, W.W. Bewley, K. Bussmann, J.R. Meyer, and J.P. Long, “An integrated surface-plasmon source,” Opt. Express, 18(10), 10609–10615 (2010).

[1.20] T. Aihara, H. Sakai, A. Takeda, S. Okahisa, M. Fukuhara, M. Ota, Y. Ishii and M. Fukuda, “Coherent plasmonic interconnection in silicon based electrical circuit,” J. Lightwave Technol., 33(10), 2139–2145 (2015).

[1.21] A. Kubo, K. Onda, H. Petek, Z. Sun, Y.S. Jung and H.K. Kim, “Femtosecond imaging of surface plasmon dynamics in a nanostructured silver film,” Nano Letters, **5**(6), 1123–1127 (2005)

[1.22] U. Hohenester and J. Krenn, “Surface plasmon resonances of single and coupled metallic nanoparticles: A boundary integral method approach,” Physical Review B, **72**(19), 195429 (2005)

[1.23] V. Giannini, A.I. Fernandez-Dominguez, S.C. Heck and S.A. Maier, “Plasmonic nanoantennas: Fundamentals and their use in controlling the radiative properties of nanoemitters”, Chemical Reviews, 111, 3888-3912 (2011)

[1.24] M. Bashevoy, F. Jonsson, A.V. Krasavin, N.I. Zheludev, Y. Chen and M.I. Stockman, “Generation of travelling surface plasmon waves by free electron impact”, Nano Letters, 6(6), 1113-1115 (2006)

[1.25] R.M. Ma, R.F. Oulton, V.J. Sorger and X. Zhang, “Plasmon lasers: Coherent light source at molecular scales”, Laser and photonics reviews, 1-12 (2012)

[1.26] I.I. Smolyaniov, M.S. Khaikin and V.S. Edelman, “Light emission from the tunnelling junction of the scanning tunnelling microscope”, Physics Letters A, 149, 7, 410-412 (1990)

[1.27] J. Aizpurua, A.P. Apell and R. Berndt, “Role of tip shape in light emission from the scanning tunnelling microscope”, Physical review B, 62, 3, 2065 (2000)

[1.28] J. Chen, M. Badioli, P. Alonso-González, S. Thongrattanasiri, F. Huth, J. Osmond, M. Spasenović, A. Centeno, A. Pesquera, P. Godignon and A.Z. Elorza, “Optical nano-imaging of gate tunable graphene plasmons”, Nature Letters, 487(7405), 77-81 (2012)

[1.29] Z. Fei, A.S. Rodin, G.O. Andreev, W. Bao, A.S. McLeod, M. Wagner, L.M. Zhang, Z. Zhao, M. Thiemens, G. Dominguez, M.M. Fogler, A.H. Castro Neto, C.N. Lau, F. Keilmann, and D.N. Basov, “Gate-tuning of graphene plasmons revealed by infrared nano-imaging,” Nature, 487(7405), 82–85 (2012)

[1.30] P. Bharadwaj, A. Bouhelier and L. Novotny, “Electrical excitation of surface plasmons”, Physical Review Letters, 106(22), 226802 (2011)

[1.31] P. Das, A. Kedia, P.S. Kumar, N. Large and T.K. Chini, “Local electron beam excitation and substrate effect on the plasmonic

response of single gold nanostars", Nanotechnology, 24(40), 405704 (2013)

[1.32] W. Cai, R. Sainidou, J. Xu, A. Polman and F.J.G. de Abajo, "Efficient generation of propagating plasmons by electron beams", Nano Letters, 9(3), 1176-1181 (2009)

[1.33] S. Liu, M. Hu, Y. Zhang, Y. Li and R. Zhong, "Electromagnetic diffraction radiation of a subwavelength hole array excited by an electron beam", Physical Review E, 80, 036602 (2009)

[1.34] D.M. Koller, A. Hohenau, H. Ditlbacher, N. Galler, F. Reil, F.R. Aussenegg, A. Leitner, E.J.W. List and J.R. Krenn, "Organic plasmon-emitting diode", Nature Photonics Letters, 2, 684 (2008)

[1.35] L. Wang, T. Li, L. Li, W. Xia, X.G. Xu and S.N. Zhu, "Electrically generated unidirectional surface plasmon source", Optics Express, 20(8), 8710-8717 (2012)

[1.36] K.C.Y. Huang, M.K. Seo, T. Sarmiento, Y. Huo, J.S. Harris and M.L. Brongersma, "Electrically driven subwavelength optical nanocircuits", Nature Photonics, 8, 244–249 (2014)

[1.37] R.J. Walters, R.V.A. van Loon, I. Brunets, J. Schmitz and A. Polman, "A silicon based electrical source of surface plasmon polaritons", Nature Materials, 9, 21 (2009)

[1.38] P. Fan, C. Colombo, K.C. Huang, P. Krogstrup, J. Nygård, I. Fontcuberta, A. Morral and M.L. Brongersma, "An electrically-driven GaAs nanowire surface plasmon source", Nano Letters, 12, 4943-4947 (2012)

[1.39] Y.S. No, J.H. Choi, H.S. Ee, M.S. Hwang, K.Y. Jeong, E.K. Lee, M.K. Seo, S.H. Kwon and H.G. Park, “A double-strip plasmonic waveguide coupled to an electrically driven nanowire LED”, Nano letters, 13, 772-776 (2013)

[1.40] A. Babuty, A. Bousseksou, J.P. Tetienne, I.M. Doyen, C. Sirtori, G. Beaudoin, I. Sagnes, Y. De Wilde and R. Colombelli, “Semiconductor surface plasmon sources”, Physical Review Letters, 104(22), 226806 (2010)

[1.41] J. Li, H. Shen, X. Dong, Y. Zhang, Z. Zhao, X. Duan and X. Meng, “Electrical excitation of surface plasmon polaritons using an Au ring grating/GaAs quantum well coupling structure”, Plasmonics, 10(1), 145-149 (2015)

[1.42] J. Li, H. Wei, H. Shen, Z.X. Wang, Z.S. Zhao, X.M. Duan and H.X. Xu, “Electrical source of surface plasmon polaritons based on hybrid Au-GaAs QW structures”, Nanoscale, 5, 8494–8499 (2013)

Chapter 2. Excitation of plasmon polaritons

2.1. Introduction

To excite plasmon polaritons, one has to match the wavevector of the incident excitation source with the wavevector of the plasmon polaritons. Here, methods of plasmon polariton excitation are reviewed. These include optical excitations usually in the form of an external laser or TM polarised electromagnetic wave and electrical excitations in the form of electron beams. From the different methods detailed, electrical excitation has been identified to have the most potential in creating a source of excited plasmon polaritons that can take on the role of a compact light source in optoelectronic integrated circuits. The use of electrical excitation allows the on-chip plasmon source to draw current from the same power supply as that of the other components in the circuits. Since the plasmon source is to be integrated on-chip, the power requirements should be very low as well. The power supply voltage requirement for a typical electronic integrated circuit is around 1.8 volts to 3.3 volts for 0.18 μm technology [2.1, 2.2].

It is however hard to realise such electrical excitation since low power requirements would mean that the device footprint has to be small. The use of electrical excitation also means that the choice of materials making up the plasmon polariton source must also be electrically conductive. One way to overcome these above mentioned challenges is to make use of simple structures made up of electrically conductive materials that exhibit plasmonic

properties. It would also be ideal if the material adopted for use exhibits compatibility with current complementary metal-oxide-semiconductor (CMOS) manufacturing processes. To further lower the device footprint, it may be possible to consider modifications to integrate existing components that can already meet the scaling requirements.

2.2. Plasmons and plasmon polaritons

A plasma is a medium with an equal concentration of positive and negative charges [2.3]. At least one of its charge types is mobile. In this case, the negative charges are the conduction electrons while the positive charges are ion cores in the background. Such a description of a plasma can be adequately represented by good conductors with dominant conduction electrons such as metals [2.4]. Plasmons are collective oscillations of free electrons in metals at a particular eigenfrequency, ω_p. In general, they are a quantum (collective unit) of charge density oscillation in a plasma. For a given quanta, plasmons have energy $\hbar\omega_p$. Plasmons are analogous to sound waves since they are longitudinal oscillations of the free electron gas which creates regions of varying electron density. When plasmons are formed as a result of excited resonances from incident excitation sources, they are known as plasmon polaritons.

Plasmon polaritons can be excited either via optical or electrical means as would be covered in Secs. 2.4 and 2.5. Both optical and electrical means of excitation involve electromagnetic radiation since optical sources are actually electromagnetic waves while electrical sources such as electron beams or tunnelling electrons produce their own electromagnetic waves as they move. The excited plasmon polaritons may be localised or propagating, depending on the structure or configuration in which they are excited. Since optical excitations and excited electron beams from electrical excitations form electromagnetic waves, macroscopic Maxwell's equations, the divergence relations and their corresponding boundary conditions have to be dealt with.

Maxwell's equations can exist in either differential or integral form and can be represented in terms of vector and scalar potentials [2.5]. Since the focus for this work is in the optical regime at high frequencies, ferromagnetic materials are not considered since it is assumed that the materials under consideration do not induce magnetic induction; hence the magnetisation vector, $\bar{M} = 0$. The differential form Maxwell's equations [2.5] can be represented as shown in Eqns. 2.1 and 2.2,

$$\nabla \times \bar{E} = -\frac{d\bar{B}}{dt} \tag{2.1}$$

$$\nabla \times \bar{H} = \bar{J} + \frac{d\bar{D}}{dt} \tag{2.2}$$

where $\bar{E}$ and $\bar{H}$ refer to the macroscopic electric and magnetic fields while $\bar{D}$ and $\bar{B}$ refer to the electric displacement field and the magnetic flux density respectively. $\bar{J}$ refers to the total electric current density. The divergence relations are represented in Eqns. 2.3 and 2.4 where ρ represents the total charge density.

$$\nabla \cdot \bar{D} = \rho \tag{2.3}$$

$$\nabla \cdot \bar{B} = 0 \tag{2.4}$$

The electric charge and current densities are related by the charge conservation law which states that

$$(\nabla \cdot \bar{J}) + \frac{d\rho}{dt} = 0 \tag{2.5}$$

In the absence of $\bar{M}$, the resultant constitutive relations can be derived as shown in Eqns. 2.6 and 2.7,

$$\bar{D} = \varepsilon_0 \bar{E} + \bar{P} = \varepsilon \bar{E} = \varepsilon_0 \varepsilon_r \bar{E} \tag{2.6}$$

$$\bar{B} = \mu_0 \bar{H} + \bar{M} = \mu \bar{H} = \mu_0 \mu_r \bar{H} = \mu_0 \bar{H} \qquad (2.7)$$

where ε_r and μ_r refer to the relative permittivity and relative permeability of the material, respectively. Assuming that the material is homogeneous and isotropic, it can be represented within the local response approximation at optical frequencies; the scalar complex relative permittivity can be used. The complex permittivity of metals can be derived using the Drude model where

$$\varepsilon_r(\omega) = 1 - \frac{{\omega_p}^2}{\omega^2 + {\gamma_g}^2} + \frac{i{\omega_p}^2 \gamma_g}{\omega^3 + \omega {\gamma_g}^2} \qquad (2.8)$$

For a lossless metal, the damping constant γ_g tends to 0, leading to zero imaginary part of the permittivity. As a result,

$$\varepsilon_r(\omega) = 1 - \frac{{\omega_p}^2}{\omega^2} \qquad (2.9)$$

The boundary conditions of Maxwell's equations are needed and solved when homogeneous structures are considered so as to ensure continuity at interfaces. These boundary conditions are obtained as shown in Eqns. 2.10 to 2.13,

$$\hat{n} \times (\overline{H_2} - \overline{H_1}) = J_s \qquad (2.10)$$

$$\hat{n} \times (\overline{E_2} - \overline{E_1}) = 0 \qquad (2.11)$$

$$\hat{n} \cdot (\overline{D_2} - \overline{D_2}) = \rho_s \qquad (2.12)$$

$$\hat{n} \cdot (\overline{B_2} - \overline{B_1}) = 0 \qquad (2.13)$$

where $\hat{n}$ is the unit vector pointing from medium 1 to medium 2.

There are two types of plasmon polaritons [2.6], volume plasmon polaritons and surface plasmon polaritons [2.7]. Volume plasmon polaritons are the longitudinal electron oscillations about positive ion cores within the bulk of an electron gas/plasma. In general, they can be defined as the

fluctuations of free charge density inside the material which propagate as a longitudinally polarised charge density wave. Volume plasmon resonances occur at the plasma frequency of metals, ω_p. The plasma frequency is primarily dependent on the electron density in accordance with the equation

$$\omega_p{}^2 = \frac{nq^2}{\varepsilon_0 m_e} \qquad (2.14)$$

where *n* refers to the density of conduction electrons, *q* is the charge of each electron, and m_e is the mass of the electrons. Volume plasmons are longitudinal modes which cannot be excited by incident electromagnetic waves, but only by particle impact which affects the electron density. The dispersion relation for bulk plasmon polaritons is as shown in Eqn. 2.15. k refers to the wavevector in the medium. The dispersion relation is plotted as shown in Fig. 2.1.

$$\omega^2 = \omega_p{}^2 + c^2k^2 \qquad (2.15)$$

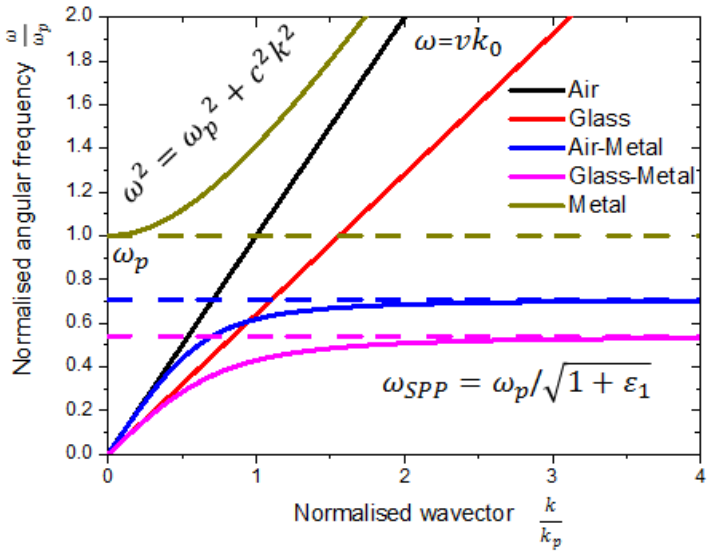

Figure 2.1: Dispersion relations for excitation of plasmon polaritons at insulator-metal interface

Surface plasmon polaritons (SPPs), on the other hand, are coherent electron oscillations that occur at the interface between two materials where the real part of the dielectric function changes its sign across the interface. In general, they can be defined as the fluctuations of free charge density inside the material which propagate along the interface of materials. Surface plasmon polariton waves are waves propagating at the planar interface between two half spaces. The charge motion in a surface plasmon polariton creates electromagnetic fields. Surface plasmon polaritons are the result of the coupled state between the excitation source and plasma oscillations at the interface between metal and dielectric. In response to an incident electric field, the electrons of the metal induce an opposing field determined by the dielectric function of the metal.

The surface plasmon energy is equal to the bulk plasmon energy divided by $\sqrt{2}$. This relation can be obtained from the surface plasmon dispersion relation at a single planar interface,

$$\beta = k_{SPP} = k_0\sqrt{\frac{\varepsilon_1\varepsilon_2}{(\varepsilon_2+\varepsilon_1)}} \qquad (2.16)$$

The dispersion relation is further discussed in Sec. 2.3. The surface plasmon frequency is the asymptote of the dispersion relation. From Eqn. 2.16,

$$\beta^2 = {k_0}^2\frac{\varepsilon_1\varepsilon_2}{(\varepsilon_2+\varepsilon_1)} \qquad (2.17)$$

where β diverges at the surface plasmon frequency when $\varepsilon_2 = -\varepsilon_1$. Since modes are required to be bound to the interface, one interface must be a dielectric while the other, a metal. Assuming medium 1 is a dielectric and

medium 2 is a metal, this means $\varepsilon_m = -\varepsilon_d$. When this happens, the complex permittivity of metals can be derived using the Drude model shown in Eqn. 2.8. For a lossless metal, γ_g tends to 0, leading to zero imaginery part of the permittivity. As a result,

$$\varepsilon_r(\omega) = \varepsilon_m = \varepsilon_2 = 1 - \frac{{\omega_p}^2}{\omega^2}. \quad (2.18)$$

Rearranging Eqn. 2.18,

$$\omega^2 = \frac{{\omega_p}^2}{1-\varepsilon_2} = \frac{{\omega_p}^2}{1+\varepsilon_d} \quad (2.19)$$

$$\omega = \frac{\omega_p}{\sqrt{1+\varepsilon_d}} \quad (2.20)$$

$$\omega_{SPP} = \frac{\omega_p}{\sqrt{1+\varepsilon_d}} \quad (2.21)$$

The largest value of ω_{SPP} occurs when ε_d is the smallest. This is only possible if the dielectric is air or vacuum where $\varepsilon_d = 1$. Hence,

$$\omega_{SPP} = \frac{\omega_p}{\sqrt{2}} \quad (2.22)$$

For some specimens and under certain conditions, surface plasmon polaritons can have a high intensity. These conditions include situations where the surface dominates over the volume of the specimen. The smaller the wavelength of the surface plasmon polariton, the shorter the length it travels or propagates over the surface. Surface waves can propagate along a metallic surface with a broad spectrum of eigenfrequencies from $\omega = 0 \; to \; \omega = \frac{\omega_p}{\sqrt{2}}$.

For SPPs, the fields on both sides of the insulator and metal interfaces are evanescent. Plasmon polaritons are being generated when the wavevector of the incident excitation source matches the wavevector of the plasmons. Eigenmodes of surface plasmon polaritons can be distinguished from volume

plasmon polaritons in that their effective mode index is greater than the mode index of the medium in which they are excited. Surface plasmon polaritons can be classified into localised and propagating surface plasmon polaritons.

Localised SPPs are charge oscillations that are confined to a nanostructure. They are the non-propagating part of SPPs which can be excited in nanostructures or nanoparticles. The free electron cloud of the nanostructure/nanoparticle can be resonantly excited by electromagnetic (EM) fields due to the enhanced polarizability of the particle/structure at certain frequencies. These enhanced polarizabilities give rise to strongly enhanced near fields close to the metal surface which are also known as hot spots.

Propagating SPPs are charge oscillations that propagate relatively large distances. They can be classified into short (up to tens of microns) and long (tens of microns in visible (VIS) to hundreds of microns in near infra-red (NIR)) range/travelling waves. Long range propagating SPPs show very low confinement and small damping while short range propagating SPPs show very high confinement but strong damping. Propagating SPPs are normally utilised in waveguiding configurations particularly long and short range waveguides. Examples of long range propagating SPP waveguides are insulator-metal-insulator (IMI) waveguides [2.8, 2.9] in which the metal layer is thinner than the skin depth, resulting in very low confined modes with very long propagation distances [2.10]. The skin depth of electromagnetic waves in metal refers to the penetration distance by which the electric field falls to 1/e [2.11]. One example is the Kretcshmann configuration. Examples of short range propagating SPP waveguides are metal-insulator-metal (MIM) waveguides [2.12, 2.13] in which the metal thickness is much thicker than the

skin depth, resulting in highly confined modes with short propagation distances.

The properties of propagating SPPs depend strongly on the waveguide design and are determined by the dispersion relations and thickness of the materials involved. Propagation behaviour of propagating SPPs are characterised by the effective mode index, n_{eff}, of the waveguide which defines the degree of confinement and the propagation wavevector of the SPP. As most dielectric materials show little or no damping, the propagation behaviour is mainly dominated by the properties of the metal layer.

2.3. Conditions for surface plasmon polaritons excitation

Surface plasmon polaritons are confined at the boundary between two interfaces and can be excited optically by matching the wavevector of the incident electromagnetic radiation with the wavevector of the plasmons in both interfaces in accordance with the dispersion relation for surface plasmons. To arrive at this dispersion relation, equations are derived for both transverse electric (TE) and transverse magnetic (TM) waves. Using the convention where a wave propagates in the x direction along metal dielectric interface, the plane of incidence is the xz plane and structure is infinitely long in the y direction. The wave equation for TM modes is given as

$$\frac{\partial^2 H_y}{\partial z^2} + (k_0{}^2 \varepsilon_r - \beta^2) H_y = 0 \qquad (2.23)$$

while the wave equation for TE modes is given as

$$\frac{\partial^2 E_y}{\partial z^2} + (k_0{}^2 \varepsilon_r - \beta^2)\, E_y = 0 \qquad (2.24)$$

and can be generalised using the Helmholtz equations given namely as

$$\nabla^2 \bar{E} + k^2 \bar{E} = 0 \qquad (2.25)$$

$$\nabla^2 \bar{H} + k^2 \bar{H} = 0. \qquad (2.26)$$

From the obtained wave equations, the dispersion relation for surface plasmon polaritons can be derived as

$$\beta = k_{SPP} = k_0 \sqrt{\frac{\varepsilon_1 \varepsilon_2}{(\varepsilon_2 + \varepsilon_1)}}. \qquad (2.27)$$

Rewriting,

$$\omega = c k_{SPP} \sqrt{\frac{\varepsilon_2 + \varepsilon_1}{\varepsilon_1 \varepsilon_2}}. \qquad (2.28)$$

$\omega(k)$ is known as the dispersion relation. For a linear dispersion relation, we say that the medium is non dispersive.

$$n_{eff} = \frac{\beta}{k_0} = \sqrt{\frac{\varepsilon_1 \varepsilon_2}{(\varepsilon_2 + \varepsilon_1)}} = n_{eff}' + i n_{eff}'', \quad (2.29)$$

where $n_{eff}$is the effective mode index.

$$\lambda_{eff}\ of\ SPP\ = \frac{\lambda_{SPP}}{n_{eff}'} \quad (2.30)$$

$$v_{eff} = \frac{c}{n_{eff}'} \quad (2.31)$$

$$L_{eff} = \frac{1}{n_{eff}''} \quad (2.32)$$

λ_{SPP} refers to the wavelength of excited SPPs, λ_{eff} refers to the effective wavelength, v_{eff} refers to the effective propagation speed and L_{eff} refers to the effective propagation length which is the number of wavelengths to attenuate to 1/e. This means that only TM polarised waves can excite propagating surface plasmon polaritons in IM structures. This is because for a TM polarised wave, there is an electric field perpendicular to the surface. As D_z is continuous, E_z changes, resulting in the accumulation of charge density at the interface. In a TE polarised wave, the electric field has no component perpendicular to the surface. Hence it is continuous and does not produce charge density accumulation at the surface.

While TM polarised waves can excite surface plasmons at IM interfaces, they can also excite surface plasmons in other geometries. Here, a multilayer metal-insulator-metal (MIM) structure with two interfaces is considered where the magnetic field is stronger at the interface and decays exponentially from the interface. The dispersion relation for surface plasmon

polaritons in an asymmetric MIM structure composed of different metals in medium 1 and 3 and an insulator in medium 2 can be calculated [2.14] and is given as

$$tanh(\gamma_2 a) = -\frac{R_2(R_1+R_3)}{{R_2}^2+R_1R_3} \tag{2.33}$$

where

$$\gamma = ik_z \tag{2.34}$$

and

$$R_j = \frac{\gamma_j}{\varepsilon_j}\ (j = 1,2\ or\ 3). \tag{2.35}$$

In the case of a symmetric MIM structure composed of similar metals, the dispersion relation for the symmetric multilayer (3 layer) structure is as follows:

$$\frac{R_1}{R_2} = \begin{cases} -coth\left(\gamma_2 \frac{a}{2}\right)\ if\ \overline{H_2}^+ = -\overline{H_2}^- \\ -tanh\left(\gamma_2 \frac{a}{2}\right) if\ \overline{H_2}^+ = \overline{H_2}^- \end{cases} \tag{2.36}$$

This constitutes two branches (symmetric and asymmetric) in symmetric structures. Similarly, only TM polarised waves can excite propagating surface plasmon polaritons in the MIM geometry.

For multilayer interfaces with more than three interfaces, it may be more convenient to analyse modes and solve for the dispersion relation using the impedance transformation technique [2.10] or the transfer matrix method (TMM) [2.15]. These mode analysis techniques can also be applied to multilayer dielectric interfaces.

To perform the calculations for real materials, the materials' permittivities are usually obtained via experiments and can be extrapolated accordingly as shown in Appendix A.

The wavelength range of electromagnetic radiation that can be used to excite surface plasmon polaritons is also limited since the lower the wavelength, the higher the frequency of the incident radiation and the harder and less responsive the electrons are to the incident radiation. At higher frequencies, the metal becomes transparent and behaves as a dielectric.

The surface plasmon resonance can only be observed if the width of the surface plasmon resonance profile is sufficiently narrow. The probability to observe a surface plasmon resonance increases with a decrease in frequency. Using the observable surface plasmon resonance width [2.16] as a benchmark, surface plasmon polaritons can only be observed below high frequencies of around 700 THz and above equivalent wavelengths of 400 nm. At lower frequencies and in the visible wavelength, only a few metals such as silver (Ag), gold (Au), aluminium (Al) and copper (Cu) are able to support a sharp plasmon resonance. At even lower frequencies or in the near infra-red wavelengths around 1200 nm, more metals such as nickel (Ni) and platinum (Pt) are able to support a sharp plasmon resonance.

The dispersion relation shown in Eqn. 2.28 holds only for a specific value of the permittivity of the metal medium $\varepsilon_2(\omega)$ at a specific frequency. An alternative expression [2.17] that is a continuous function of ω can be obtained by substituting Eqn. 2.9 in Eqn. 2.28 and expressing it as

$$y = \frac{1}{2} + x^2\left(\frac{1+\varepsilon_1}{2\varepsilon_1}\right) - \sqrt{\frac{1}{4} + x^2\left(\frac{2\varepsilon_1-2}{4\varepsilon_1}\right) + x^4\left(\frac{(\varepsilon_1+1)^2}{4{\varepsilon_1}^2}\right)} \qquad (2.37)$$

where $y = \frac{\omega^2}{\omega_p{}^2}$, $x = \frac{k_{SPP}}{k_p}$ and $k_p = \frac{\omega_p}{c}$. y and x are the normalised angular frequency and the normalised wavevector, respectively. From this expression, the dispersion relation of excited volume plasmon polaritons in metal, surface plasmon polaritons at an air/metal and a glass/metal interface are plotted as shown in Fig. 2.1, together with the light line in free space (air) and in glass. The refractive index of air is taken to be 1 while that of glass is taken to be 1.56. It can be seen that the dispersion relation of excited surface plasmon polaritons at the air/metal interface lies to the right of the light line in free space. These two lines do not intersect except at the origin. A similar phenomenon is seen for light incident at a glass/metal surface. The surface plasmon polaritons have a greater wavevector and momenta than that of light at any given frequency. This means that the surface plasmon polaritons are non-radiative and cannot be excited directly by an incident photon. Only when the dispersion relation coincides with the light line can the SPP mode be excited. This means that the momentum and energy are conserved. Light incident from the insulator at an IM interface cannot excite SPPs as the wavenumber of SPPs is higher than wavenumber of light in the insulator. For waves incident in air at an angle with respect to the surface normal, the in plane component, x along the interface is given by

$$k_x = k_{inc} sin\theta_{inc}. \qquad (2.38)$$

If the wave is incident in glass which is a medium with a higher dielectric constant leading to a higher refractive index, n_{medium} than air,

$$k_x = k_0 n_{medium}\, sin\theta_{inc} = k_0 \sqrt{\varepsilon_{medium}} sin\theta_{inc}. \qquad (2.39)$$

In this way, SPPs can be excited with wave vectors in between the free space light line and the dispersion relation in the glass medium as shown in Fig. 2.1.

2.4. Optical excitation of surface plasmon polaritons

In order to match the wavevector of the incident electromagnetic radiation with the wavevector of the plasmon polaritons, there have been attempts to make use of techniques such as attenuated total reflection (ATR) [2.18], or regular or irregular corrugations on surfaces on which plasmons are excited. ATR makes use of prism coupling and includes both the Otto [2.19] and Kretschmann [2.20] configuration while regular corrugations may refer to uniform gratings [2.21, 2.22] or nanostructured surfaces [2.23] and irregular corrugations may refer to engineered localised defects [2.24, 2.25] on surfaces. Irregular surface corrugations can be intentional or unintentional due to undesired effects in sample fabrication such as surface roughness and particle contamination. Either localised or propagating SPPs or a mixture of both can be excited depending on the profile of the nanostructure or the size of the planar surface on which the plasmons are excited.

For ATR, coupling is not based on direct coupling to plasmons at the insulator-metal interface but is based on total internal reflection (TIR) at the insulator-prism interface which results in the tunnelling of the evanescent fields that can couple to the propagating SPP modes at the metal-insulator interface. Since the wavenumber is directly proportional to the refractive index, a high refractive index material is used to increase the wavenumber of light.

In the Otto configuration shown in Fig. 2.2, there is a small gap between metal layer and prism. The evanescent field of the TIR wave tunnels through the air gap in order to excite a SPP mode at the air/metal interface. If

this phenomenon is observed, there is a minimum in the reflected signal at the angle/wavelength at which SPP excitation occurs.

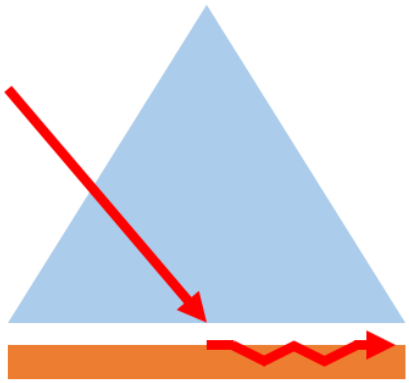

Figure 2.2: Otto configuration to excite plasmon polaritons

For the Krestchmann configuration shown in Fig. 2.3, evanescent waves from the thin metal layer are used to excite interface on the other side. A metal layer is deposited on top of a prism and a light beam is incident with an angle larger than the critical angle such that TIR occurs at the prism interface. Evanescent fields of TIR wave tunnel through the metal layer and excite propagating SPPs at the metal/air interface.

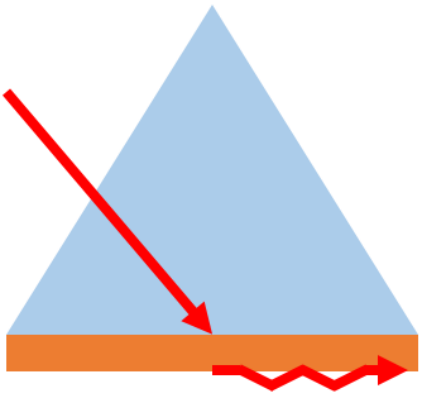

Figure 2.3: Kretschmann configuration to excite plasmon polaritons

With regular corrugations such as diffraction gratings shown in Fig. 2.4, gratings provide light with additional momentum on the grating axis due to spatial periodicity. For a 1D lattice, additional momentum (written as a change in wavevector) is given as

$$\Delta k = m\frac{2\pi}{a_{grating}}, \tag{2.40}$$

where $a_{grating}$ is the period of the grating and m is an integer.

$$g_{grating} = \frac{2\pi}{a_{grating}} \tag{2.41}$$

where g is the magnitude of the reciprocal vector of the grating. The matching between the incident wave and the excited SPP can be achieved when the condition is fulfilled.

$$k_{SPP} = k_{inc} sin\theta_{inc} + \Delta k \tag{2.42}$$

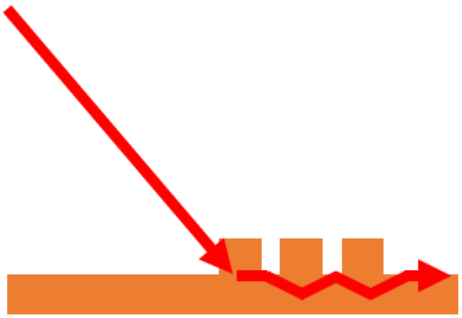

Figure 2.4: Regular corrugations in the form of diffraction gratings

Irregular corrugations can also serve to provide a similar enhancement in momentum.

Using regular corrugations provides advantages other than the excitation of plasmons. For instance, gratings on top of the metal surface, as in the case of V-shaped nanoantenna structure [2.21] connected at the ends at an

angle, allow the excited plasmons to be tuned to exhibit a directionality preference towards the side of the V-shaped nanoantenna structure. Also, regular corrugations in the form of nanostructured surfaces lead to enhanced transmission [2.26-2.29].

Plasmons can also be generated between gaps of nanoparticles [2.30-2.32], while taking into account the optical response of large coupled plasmonic systems including quantum effects as well as the permittivity of the gap medium. Laser excited plasmon sources have been demonstrated as well [2.33-2.36]. An example of a free electron laser excited plasmon source [2.37] is comprised of a nanohole in a periodically layered metal/dielectric structure where the potential is periodically modulated, leading to the excitation/scattering of surface plasmons on metal/dielectric interfaces within the structure. A singular surface plasmon beam can also be formed from the interference of two SPP waves [2.38]. Plasmon sources excited by TM polarised electromagnetic waves include that of a nanoslit structure together with a movable metal film [2.39].

While plasmons are usually generated on metal surfaces [2.40], they can also be generated on hybrid materials such as (Au/titanium dioxide (TiO_2)) [2.41] or on materials which have a negative permittivity and a high carrier mobility [2.42]. Graphene is also one such possibility since it has a high carrier mobility at high temperatures [2.42].

In an insulator-metal (IM) configuration where the metal layer is non-uniform and in the form of metallic nanostructures/particles, localised surface plasmon polaritons can be excited. For metallic nanostructures/particles with dimensions that are much smaller than the wavelength of the incident

electromagnetic wave, λ_{inc}, the quasistatic approximation can be adopted which approximates a uniform electric field over the volume of the particle. Dipolar plasmon resonances can thus be excited. For the case where the nanostructure or nanoparticle has dimensions that are comparable to the wavelength of the incident light, the quasistatic approximation is no longer valid.

Under the validity of the quasistatic approximation, two different polarisation states of the EM waves propagating along the two symmetry axes of the nanostructure/particle can be considered. For instance, it is only possible for a plane wave that propagates perpendicular to the plane of the nanodisc to excite a dipole resonance where the dipole moment is aligned with the polarisation vector of the incident wave. For the plane wave which propagates in the plane of the circular nanostructure with the polarisation in the plane of the nanostructure, a quadrupole mode is excited. This is as shown in Fig. 2.5.

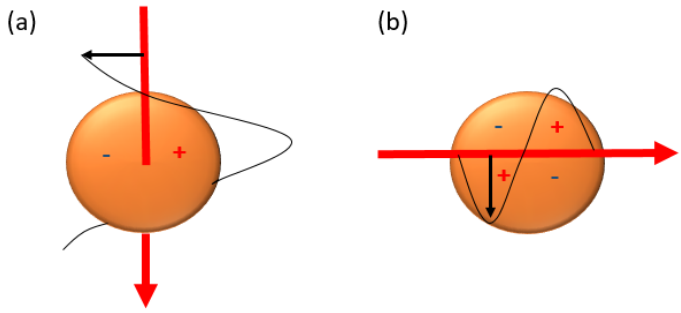

Figure 2.5: Exciting a (a) dipolar resonance mode. (b) quadrupolar resonance mode.

The wavelength of a localised surface plasmon resonance (LSPR) [2.43] depends on interactions between neighbouring particles. The interactions can be classified into both near and far field coupling. Near field

coupling results from particles separated by distances smaller than the wavelength of the incident light while far field coupling results from particles separated by distances larger than the wavelength of the incident light. The extent of the wavelength spectra shift depend on the phase coherence between the local modes excited in a particle and the scattered fields due to modes in the neighbouring particles.

In near field coupling, particles are considered as simple point dipoles. Coupling includes both longitudinal and transverse coupling. In transverse coupling as shown in Fig. 2.6(a), scattered fields of neighbouring particles enhance the local resonance and increase its energy while for longitudinal coupling as shown in Fig. 2.6(b), scattered fields of neighbouring particles oppose the local resonance and decrease its energy. Due to the decrease in energy, longitudinal coupling causes the plasmon resonance to red shift while transverse coupling causes the plasmon resonance to blue shift due to an increase in energy.

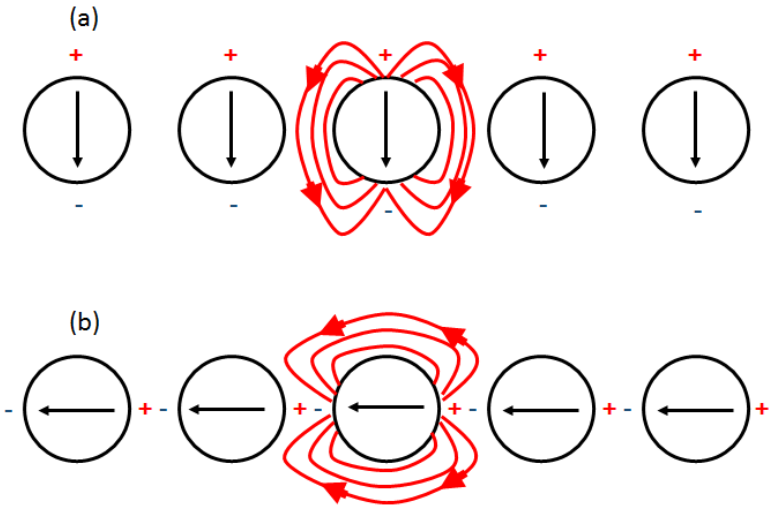

Figure 2.6: (a) Transverse coupling. (b) Longitudinal coupling.

For far field coupling, both transverse and longitudinal coupling will show an oscillating behaviour. Apart from being affected by interactions between neighbouring particles, LSPRs are highly tunable and allow light to be confined to deep subwavelength dimensions. Other design parameters to tune the LSPR include nanoparticle size and shape, material properties of the nanoparticle and the surrounding medium. For instance, an increase in the dimension of the particle causes the plasmon resonance to show a red shift due to a decrease in energy. This decrease in energy is due to the same energy being distributed over a larger volume of particle, thereby resulting in a decrease in energy per unit volume. LSPRs can be tuned from the ultraviolet (UV) part of the spectrum to the NIR by adopting different types of nanoparticle shapes such as spheres [2.44], rods [2.45, 2.46], triangles [2.47, 2.48] and cubes [2.49].

2.5. Electrical excitation of plasmon polaritons

Plasmon polaritons can be electrically excited by using either high energy electron beams generated from an electron gun in a transmission electron microscope (TEM) configuration or using low energy electron beams in the form of a tunnelling current. They can also be electrically excited using generated electron-hole pairs [2.50-2.55] via electrostatic interactions to form excitons [2.56].

In the TEM configuration, high energy electron beams are usually used in electron energy loss spectroscopy (EELS) which provides sub-nanometre spatial resolution. A sub-nanometre electron beam is focused on the structure of interest and the energy losses of the electrons to the structure are analysed. These energy losses are a result of the generation of excited plasmon polaritons when the electron beam is incident either normally [2.57, 2.58] or travelling parallel [2.59] to the structure of interest. The eigenfields from these excited plasmons can be calculated by making use of charge density and boundary conditions to solve for the SPP E and H fields travelling normally or parallel to the interface.

For normal incidence of the high energy electron beam, the electrons transfer momentum,

$$\bar{p} = \hbar\bar{k} \qquad (2.43)$$

and energy E_{loss} to the electrons of the metal as shown in Fig. 2.7 when they penetrate the metal. E_{loss} refers to the energy lost by electrons during the penetration and can be represented by the formula $E_{loss} = \hbar\omega$. Since the electrons are scattered at different angles, they deliver different momenta

$\hbar k_x = \hbar k_{scat}\, sin\theta_{scat}$ and hence wavevectors, $\bar{k}$. k_x refers to the wavevector along the x direction, k_{scat} refers to the wavevector along the direction of the scattered electrons and θ_{scat} refers to the angle of the direction of scattered electrons away to normal. If θ_{scat} is very small, $\hbar k_x = \hbar k_{scat}\, sin\theta_{scat} \approx \hbar k_{scat}\, \theta_{scat} \approx \hbar k_{inc}\, where\, k_{inc} = \frac{2\pi}{\lambda_{inc}}$. k_{inc} and λ_{inc} refers to the wavevector and wavelength of incident penetrating electrons respectively. At an increasing angle θ_{scat}, the dispersion relation can be measured for a very large k_x .

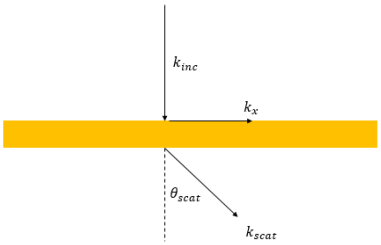

Figure 2.7: Schematic of high energy electron beam excitation of plasmons.

EELS studies have been applied to individual and multiple metal nanoparticles [2.60-2.62] such as rods and spheres [2.63], triangles [2.64] as well as nanostructures [2.65-2.67].

There has been much research on the creation of electrical plasmon sources using STM [2.68-2.71, 2.72]. The STM configuration is very similar to the TEM configuration. The only important difference that exists is just in the energy of the electron beam. Similar to TEM, STM allows control over the site of excitation but it is difficult to translate to practical applications due to bulky structures and high cost. Theoretically, the STM configuration can be likened to a 2-layer insulator metal (IM) structure due to the small size of the tip as compared to the overall surface on which plasmons are generated.

Assuming that the total input power goes into excitation of confined eigenwaves and non-confined leaky waves, the efficiency of SPP excitation using STM is extremely low due to high leakage radiation losses.

Low energy electron beams have also been used in metal-insulator-metal (MIM) structures to generate plasmon sources, making use of a roughened dielectric [2.12, 2.73 and 2.74] or induced change in molecular dipole moments from charge transfer in molecular tunnel junctions [2.75-2.81] to create tunnelling currents that excite plasmon polaritons. The use of these rough dielectric or uniform molecular junctions makes it difficult to control the location and types of excited plasmon polaritons, with heavy damping impeding the propagation lengths of excited plasmons. For electrically excited MIM structures, the insulator layer is usually very thin, leading to very short SPP propagation lengths [2.82]. It is also very difficult to couple these excited plasmons out [2.81].

2.6. Electrical excitation as an avenue for on-chip plasmon sources

Electronic circuits make use of electricity as a source to power up individual components. If optoelectronic integrated circuits are to be realised, they have to make use of a similar power source. Since the power source is to be utilised across many components in the circuit, each component would normally have low power requirements which must be respected. Low power requirements indirectly infer small device footprints. With electrical excitation, a tunnelling current could be generated with a small voltage bias for a small gap separation between a cathode and an anode [2.83]. The gap separation can range from nanometres to sub-nanometre. Optical excitation, on the other hand, requires sources much larger than the excitation wavelength. This means that since electromagnetic radiation in the visible to near infra-red wavelength range is needed to excite plasmon polaritons, in terms of applications in integrated circuits, only electrical excitation can offer scaling demands to meet low power requirements and can ultimately lead to small device footprints.

As such electrically excited plasmon polariton sources could provide an avenue to realise compact light sources [2.84, 2.85] and are essential to generate surface plasmon polaritons SPPs [2.86, 2.87].

While electrical excitation serves as the optimal means for excitation of plasmon polaritons, optical waveguiding techniques can also be adopted to couple out the excited plasmon polaritons. There are already many optical waveguide types that meet scaling requirements [2.12, 2.88-2.90]. These waveguides can be modified or redesigned to incorporate electrical excitation

so that they can serve both as a compact light source and as a waveguiding medium, reducing the need for an additional source component and maintaining a small device footprint. Such hybrid design concepts already exist (for other SPP applications) in the form of integrated laser diodes and waveguides [2.91, 2.92], integrated modulators and waveguides [2.93-2.95], and integrated waveguides and photodetectors [2.96, 2.97].

2.7. Summary

Comparing both optical and electrical means of plasmon excitation, electrical excitation is the most feasible to implement in an on-chip source since we can make use of electrical inputs on existing electronic circuits as a form of excitation to generate intermediary plasmons which can then be used as a form of communication in optoelectronic integrated circuits. The use of electrical excitation to generate a low energy electron beam in the form of a tunnelling current provides a similar excitation as that of high energy EELS, albeit having a large energy difference in the electron beam generated. In order for an electrically excited on-chip plasmon source to function efficiently, there are a few requirements to satisfy. First, the source needs to be able to generate long propagating surface plasmon polaritons with high efficiency. Second, it needs to be localised such that the location of excitation can be controlled. Third, the source needs to be small and compact since it has to be integrated on-chip. Lastly, the source needs to generate highly directional propagating surface plasmon polaritons. Once these design considerations can be fulfilled, an on-chip electrically excited plasmon source may indeed come to fruition.

2.8. References

[2.1] "1.8V+/- 0.15V (Normal range) and 1.2V to 1.95V (Wide range) power supply voltage and interface standard for non-terminated digital integrated circuit", EIA/JED-5003A (May 2005)

[2.2] K. Bernstein, K.M. Carrig, C.M. Durham, P.R. Hansen, D. Hogenmiller, E.J. Nowak and N.J. Rohrer, *High speed CMOS design styles* (Springer Science and Business media, 2012)

[2.3] P.A. Sturrock, *Plasma Physics: An introduction to the theory of Astrophysical, geophysical and laboratory plasmas* (Cambridge University Press, 1994)

[2.4] P. Drude, *The theory of optics* (Courier Corporation, 1925)

[2.5] J.D. Jackson, *Classical electrodynamics* (John Wiley and Sons, 1962)

[2.6] S.A. Maier, *Plasmonics: Fundamentals and Applications* (Springer, 2007)

[2.7] J.M. Pitarke, V.M. Silkin, E.V. Chulkov and P.M. Echenique, "Theory of surface plasmons and surface plasmon polaritons", Reports on Progress in Physics, 70, 1-87 (2006)

[2.8] E.P. Fitrakis, T. Kamalakis and T. Sphicopoulos, "Slow light in insulator-metal-insulator plasmonic waveguides", Journal of the Optical Society of America B, 28(9), 2159-2164 (2011)

[2.9] D.Y. Fedyanin, A.V. Arsenin, V.G. Leiman and A.D. Gladun, "Backward waves in planar insulator-metal-insulator waveguide structures", Journal of Optics, 12, 015002 (2010)

[2.10] J. Piper, "Theory and analysis of surface plasmon polaritons in metal films" (2011)

[2.11] A.K. Azad and W. Zhang, “Resonant terahertz transmission in subwavelength metallic hole arrays of sub-skin-depth thickness”, Optics Letters, 30(21), 2945-2947 (2005)

[2.12] P. Neutens, P.V. Dorpe, I.D. Vlaminck, L. Lagae and G. Borghs, “Electrical detection of confined gap plasmons in metal-insulator-metal waveguides”, Nature Photonics, 3, 283-286 (2009)

[2.13] E. Verhagen, J.A. Dionne, L. Kulpers, H.A. Atwater and A. Polman, “Near field visualisation of strongly confined surface plasmon polaritons in metal-insulator-metal waveguides”, Nano Letters, 8(9), 2925-2929 (2008)

[2.14] H.T.M.C.M. Baltar, K. Drozdowicz-Tomsia and E.M. Goldys, “Ch.6 Propagating surface plasmons and dispersion relations for nanoscale multilayer metallic dielectric films”, *Plasmonics Principles and applications* (2012)

[2.15] J. Chilwell and I. Hodgkinson, “Thin-films field transfer matrix theory of planar multilayer waveguides and reflection from prism loaded waveguides”, Journal of the Optical Society of America A, 1, 7 (1984)

[2.16] J.A. Scholl, A.L. Koh and J.A. Dionne, “Quantum plasmon resonances of individual metallic nanoparticles”, Nature, 483(7390), 421-427 (2012)

[2.17] R.A. Ferrell, “Predicted radiation of plasma oscillations in metal films”, Physical Review Letters, 111(50), 1214-1222 (1958)

[2.18] H. Raether, “Surface plasmons on smooth and rough surfaces and on gratings” (Springer, 1986)

[2.19] A. Otto, “Excitation of nonradiative surface plasma waves in silver by the method of frustrated total reflection”, Z.Phys, 216, 398 (1968)

[2.20] E. Kretschmann and H. Raether, “Radiative decay of nonradiative surface plasmons excited by light”, Z.Naturforsch, 23(12), 2135-2136 (1968)

[2.21] F. Huang, X. Jiang, H. Yang, S. Li and X. Sun, “Tunable directional coupling of surface plasmon polaritons with linearly polarised light”, Applied Physics B Lasers and Optics, 122(1), 1-6 (2016)

[2.22] R.H. Ritchie, E.T. Arakawa, J.J. Cowan and R.N. Hamm, “Surface plasmon resonance effect in grating diffraction”, Physical review letters, 21(22), 1530-1533 (1968)

[2.23] T.A. Kelf, Y. Sugawara, J.J. Baumberg, M. Abdelsalam and P.N. Bartlett, “Plasmonic bandgaps and trapped plasmons on nanostructured metal surface”, Physical review letters, 95(11), 116802 (2005)

[2.24] B. Hecht, H. Bielefeldt, L. Novotny, Y. Inouye and D.W. Pohl, “Local excitation, scattering, and interference of surface plasmons”, Physical review letter, 77(9), 1889-1892 (1996)

[2.25] H. Ditlbacher, J.R. Krenn, N. Felidj, B. Lamprecht, G. Schider, M. Salerno, A. Leitner and F.R. Aussenegg, “Fluorescence imaging of surface plasmon fields”, Applied physics letters, 80(3), 404-406 (2002)

[2.26] T.W. Ebesen, H.J. Lezec, H.F. Ghaemi, T. Thio and P.A. Wolff, “Extraordinary optical transmission through subwavelength hole arrays”, Nature, 391(6668), 667-669 (1998)

[2.27] H.F. Ghaemi, T. Thio, D.E. Grupp, T.W. Ebbesen and H.J. Lezec, “Surface plasmons enhance optical transmission through subwavelength holes”, Physical Rev. B, 58(11), 6779-6782 (1998)

[2.28] A. Krishnan, T. Thio, T.J. Kim, H.J. Lezec, T.W. Ebbesen, P.A. Wolff, J. Pendry, L. Martin-Moreno and F.J. Garcia-Vidal, “Evanescently coupled resonance in surface plasmon enhanced transmission”, Optics communications, 200(1), 1-7 (2001)

[2.29] A. Degiron, H.J. Lezec, W.L. Barnes and T.W. Ebbesen, “Effects of hole depth on enhanced light transmission through subwavelength hole arrays”, Applied physics letters, 81(23), 4327-4329 (2002)

[2.30] L. Wu, H. Duan, P. Bai, M. Bosman, J.K. Yang and E. Li, “Fowler Nordheim Tunnelling Induced charge transfer plasmons between nearly touching nanoparticles”, ACS Nano, 7(1), 707-716 (2012)

[2.31] R. Esteban, A.G. Borisov, P. Nordlander and J. Aizpurua, “Bridging quantum and classical plasmonics with a quantum corrected model”, Nature Communications, 3, 825 (2012)

[2.32] K.J. Savage, M.M. Hawkeye, R. Esteban, A.G. Borisov, J. Aizpurua and J.J. Baumberg, “Revealing the quantum regime in tunnelling plasmonics”, Nature Letter, 491(7425), 574-577 (2012)

[2.33] F. López-Tejeira, S.G. Rodrigo, L. Martín-Moreno, F.J. García-Vidal, E. Devaux, T.W. Ebbesen, J.R. Krenn, I.P. Radko, S.I. Bozhevolnyi, M.U. González and J.C. Weeber, “Efficient unidirectional nanoslit couplers for surface plasmons”, Nature Physics, 3(5), 324-328 (2007)

[2.34] J. Chen, Z. Li, S. Yue and Q. Gong, “Efficient unidirectional generation of surface plasmon polaritons with asymmetric single nanoslit”, Applied Physics Letters, 97(4), 041113 (2010)

[2.35] J. Chen, Z. Li, S. Yue and Q. Gong, “Highly efficient all optical control of surface plasmon polariton generation based on a compact asymmetric single slit, Nano letters, 11(7), 2933-2937 (2011)

[2.36] A. Baron, E. Devaux, J.C. Rodier, J.P. Hugonin, E. Rousseau, C. Genet, T.W. Ebbesen and P. Lalanne, “Compact antenna for efficient and unidirectional launching and decoupling of surface plasmons”, Nano letters, 11(10), 4207-4212 (2011)

[2.37] G. Adamo, K.F. MacDonald, Y.H. Fu, C.M. Wang, D.P. Tsai, F.G. de Abajo and N.I. Zheludev, “The light well: A tunable free electron light source on a chip”, 103(11), 113901 (2009)

[2.38] S. Wei, J. Lin, Q. Wang, G. Yuan, L. Du, R. Wang, L. Xu, M. Hong, C. Min and X. Yuan, “Singular diffraction free surface plasmon beams generated by overlapping phase shifted sources”, Optics Letters, 38(7), 1182-1184 (2013)

[2.39] Y. Wang, X. Zhang, H. Tang, K. Yang, Y. Wang, Y. Song, T.H. Wei and C.H. Wang, “A tunable unidirectional surface Plasmon polaritions source”, Optics Express, 17(22), 20457-20464 (2009)

[2.40] W.L. Barnes, A. Dereux and T.W. Ebbesen, “Surface plasmon subwavelength optics”, Nature, 24, 824-830 (2003)

[2.41] E. Kowalska, O.O. Mahaney, R. Abe and B. Ohtani, “Visible-light-induced photocatalysis through surface plasmon excitation of gold on

titania surfaces", Physical chemistry chemical physics, 12(10), 2344-2355, (2010)

[2.42] F. Liu, C. Qian and Y.D. Chong, "Directional excitation of graphene surface plasmons", Optics Express, 23(3), 2383-2391 (2015)

[2.43] K.A. Willets and R.P. van Duyne, "Localised surface plasmon resonance spectroscopy and sensing", Annu.Rev.Phys.Chem, 58, 267-297 (2007)

[2.44] T.R. Jensen, M.D. Malinsky, C.L. Haynes and R.P. van Duyne, "Nanosphere lithography: Tunable localised surface plasmon resonance spectra of silver nanoparticles", Journal of Physical Chemistry B, 104, 10549-10556 (2004)

[2.45] P. Zijlstra, P.M.R. Paulo and M. Orrit, "Optical detection of single non-absorbing molecules using the surface plasmon of a gold nanorod", Nature Nanotechnology, 7(6), 379-382 (2012)

[2.46] K.M. Mayer, S. Lee, H. Liao, B.C. Rostro, A. Fuentes, P.T. Scully, C.L. Nehl and J.H. Hafner, "A label free immunoassay based upon localised surface plasmon resonance of gold nanorods", ACS Nano, 2(4), 687-692 (2008)

[2.47] L.J. Sherry, R. Jin, C.A. Mirkin, G.C. Schatz and R.P. van Duyne, "Localised surface plasmon resonance spectroscopy of single silver triangular nanoprisms", Nano Letters, 6(9), 2060-2065 (2006)

[2.48] A.J. Haes and R.P. van Duyne, "A nanoscale optical biosensor: Sensitivity and selectivity of an approach based on the localised surface plasmon resonance spectroscopy of triangular silver

nanoparticles", Journal of the America Chemical Society, 124, 10596-10604 (2002)

[2.49] L.J. Sherry, S.H. Chang, G.C. Schatz and R.P. van Duyne, "Localised surface plasmon resonance spectroscopy of single silver cubes", Nano Letters, 5(10), 2034-2038 (2005)

[2.50] P. Neutens, L. Lagae, G. Borghs and P.V. Dorpe, "Electrical excitation of confined surface plasmon polaritons in metallic slot waveguides", Nano letters, 10, 1429-1432 (2010)

[2.51] D.M. Koller, A. Hohenau, H. Ditlbacher, N. Galler, F. Reil, F.R. Aussenegg, A. Leitner, E.J.W. List and J.R. Krenn, "Organic plasmon-emitting diode", Nature Photonics Letters, 2, 684 (2008)

[2.52] R.J. Walters, R.V.A. van Loon, I. Brunets, J. Schmitz and A. Polman, "A silicon based electrical source of surface plasmon polaritons", Nature Materials, 9, 21 (2009)

[2.53] L. Wang, T. Li, L. Li, W. Xia, X.G. Xu and S.N. Zhu, "Electrically generated unidirectional surface plasmon source", Optics Express, 20(8), 8710-8717 (2012)

[2.54] A. Babuty, A. Bousseksou, J.P. Tetienne, I.M. Doyen, C. Sirtori, G. Beaudoin, I. Sagnes, Y. De Wilde and R. Colombelli, "Semiconductor surface plasmon sources", Physical Review Letters, 104(22), 226806 (2010)

[2.55] J. Li, H. Shen, X. Dong, Y. Zhang, Z. Zhao, X. Duan and X. Meng, "Electrical excitation of surface plasmon polaritons using an Au ring grating/GaAs quantum well coupling structure", Plasmonics, 10(1), 145-149 (2015)

[2.56] X. Cui, C. Wang, A. Argondizzo, S. Garrett-Roe, B. Gumhalter and H. Petek, “Transient excitons at metal surfaces”, Nature Physics, 10(7), 505-509 (2014)

[2.57] P. Das, A. Kedia, P.S. Kumar, N. Large and T.K. Chini, “Local electron beam excitation and substrate effect on the plasmonic response of single gold nanostars”, Nanotechnology 24(40), 405704 (2013)

[2.58] W. Cai, R. Sainidou, J. Xu, A. Polman and F.J. Garcia de Abajo, “Efficient generation of propagating plasmons by electron beams”, Nano Letters, 9(3), 1176-1181 (2009)

[2.59] S. Liu, M. Hu, Y. Zhang, Y. Li and R. Zhong, “Electromagnetic diffraction radiation of a subwavelength hole array excited by an electron beam”, Physical Review E, 80, 036602 (2009)

[2.60] V.E. Babicheva, N. Kinsey, G.V. Naik, A.V. Lavrinenko, V.M. Shalaev and A. Boltasseva, “Ultra-compact modulators based on novel CMOS compatible plasmonic materials”, Optics Express, 21 (22), 27326-27337 (2013)

[2.61] J.R. Sambles, G.W. Bradbery and F. Yang, “Optical excitation of surface plasmons: An introduction”, Contemporary Physics, 32 (3), 173-183 (1991)

[2.62] C. Jung, S. Yee and K. Kuhn, “Integrated optics waveguide modulator based on surface plasmon resonance”, Journal of Lightwave Technology, 12(10), 1802-1806 (1994)

[2.63] M.W. Chu, V. Myroshnychenko, C.H. Chen, J.P. Deng, C.Y. Mou and F.J. García de Abajo, “Probing bright and dark surface plasmon modes

in individual and coupled noble metal nanoparticles using an electron beam", Nano Letters, 9(1), 399-404 (2008)

[2.64] A.L. Koh, A.L. Fernández-Domínguez, D.W. McComb, S.A. Maier and J.K. Yang, "High resolution mapping of electron beam excited plasmon modes in lithographically defined gold nanostructures", Nano Letters, 11(3), 1323-1330 (2011)

[2.65] C. Lin and A.S. Helmy, "Dynamically reconfigurable nanoscale modulators utilising coupled hybrid plasmonics", Scientific Reports, 5(12313), 1-10 (2015)

[2.66] C. Shen, T.K. Ng, J.T. Leonard, A. Pourhashem, H.M. Oubei, M.S. Alias, S. Nakamura, S.P. DenBaars, J.S. Speck, A.Y. Alyamani, M.M. Eldesouki and B.S. Ooi, "High modulation efficiency, integrated waveguide modulator laser diode at 448 nm", ACS Photonics, 3(2), 262-268 (2016)

[2.67] K. Liu, N. Li, D.K. Sadana and V.J. Sorger, "Integrated nanocavity plasmon light sources for on-chip optical interconnects", ACS Photonics, 3(2), 233-242 (2016)

[2.68] I.I. Smolyaniov, M.S. Khaikin and V.S. Edelman, "Light emission from the tunnelling junction of the scanning tunnelling microscope", Physics Letters A, 149(7), 410-412 (1990)

[2.69] J. Aizpurua, S.P. Apell and R. Berndt, "Role of tip shape in light emission from the scanning tunnelling microscope", Physical review B, 62(3), 2065 (2000)

[2.70] J. Chen, M. Badioli, P. Alonso-González, S. Thongrattanasiri, F. Huth, J. Osmond, M. Spasenović, A. Centeno, A. Pesquera, P. Godignon and

A.Z. Elorza, “Optical nano-imaging of gate tunable graphene plasmons”, Nature Letters, 487(7405), 77-81 (2012)

[2.71] Z. Fei, A.S. Rodin, G.O. Andreev, W. Bao, A.S. McLeod, M. Wagner, L.M. Zhang, Z. Zhao, M. Thiemens, G. Dominguez, M.M. Fogler, A.H. Castro Neto, C.N. Lau, F. Keilmann, and D.N. Basov, “Gate-tuning of graphene plasmons revealed by infrared nano-imaging,” Nature, 487(7405), 82–85 (2012).

[2.72] P. Bharadwaj, A. Bouhelier and L. Novotny, “Electrical excitation of surface plasmons”, Physical Review Letters, 106(22), 226802 (2011)

[2.73] J. Lambe and S.L. McCarthy, “Light emission from inelastic electron tunnelling”, Physical review letters, 37, 14 (1976)

[2.74] R.C. Jaklevic and J. Lambe, “Experimental study of quantum size effects in thin metal films by electron tunnelling”, Physical Review B, 12(10), 4146 (1975)

[2.75] M. Galperin and A. Nitzan, “Current induced light emission and light induced current in molecular tunnelling junctions”, Physical Review Letters, 95(20), 206802 (2005)

[2.76] E. Flaxer, O. Sneh and O. Cheshnovsky, “Molecular light emission induced by inelastic electron tunnelling”, Science, 262(5142), 2012-2013 (1993)

[2.77] R.C. Jaklevic and J. Lambe, “Molecular vibration spectra by electron tunnelling”, Physical Review Letters, 17(22), 1139 (1966)

[2.78] B.D. Fainberg, M. Jouravlev and A. Nitzan, “Light induced current in molecular tunnelling junctions excited with intense shaped pulses”, Physical review B, 76(24), 245329 (2007)

[2.79] D.J. Wold, R. Haag, M.A. Rampi and C.D. Frisbie, “Distance dependence of electron tunnelling through self-assembled monolayers measured by conducting probe atomic force microscopy: Unsaturated versus saturated molecular junctions”, Journal of Physical Chemistry B, 106(11), 2813-2816 (2012)

[2.80] J.M. Beebe, B. Kim, J.W. Gadzuk, C.D. Frisbie and J.G. Kushmerick, “Transition from direct tunnelling to field emission in metal-molecule-metal junctions”, Physical review letters, 97(2), 026801 (2006)

[2.81] W. Du, T. Wang, H.S. Chu, L. Wu, R. Liu, S. Sun, W.K. Phua, L. Wang, N. Tomczak and C.A. Nijhuis, “On-chip molecular electronic plasmon sources based on self-assembled monolayer tunnel junctions”, Nature Photonics, 10(4), 274-280 (2016)

[2.82] H.T. Baltar, E.M. Goldys and K. Drozdowicz-Tomsia, *Propagating surface plasmons and dispersion relations for nanoscale multilayer metallic dielectric films*, (INTECH Open Access Publisher, 2012)

[2.83] L.K. Ang, T.J.T. Kwan, and Y.Y. Lau, “New scaling of Child-Langmuir law in the quantum regime,” Physical Review Letters, 91(20), 208303 (2003)

[2.84] C.S. Kim, I. Vurgaftman, R.A. Flynn, M. Kim, J.R. Lindle, W.W. Bewley, K. Bussmann, J.R. Meyer and J.P. Long, “An integrated surface plasmon source”, Optics Express, 18(10), 10609-10615 (2010)

[2.85] T. Aihara, H. Sakai, A. Takeda, S. Okahisa, M. Fukuhara, M. Ota, Y. Ishii and M. Fukuda, “Coherent plasmonic interconnection in silicon based electrical circuit”, Journal of Lightwave Technology, 33(10), 2139-2145 (2015)

[2.86] A. Kubo, K. Onda, H. Petek, Z. Sun, Y.S. Jung and H.K. Kim, "Femtosecond imaging of surface plasmon dynamics in a nanostructured silver film", Nano letters, 5(6), 1123-1127 (2005)

[2.87] U. Hohenester and J. Krenn, "Surface plasmon resonances of single and coupled metallic nanoparticles: A boundary integral method approach", Physical review B, 72(19), 195429 (2005)

[2.88] M.P. Nielsen, L. Lafone, A. Rakovich, T.P.H. Sidiropoulos, M. Rahmani, S.A. Maier and R.F. Oulton, "Adiabatic nanofocusing in hybrid gap plasmon waveguides on the silicon-on-insulator platform", Nano Letters, 16(2), 1410-1414 (2016)

[2.89] I. Goykhman, B. Desiatov and U. Levy, "Experimental demonstration of locally oxidised hybrid silicon-plasmonic waveguide", Applied Physics Letters, 97(141106), 1-4 (2010)

[2.90] Z. Han, A.Y. Elezzabi and V. Van, "Experimental realisation of subwavelength plasmonic slot waveguides on a silicon platform" Optics Letters, 35(4), 502-504 (2010)

[2.91] O. Benson, "Assembly of hybrid photonic architectures from nanophotonic constituents," Nature, 480(7376), 193–199 (2011).

[2.92] R. Sachan, A. Malasi and G. Duscher, "Plasmon excitations in bimetallic Ag nanostructures by monochromated e beam", Microscopy and Microanalysis, 19(S2), 1510-1511 (2013)

[2.93] S. Raza, W. Yan, N. Stenger, M. Wubs and N.A. Mortensen, "Blueshift of the surface plasmon resonance in silver nanoparticles studied with EELS", Nanophotonics, 21(22), 27344-27355 (2013)

[2.94] M. N'Gom, S. Li, G. Schatz, R. Erni, A. Agarwal, N. Kotov and T.B. Norris, "Electron beam mapping of plasmon resonances in electromagnetically interacting gold nanorods", Physical Review B, 80(11), 113411 (2009)

[2.95] S.O. Guillaume, N. Geuquet and L. Henrard, "Numerical study of optical and EELS response of coupled metallic nanoparticles", *SPIE NanoScience+Engineering*, 80962E-80962E, International Society for Optics and Photonics (2011)

[2.96] D. Ly-Gagnon, S.E. Kocabas and D.A. Miller, "Integrated photodetectors in metal slot plasmonic waveguides", Frontiers in Optics 2008/Laser Science XXIV/Plasmonics and Metamaterials/Optical Fabrication and Testing, OSA Technical Digest (CD) (Optical Society of America), paper MWA1 (2008)

[2.97] J.T. Kim, Y.J. Yun, H. Choi and C.G. Choi, "Graphene based plasmonic photodetector for photonic integrated circuits", Optics Express, 22(1), 803-808 (2014)

Chapter 3. Electrically exciting long traveling propagating surface plasmon polaritons using pMIM structures.

3.1. Introduction

For electrical excitation of SPPs, electrodes which are good conductors are needed. In the simplest sense, in order to have electrical excitation, there is a need to have at least two electrodes in which one serves as an anode and the other serves as a cathode. An example of one such configuration is that of the MIM structure which sandwiches an insulator layer between two metal layers. The MIM structure allows electrical excitation since an electric field can be formed in the insulator layer.

Much research on MIM structures have thus far been focused on creating [3.1-3.4] plasmon polaritons using thin insulator layers or facilitating the waveguiding [3.5-3.7] of excited plasmon polaritons using thick insulator layers. A thin insulator allows for the possibility of electrical excitation since the thinner the insulator layer, the smaller the bias necessary to generate a tunnelling current. Thin insulator layers, however also lead to short SPP propagation lengths. Thicker insulator layers can improve the SPP propagation length but this will in turn reduces the strength of electrical excitation for a fixed applied voltage.

Since the requirements for exciting and transmitting excited plasmon polaritons for long propagating distances are at odds, there seems to be no way

to excite and transmit plasmon polaritons with the same MIM structure. Further, due to the uniform junction designs of typical MIM structures, it is difficult to control the location of excited plasmon polaritons. To control the location of excitation, non-uniform MIM structures in the form of STM excitation have been proposed which make use of localised tips. STM excitation enhances the SPPs' propagation lengths but is a bulky configuration which is difficult to translate to practical applications. Since the STM configuration shows potential in exciting and propagating plasmon polaritons for long distances, there may indeed be a possibility that plasmon generation and plasmon waveguiding can coexist with a non-uniform MIM structure. One potential solution is to find a way to integrate both tips and thick insulator layers based on the MIM configuration. A realisation of such a possibility would mean that one can make use of the optimal waveguiding designs [3.8-3.11] that are already available and tweak them to allow not just waveguiding but also excitation. This will reduce the need to design a plasmon source, and will further reduce the device footprint on the optoelectronic integrated circuit.

3.2. Proposed pMIM design

A compact and highly efficient tunable and localised source of propagating surface plasmon-polaritons is proposed based on a protruded metal-insulator-metal (pMIM) structure as shown in Fig. 3.1.

This structure is composed of (i) a protruded segment and (ii) an MIM waveguiding segment. The protruded segment of the pMIM makes use of the concept of tunnelling junctions to excite plasmon polaritons. These excited plasmon polaritons are then coupled into the thick insulator of the MIM waveguiding segment for long distance propagation. Different from the conventional MIM structure with thin uniform or roughened junctions for electrical excitations, the pMIM structure has a thick insulator layer in the waveguiding segment and a small gap between the protruded tip and the substrate to generate a tunnelling current with an applied external bias. The gap distance between top Au cathode and bottom Au anode ranges from sub-nanometre to nanometres, and is the shortest at the site of the protrusion and provides a passage for the tunnelling current for the excitation of propagating eigenmodes. Combining the advantages of an equivalent STM [3.12]-[3.14]] and MIM [3.15]-[3.22] excitation, the pMIM structure allows controllability over the location of the source and facilitates electrical excitation due to the presence of a short tunnelling path. It also allows more efficient plasmon-polariton generation as compared to a pure STM configuration due to minimized leakage. The presence of the protrusion also significantly enhances plasmon-polariton generation and allows smooth coupling onto the MIM waveguiding segment of the pMIM.

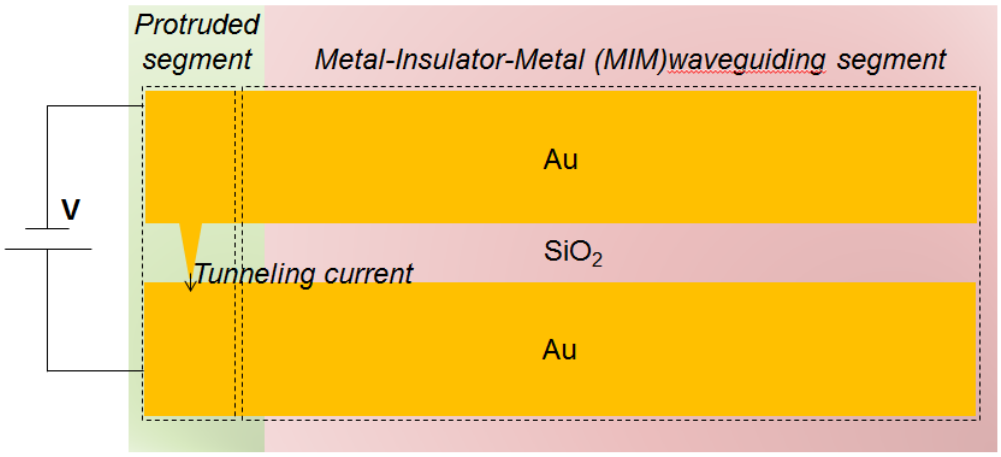

Figure 3.1: Protruded Au-SiO_2-Au configuration with a tunnelling path for propagating plasmon source generation along the MIM waveguiding segment. The dashed line distinguishes the protruded segment and MIM waveguiding segment [3.23].

In the case of the pMIM structure, the addition of a metal layer on top of the IM structure significantly lowers the excitation of leaky waves [3.24], thereby minimizing leakage radiation losses [3.25]. In an ideal situation, all the input power can be converted into confined waveguide modes with no leaky wave generation. Furthermore, the excitation of a single long travelling eigenmode would mean that all input power would go into the excitation of that mode with optimal efficiency. A qualitative comparison between excitation with IM and pMIM structures is shown in Fig. 3.2.

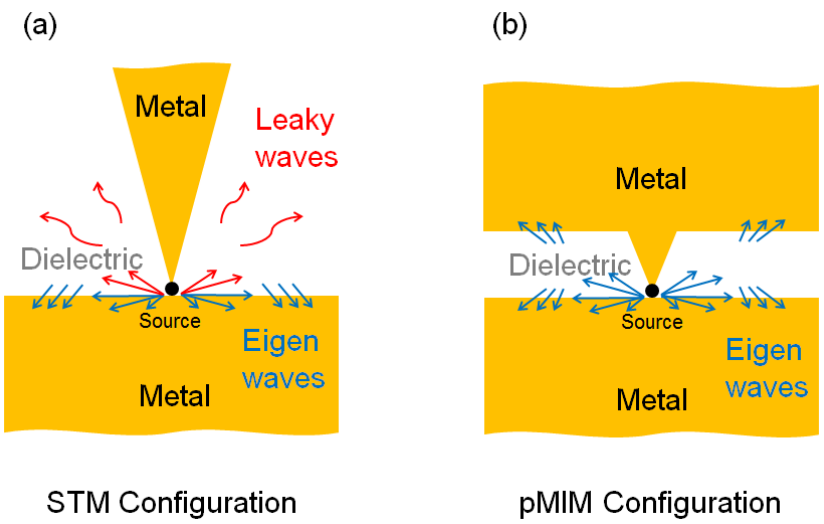

Figure 3.2: Efficiency of eigenmode excitation in semi-infinite (a) STM configuration and (b) pMIM configuration. Arrows indicate direction of power flow. Leaky waves are almost negligible in pMIM structures [3.23].

3.3. Tunnelling current excited plasmon polaritons

To model the tunnelling current, a spatially uniform tunnelling current density $\bar{J}(\omega)$ is used as the excitation. An increase in applied voltage bias causes an increase in tunnelling current density $\bar{J}(\omega)$ for a constant tunnelling path of 1 nm. $\bar{J}(\omega)$ is dependent on the static tunnelling current density, J_0 and voltage bias V in accordance to the relation

$$\bar{J}(\omega) = J_0 \left(1 - \frac{\hbar\omega}{eV}\right) \qquad (3.1)$$

Due to the nature of the tunnelling current being formed via a short tunnelling pass of 1 nm, J_0 is calculated self-consistently from a solution of the 1D time independent Poisson and Schrodinger's equations with the consideration of image potential, exchange correlation effects and space charge limited effects [3.26]. The calculated J_0 has the profile shown in Fig. 3.3.

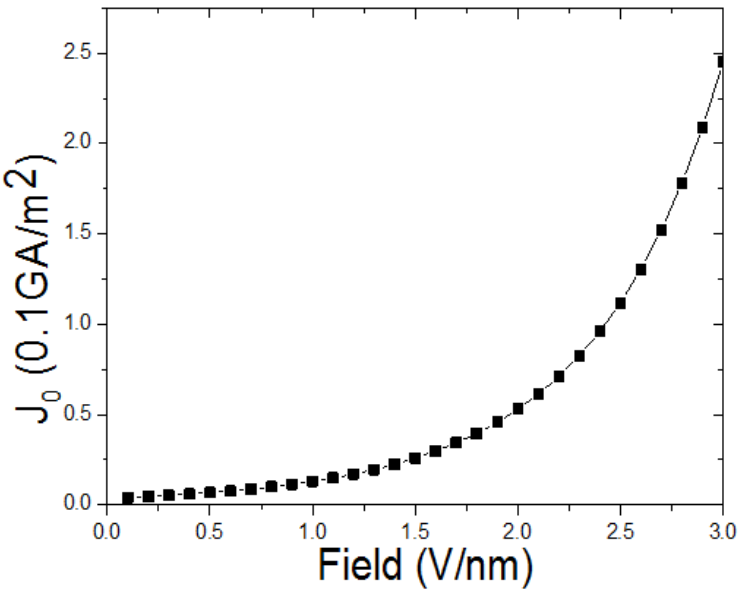

Figure 3.3: Calculated static current density profile as a function of applied bias [3.23].

In this study, the 1D approximation is sufficient even though the 3D tips of different profiles are considered. This is because only a realistic case over the region where the current is excited is considered. This is the flat part of the tip. It is difficult to fabricate tips which possess similar sharpness along both dimensions. A 1D case would suffice for a proof of concept and would serve as a realistic benchmark for practical tips. For this thesis, the focus is on the proof of concept and the use of such design principles.

The average power emitted by the tunnelling current, P(ω), can be measured at the site of the tunnelling current as shown in Fig. 3.4 and is computed as

$$P(\omega) = \frac{1}{2}\int \bar{E}(\omega) \cdot \bar{J}^{*}(\omega)\, dVol, \qquad (3.2)$$

where $\bar{E}(\omega)$ is the electric field, Vol is the volume of the tunnel current and dVol is the differential volume element of the tunnel current. To obtain the power P(ω), the calculated J_0 is substituted into Eqns. 3.1 and inserted as an external current density in the Maxwell's equation.

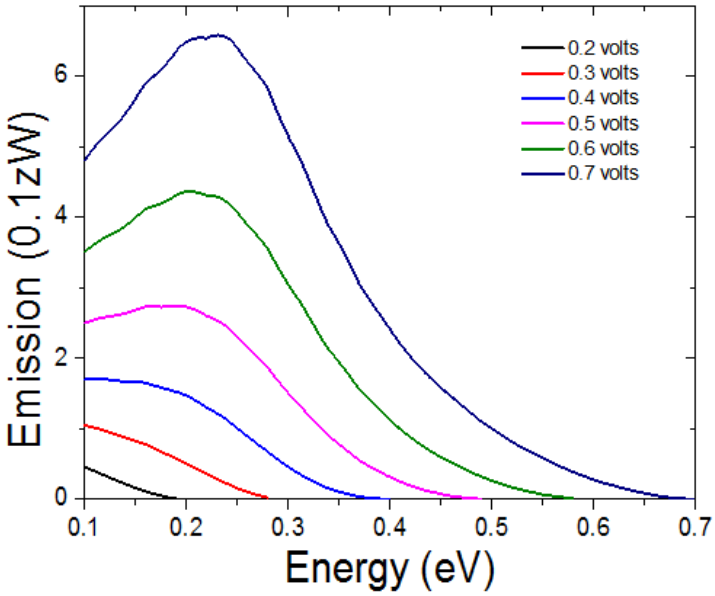

Figure 3.4: Power transferred from tunnelling current in pMIM into the excitation of SPPs as a function of energy for different applied biases in the single mode regime as would be discussed in section 4.2 [3.23].

An increase in applied voltage bias enhances the amount of power at the site of the tunnelling current that goes into exciting the SPPs in pMIM as shown in Fig. 3.4. By increasing the applied voltage bias, the emission peak can also be shifted to higher energies. This allows mode 1 in the single mode regime to be excited more strongly at higher energies. For example, increasing the voltage bias from 0.5 to 0.7 volts shifts the peak emission from 0.2 eV to 0.25 eV. More details on mode 1 in the single mode regime will be discussed in section 4.2.

There are two main mechanisms which allows the tunnelling current to excite plasmon polaritons. These are elastic and inelastic tunnelling mechanisms as shown in Fig. 3.5 [3.27]-[3.29]. The elastic tunnelling mechanism is the dominant process. The electrons tunnel elastically across the tunnelling region and contribute to the tunnelling current. These elastic tunnelling electrons excite cavity plasmon polaritons and modify the dielectric

environment. This in turn determines the cavity plasmon resonance energy, $\hbar\omega_0$. For the inelastic tunnelling mechanism, the tunnelling electrons lose energy from 0 to the applied bias of eV_0. Upon losing energy in the form of light emission, the inelastic tunnelling electrons couple to the cavity plasmon state.

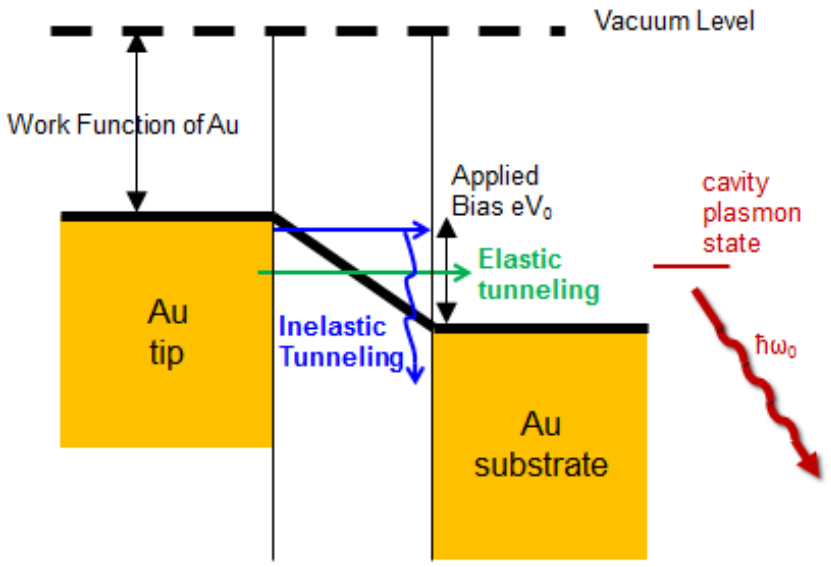

Figure 3.5: Elastic and inelastic tunnelling mechanisms' role in excitation of plasmon polaritons

3.4. Enhancement of emitted power from tunnelling current

To show that the proposed pMIM structure can electrically excite the intrinsic eigenmodes of the MIM waveguiding segment efficiently, an MIM waveguiding segment consisting of a gold (Au) cathode, 500 nm thick silicon dioxide (SiO_2) insulator and a Au anode is chosen. From theoretical calculations, this configuration is the most efficient amongst other practical material options that would include Eutectic Gallium Indium (EGaIn), Silver (Ag) and Aluminium (Al) for metals, as well as Air, Silicon Nitride (Si_3N_4) and Aluminium Oxide (Al_2O_3) for insulators. The criterion for the choice of material is to achieve the longest possible propagation lengths of excited plasmon-polaritons in the energy range (0.5-2.0 eV) of interest.

The presence of tip enhances emitted power by tunnelling current source. To generate a strong emitted power by the tunnelling current source, a long, narrow and sharp tip is ideal 0 since it has the smallest cross sectional area at the site of tunnelling current generation and the steepest slope gradient but is not feasible in reality due to limitations in fabrication. Rectangular, convex, triangular and concave tips shown in Fig. 3.6 were investigated to represent the range of possible practical tip profiles with different cross sectional areas and slope gradients.

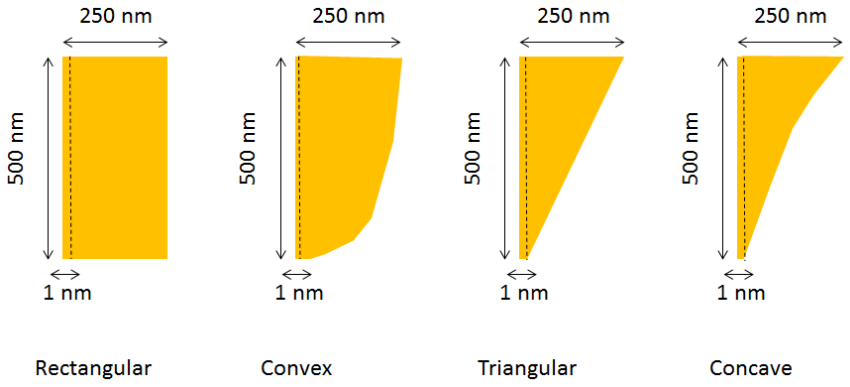

Figure 3.6: Practical rectangular, convex, triangular and concave tip profiles. Tip profile indicates only half of the cross-sectional view of the tip.

In the case of the circular convex and concave tip profile, a quadratic equation is used as a shape contour representation whereby shape contour, y is represented by Eqn. 3.3 while variables a and b are solved at the intersection points where the contour meets the tip edges. x refers to the distance along the shape contour.

$$y = ax^2 + bx \tag{3.3}$$

The pMIM structure with the configuration shown in Fig. 3.1 is studied using finite element method (FEM) simulation. First, it is found that the pMIM structure is able to enhance the power transferred by tunnelling current to excite eigenwaves as compared to MIM structures. Second, the fact that the pMIM simulation agrees well with eigenmode analysis of the MIM waveguiding segment as will be discussed further in chapter 4 provides clear evidence of good coupling from the protruded segment to the MIM waveguiding segment of the pMIM.

In the pMIM simulation, ideal uniform surfaces and interfaces over a domain size of 50 μm are assumed. Perfectly matched layer (PML) boundary conditions are used to absorb waves (both propagating and evanescent) with

near zero reflections. For the smallest wavelength studied, a mesh size of 10 elements per wavelength is used to ensure accuracy. The Au cathode, SiO_2 insulator and Au anode are assigned thicknesses of 1 μm, 500 nm and 1 μm, respectively. The protrusion has a base radius of 250 nm and a tip radius of 1 nm. It is placed 1 nm above the bottom Au anode. An external broadband inelastic tunnelling current between the protrusion and the bottom Au anode acts as the excitation source. While the tip allows a tunnelling current source to be generated, it also serves to enhance the emitted power from the tunnelling current.

To obtain the power transferred from the tunnelling current, the material permittivity is extrapolated to very low energies (0.1 eV) using the Drude model as shown in Appendix A and a surface integration is performed on the resistive loss for a 2D axial symmetric model of the pMIM structure. Thereafter, the surface integrated resistive loss is converted to a volume integrated resistive loss for a better depiction of a 3D pMIM structure.The emitted power spectra allow all possible peaks generated from excited plasmon polaritons to be detected. The emitted power is enhanced at different energies for different shaped tips for a fixed tunnelling current as shown in Fig. 3.7.

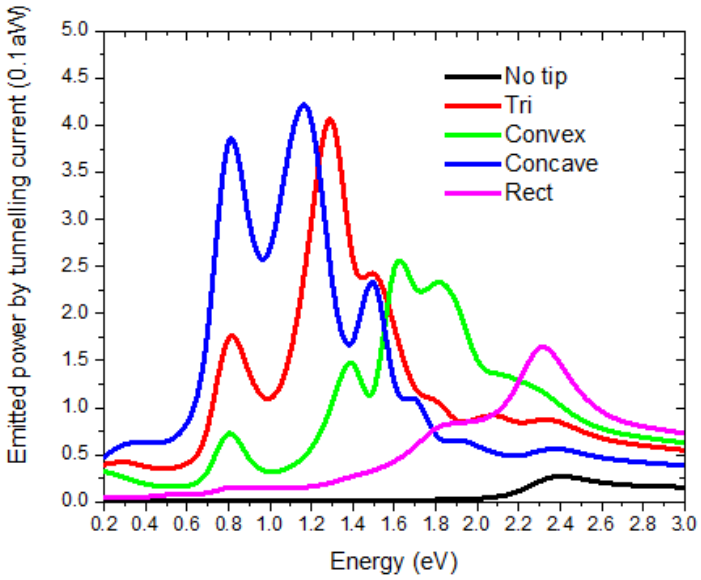

Figure 3.7: Emitted power (aW) vs Energy (eV) for different tip profiles if tunnelling current is kept constant at 0.2 eV across different energies

The tunnelling current at energy of 0.2 eV is used as a benchmark since the value of the tunnelling current varies at different energies due to the dispersive nature of the materials. This enhancement is due to the generation of plasmon polaritons in the form of eigenwaves at the insulator/metal interface. The emitted power is seen to be the strongest for the concave tip. The effect of applied bias on tunnelling current is taken into account in Fig. 3.8.

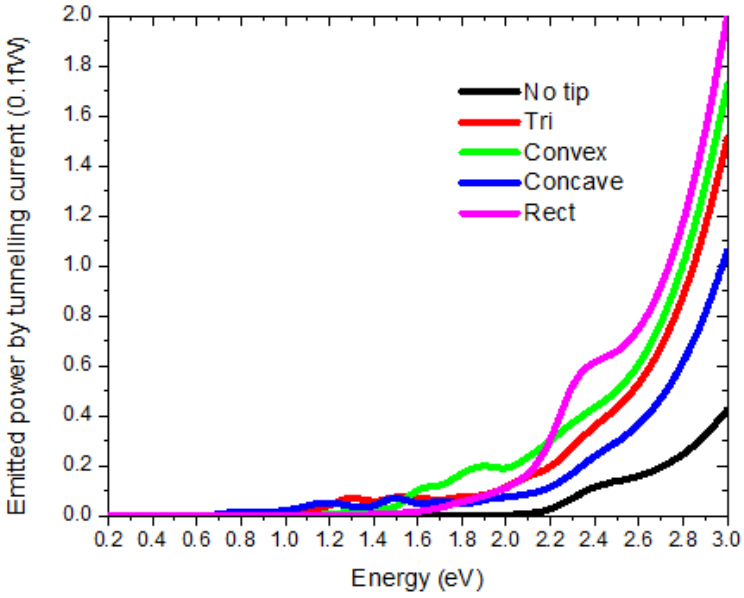

Figure 3.8: Emitted power (fW) vs Energy (eV) for different tip profiles for respective tunnelling current densities across different energies

The profile seen in Fig. 3.8 can be explained as follows. The tunnelling current density profile increases exponentially with applied bias for a 1nm gap as shown in Fig. 3.3. The power emitted by the tunnelling current is dependent on the tunnelling current density and hence increases exponentially with an applied bias as well. The applied bias has a direct correlation with the energy spectra from 0.2 eV to 3 eV since an applied bias is able to provide an excitation up till the energy at the applied bias. This accounts for the overall exponential profile of the emitted power by the tunnelling current across the energy spectra leading to the trend seen in Fig. 3.8.

A fixed value of the tunnelling current used in Fig. 3.7 is to highlight the change in resonant energy peaks due to generated plasmon polaritons which would otherwise be hidden if interpreted from Fig. 3.8 directly. Placing focus on the energy spectra for a fixed tunnelling current, it is possible to excite and tune resonant energy peaks with the different tip profiles.

Since the thickness of the insulator layer does not change and the top separation remains the same for the MIM waveguiding segment, it is postulated that the tip profile will not affect the propagation length of the excited plasmon polaritons. The tip profile will only affect the amount of power that goes into each excited eigenmode in the MIM waveguiding segment as would be discussed further in chapter 4. While not all the eigenwaves are excited by the same amount at a particular bias, eigenwaves at a specific resonant energy can be excited more strongly by adopting different tip profiles. Depending on the resonant energy of excited plasmon polaritons, the amount of enhancement can be determined. For instance, for a fixed tunnelling current to excite a single eigenwave at 0.6 eV or to excite 2 eigenwaves of equal strength at different resonant energies, a concave tip should be adopted. To explain the origin of the peaks shown in Fig. 3.7, the $|H_\phi|$ profile across the various interfaces is investigated as shown in Fig. 3.9. From the observed profile, peaks at 0.8 eV are seen to be due to the thickness of the insulator layer in the MIM waveguiding segment. Since all tip profiles have similar insulator thicknesses, the plasmon polaritons' resonant energy at the top Au/SiO_2 interface is the same.

Peaks at 1.2 eV, 1.3 eV and 1.4 eV are due to excited plasmon polaritons along SiO_2/bottom Au interface. These resonant energies are affected by the bottom tip profile. Since the bottom tip profile changes gradually from concave to triangular to convex, there is a shift in plasmon polariton resonant energies from 1.2 eV to 1.3 eV and 1.4 eV. The slope gradient of the tip is decreased abruptly from concave to a more gentle convex profile. A decrease in slope gradient is seen to result in a shift in SPP

resonance to higher energies due to a less localised collective resonance at the tip [3.13].

Peaks at 1.5 eV and 1.6 eV are due to plasmon polaritons excited at Au tip/SiO_2 interface. As the slope gradient is similar for both triangular and concave tips, they both show two peaks at 1.5 eV. A convex tip provides a gentler profile than triangular and concave tips and hence shows a resonant energy at 1.6 eV.

There's a peak around 2.1 eV which exist for all tips. This is due to the plasmon polaritons excited at the general SiO_2/bottom Au interface without the influence of the tip profile. Peak at 2.3 eV is due to plasmon polaritons excited at bottom Au tip/SiO_2 interface for the rectangular profile. It is able to support plasmon polaritons that have short propagation lengths within the MIM region between the rectangular tip and the bottom Au substrate.

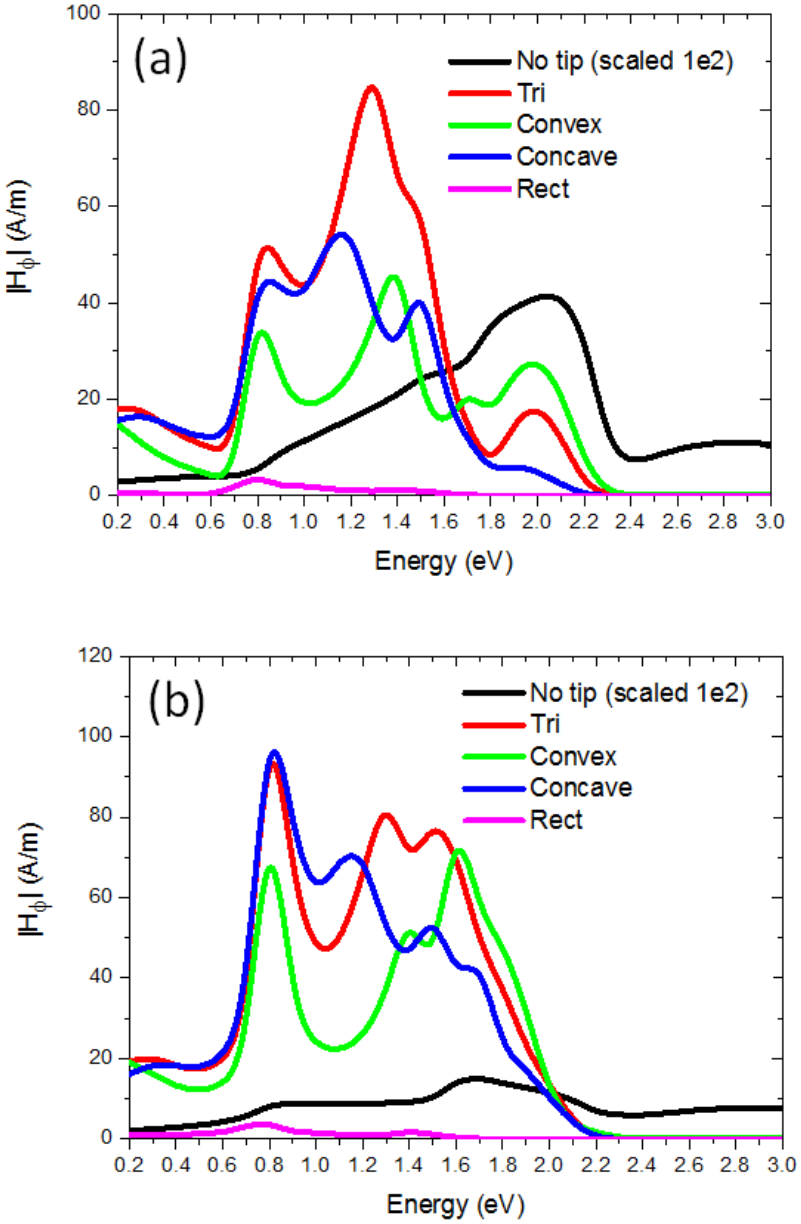

Figure 3.9: $|H_\phi|$ (A/m) vs Energy (eV) for different tip profiles at (a) SiO_2/bottom Au interface and (b) Top Au/SiO_2 interface.

To study the impact of the protruded tip on enhancement of the power emitted from the tunnelling current, the triangular protruded tip is used as a basis of comparison between MIM structures with an external excitation source. Figure 3.10 shows a comparison of the two cases. Compared to the MIM structures, the protrusion in pMIM structures allows for a huge enhancement in emission from the tunnelling junction.

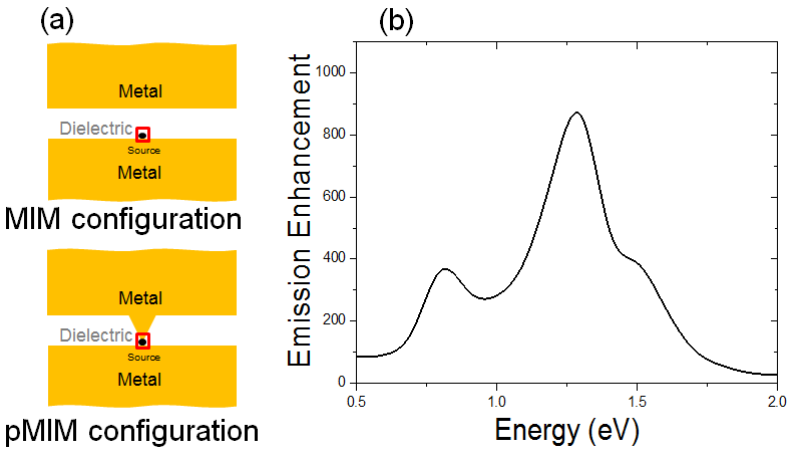

Figure 3.10: Emission enhancement in excitation of pMIM over MIM structures. (a) Site (red highlighted region) in vicinity of tunnel current where average power emitted by tunnelling current in MIM and pMIM structures is measured. (b) Emission enhancement (simulated) in pMIM is around two to three orders larger than MIM structures [3.23].

To show emission enhancement of the pMIM as compared to the MIM structures, the ratio of P(ω) for the pMIM is divided by P(ω) for the MIM. The enhancement in emission in the pMIM over the MIM structures is shown in Fig. 3.10(b). This emission enhancement in the pMIM compared to the MIM structures is around two to three orders and is particularly significant for the low energy range of 0.5 to 2.0 eV.

3.5. Tuning resonant peaks of emitted power from tunnelling current by investigating tip's gap

In order to tune the resonant peaks of power emitted from the tunnelling current, the gap separation of the tip can be varied. The gap under the tip allows resonant peaks to be tuned similar to the way tuning a cavity in a laser will change the operating wavelength. If the tunnelling current density is kept similar across different gap sizes, an increase in gap is seen to shift the emitted power to higher energies due to a less localised collective resonance as shown in Appendix B. To show the shift in more detail, a tunnelling current density at 0.2 eV for a 1 nm gap is used as the reference, as shown in Fig. 3.11. The peaks around 0.8 eV and 1.5 eV can be attributed to the thickness of the insulator layer and the Au tip/SiO2 interface. Although the gap distances change, the insulator thickness did not change while the Au tip/SiO2 interface remains the same as well. Hence there is no shift for the peaks around 0.8 eV and 1.5eV. Peaks from 1.1 to 1.3 eV are attributed to the SiO2/bottom Au interface. With a decreasing gap distance, there is shift to lower resonant energies since the resonant energies are affected by the tip profile. These affected resonant peaks are also reflected in the power that is coupled into the MIM waveguiding segment as shown in Fig. 3.12. Gap distance has a potential to be used as a tuning factor to adjust resonant wavelength peaks and control the amount of emitted power that is to be excited at the relevant wavelengths (energies) of interest. For the rest of the studies in the thesis, a gap separation of 1 nm is used.

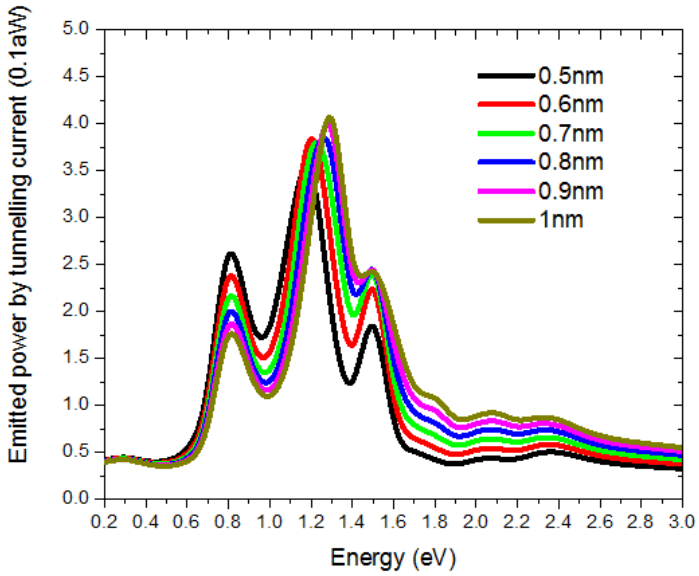

Figure 3.11: Power emitted by tunnelling current (aW) vs Energy (eV) for a pMIM triangular tip of different gap thicknesses if tunnelling current is kept constant at 0.2 eV for a 1 nm gap across different gap separations.

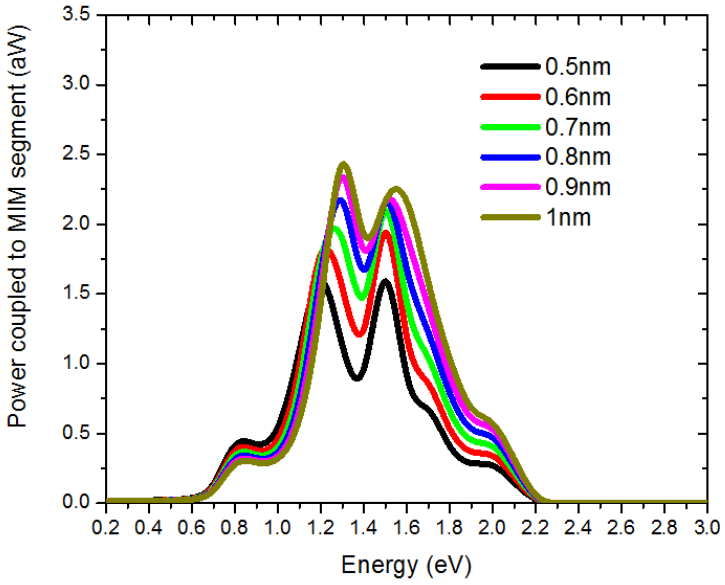

Figure 3.12: Power coupled into pMIM waveguiding segment (aW) vs Energy (eV) for a pMIM triangular tip of different gap thicknesses if tunnelling current is kept constant at a 1 nm gap across different gap separations.

3.6. Investigation of coupling efficiency of excited plasmon polaritons from the protruded segment to the MIM waveguiding segment

Apart from calculating the emitted power from the tunnelling current, there is a need to determine the efficiency of power transferred from the tunnelling current into the excitation of waveguide modes that can be coupled onto the waveguiding segment of the pMIM. The power that can be coupled into the waveguiding segment of the pMIM is calculated at the beginning of the MIM waveguiding segment and obtained for a constant tunnelling current at 0.2 eV for a 1 nm gap as shown in Fig. 3.13 and with the effects of applied bias on tunnelling current being taken into account in Fig. 3.14. Rectangular, convex, triangular and concave tip profiles were considered. When the applied bias is taken into account, the locations of the resonant peaks remain the same but the magnitude of the peaks is enhanced at higher energies.

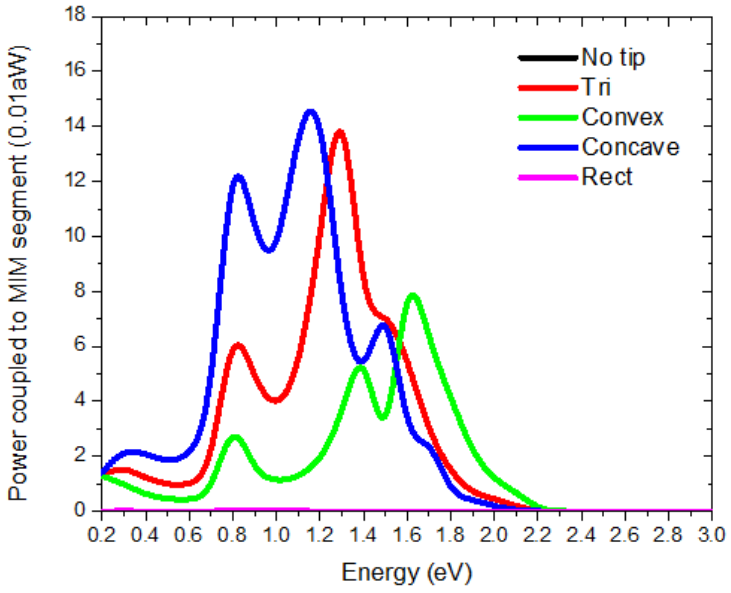

Figure 3.13: Power coupled into pMIM waveguiding segment (aW) vs Energy (eV) for different tip profiles if tunnelling current is kept constant at 0.2 eV across different energies.

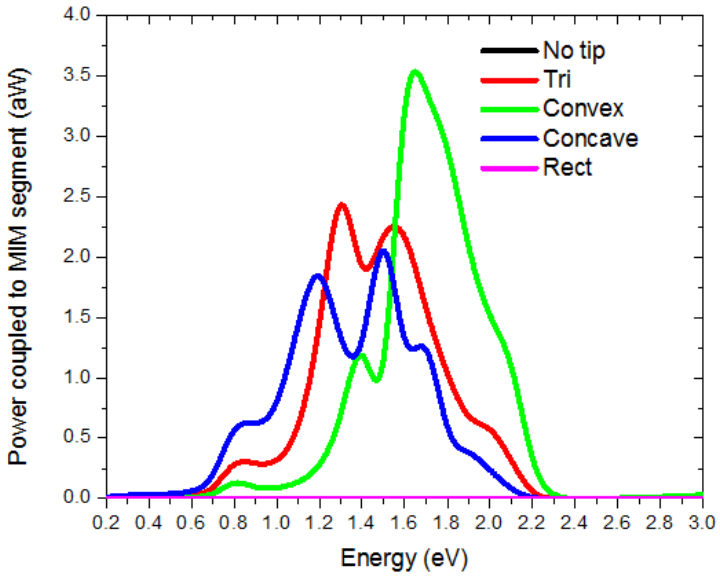

Figure 3.14: Power coupled into pMIM waveguiding segment (aW) vs Energy (eV) for different tip profiles with respective tunnelling current densities across different energies.

It can be seen that the amount of power coupled into the waveguiding segment is negligible for rectangular tip profiles and pure MIM structures as compared to triangular, concave and convex tip profiles. This could be due to the abrupt transition of the excited propagating SPPs from the tip's gap to the insulator layer in the MIM waveguiding segment. Much of the power could have been directed into localised SPPs instead. From this power, the coupling efficiency of excited eigenwaves can be calculated by comparing the emitted power from the tunnelling current and the power that is coupled into pMIM waveguiding segment as shown in Fig. 3.15.

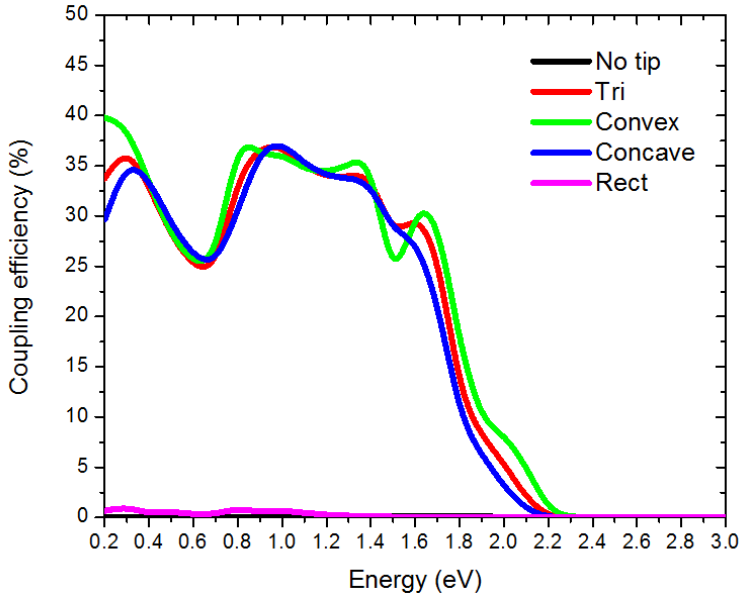

Figure 3.15: Coupling efficiency of power transferred from tunnelling current to excite eigenmodes in the waveguiding segment of pMIM structures.

The convex, triangular and concave tips show much higher coupling efficiency when compared with the rectangular tip. Among these three high-efficiency tips, the convex tip profile provides the best efficiency followed by the triangular and concave tip profile. Reasonable efficiencies of more than 10% are obtained over energies between 0.2 and 2 eV, with the highest coupling and excitation efficiency falling within the single and dual mode regimes which will be discussed in chapter 4.

3.7. Summary

In conclusion, a tunnelling current can be electrically induced in the proposed pMIM structure via a small applied voltage bias, locally exciting long traveling plasmon polaritons with high efficiency and no leakage radiation. The protruded tip enhances the total emitted power from the tunnelling current and the amount of power that can be coupled into the MIM waveguiding segment. The tip's profile affects the resonant peaks excited in both the gap and the MIM waveguiding segment. A concave tip with the smallest cross sectional area and the steepest slope gradient enhances emitted power most. An increasing gap separation at the protruded segment allows resonant peaks of power emitted from tunnelling current to be tuned which in turn shifts these resonant peaks of power to higher energies in the MIM waveguiding segment. When the excited plasmon polaritons are coupled to the MIM waveguiding segment, they can be decomposed into intrinsic eigenmodes. However not every eigenmode is desired. In the next chapter, excited eigenwaves are decomposed to identify and excite specific desirable eigenmodes in the MIM waveguiding segment.

3.8. References

[3.1] R.J. Walters, R.V.A. van Loon, I. Brunets, J. Schmitz and A. Polman, "A silicon based electrical source of surface plasmon polaritons", Nature Materials, 9(1), 21-25 (2010)

[3.2] P. Neutens, P.V. Dorpe, I.D. Vlaminck, L. Lagae and B.G. Borghs, "Electrical detection of confined gap plasmons in metal-insulator-metal waveguides", Nature Photonics, 3(5), 283-286 (2009)

[3.3] E. Verhagen, J.A. Dionne, L. Kuipers, H.A. Atwater and A. Polman, "Near field visualisation of strongly confined surface plasmon polaritons in metal-insulator-metal waveguides", Nano Letters, 8(9), 2925-2929 (2008)

[3.4] H.T. Miyazaki and Y. Kurokawa, "Squeezing visible light waves into a 3 nm thick and 55 nm long plasmon cavity", Physical Review Letters, 96, 097401 (2006)

[3.5] Y. Bian and Q. Gong, "Optical performance of one dimensional hybrid metal-insulator-metal structures at telecom wavelength", Optics Communications, 308, 30-35 (2013)

[3.6] R. Zia, M.D. Selker, P.B. Catrysse and M.L. Brongersma, "Geometries and materials for subwavelength surface plasmon modes", Journal of the Optical Society of America A, 21(12), 2442-2446 (2004)

[3.7] A.R. Davoyan, I.V. Shadrivov, S.I. Bozhevolnyi and Y.S. Kivshar, "Backward and forward modes guided by metal-dielectric-metal plasmonic waveguides", Journal of Nanophotonics, 4(1), 043509 (2010)

[3.8] P. Neutens, P.V. Dorpe, I.D. Vlaminck, L. Lagae and G. Borghs, “Electrical detection of confined gap plasmons in metal-insulator-metal waveguides”, Nature Photonics, 3(5), 283-286 (2009)

[3.9] M.P. Nielsen, L. Lafone, A. Rakovich, T.P.H. Sidiropoulos, M. Rahmani, S.A. Maier and R.F. Oulton, “Adiabatic nanofocusing in hybrid gap plasmon waveguides on the silicon-on-insulator platform”, Nano Letters, 16(2), 1410-1414 (2016)

[3.10] I. Goykhman, B. Desiatov and U. Levy, “Experimental demonstration of locally oxidised hybrid silicon-plasmonic waveguide”, Applied Physics Letters, 97(141106), 1-4 (2010)

[3.11] Z. Han, A.Y. Elezzabi and V. Van, “Experimental realisation of subwavelength plasmonic slot waveguides on a silicon platform” Optics Letters, 35(4), 502-504 (2010)

[3.12] I.I. Smolyaniov, M.S. Khaikin and V.S. Edelman, “Light emission from the tunnelling junction of the scanning tunnelling microscope”, Physics Letters A, 149(7), 410-412 (1990)

[3.13] J. Chen, M. Badioli, P. Alonso-González, S. Thongrattanasiri, F. Huth, J. Osmond, M. Spasenović, A. Centeno, A. Pesquera, P. Godignon and A.Z. Elorza, “Optical nano-imaging of gate tunable graphene plasmons”, Nature Letters, 487(7405), 77-81 (2012)

[3.14] Z. Fei, A.S. Rodin, G.O. Andreev, W. Bao, A.S. McLeod, M. Wagner, L.M. Zhang, Z. Zhao, M. Thiemens, G. Dominguez, M.M. Fogler, A.H. Castro Neto, C.N. Lau, F. Keilmann, and D.N. Basov, “Gate-tuning of graphene plasmons revealed by infrared nano-imaging,” Nature 487(7405), 82–85 (2012).

[3.15] P. Drude, *The theory of optics* (Courier Corporation, 1925)

[3.16] M.P. Nielsen, L. Lafone, A. Rakovich, T.P.H. Sidiropoulos, M. Rahmani, S.A. Maier and R.F. Oulton, “Adiabatic nanofocusing in hybrid gap plasmon waveguides on the silicon-on-insulator platform”, Nano Letters, 16(2), 1410-1414 (2016)

[3.17] I. Goykhman, B. Desiatov and U. Levy, “Experimental demonstration of locally oxidised hybrid silicon-plasmonic waveguide”, Applied Physics Letters, 97(141106), 1-4 (2010)

[3.18] Z. Han, A.Y. Elezzabi and V. Van, “Experimental realisation of subwavelength plasmonic slot waveguides on a silicon platform” Optics Letters, 35(4), 502-504 (2010)

[3.19] J.A. Dionne, K. Diest, L.A. Sweatlock and H.A. Atwater, “PlasMOStor: A metal-oxide-Si field effect plasmonic modulator”, Nano Letters, 9(2), 897-902 (2009)

[3.20] A. Melikyan, L. Alloatti, A. Muslija, D. Hillerkuss, P.C. Schindler, J. Li, R. Palmer, D. Korn, S. Muehlbrandt, D. Van Thourhout, B. Chen, R. Dinu, M. Sommer, C. Koos, M. Kohl, W. Freude and J. Leuthold, “High speed plasmonic phase modulators”, Nature Photonics, 8(3), 229-233 (2014)

[3.21] A. Melikyan, N. Lindenmann, S. Walheim, P.M. Leufke, S. Ulrich, J. Ye, P. Vincze, H. Hahn, T. Schimmel, C. Koos, W. Freude and J. Leuthold, “Surface plasmon polariton absorption modulator”, Optics Express, 19(9), 8855-8869 (2014)

[3.22] M.W. Ryu, J.S. Lee, K.S. Kim, K. Park, J.R. Yang, S.T. Han and K.R. Kim, “High performance plasmonic THz detector based on asymmetric

FET with vertically integrated antenna in CMOS technology", IEEE Transactions on electron devices, 63(4), 1742-1748 (2016)

[3.23] W.K. Phua, Y. Akimov, L. Wu, H.S. Chu, P. Bai and A. Danner, "Highly efficient tunable and localised on-chip electrical plasmon source using protruded metal-insulator-metal structure", Optics Express, 24(10), 10663-10674 (2016)

[3.24] L.W. Luo, N. Ophir, C.P. Chen, L.H. Gabrielli, C.B. Poitras, K. Bergmen, and M. Lipson, "WDM-compatible mode-division multiplexing on a silicon chip," Nature Communications, 5, 3069 (2014)

[3.25] D. Marcuse, *Theory of Dielectric Optical Waveguides* (Elsevier, 2013)

[3.26] L.K. Ang, T.J.T. Kwan, and Y.Y. Lau, "New scaling of Child-Langmuir law in the quantum regime," Physical Review Letters, 91(20), 208303 (2003)

[3.27] J. Lambe and S.L. McCarthy, "Light emission from inelastic electron tunnelling", Physical review letters, 37, 14 (1976)

[3.28] Y. Uehara, Y. Kimura, S. Ushioda and K. Takeuchi, "Theory of visible light emission from scanning tunneling microscope", Japanese Journal of Applied Physics, 31, 2465-2469 (1992)

[3.29] G. Schull, N. Neel, P. Johansson and R. Berndt, "Electon plasmon and electron electron interactions at a single atom contact", Physical Review Letters, 102(5), 057401 (2009)

[3.30] J. Azipurua, S.P. Apell and R. Berndt, "Role of tip shape in light emission from the scanning tunnelling microscope", Physical Review B, 62(3), 2065-2073 (2000)

Chapter 4. Excited eigenwaves in MIM waveguiding segment of pMIM

4.1. Introduction

By applying a voltage bias, the tunnelling current in the protruded tip of the pMIM will excite plasmon polaritons in the form of eigenwaves which can be coupled to the MIM waveguiding segment; these can be decomposed mathematically into intrinsic eigenmodes. The identification of individual eigenmodes is important in order to identify the type and properties of the excited plasmon polaritons. Excited plasmon polaritons may be made up of surface or volume plasmon polaritons with different effective mode indices as well as different propagation lengths.

Some eigenmodes could be excited more strongly than others, depending on the application. In the context of a plasmon source, one would require the excitation of surface eigenmodes with long propagation distances. The property of each excited eigenmode is intrinsic to the design parameters of the MIM waveguiding segment. With the proposed pMIM structure however, the properties of eigenmodes that can be excited in the MIM waveguiding segment remain the same but the presence of an electrical excitation allows control over the applied bias which makes it possible to ensure that the desired eigenmode is excited. To ensure the desired eigenmode can be excited with high efficiency, a decomposition of the eigenwaves that are coupled into the MIM waveguiding segment can be performed. A

decomposition technique has been proposed in this thesis to address this need, thereby allowing the efficiency of exciting desired eigenmodes to be gauged. Coupled with electrical control over the applied voltage bias in pMIM structures, desired eigenmodes with high efficiencies can be excited.

4.2. Intrinsic eigenmodes in MIM waveguiding segment

Based on earlier studies, the energy range of 0.5 to 2 eV is found to be optimal for excited eigenwaves in the MIM waveguiding segment while taking into account coupling efficiencies from the protruded tip. Using the pMIM structure with a triangular tip as a benchmark, an eigenmode analysis [4.1] is performed for the energy range of 0.5 to 2.0 eV to extract mode indices and propagation lengths of excited plasmon-polaritons that can be supported within the Au-SiO_2-Au MIM waveguiding segment. The excited eigenmodes comprise both volume and surface eigenmodes that can generally be distinguished with the effective mode index. The volume and surface eigenmodes feature propagating and evanescent fields in the insulator [4.2, 4.3] having effective mode indices below and above the insulator refractive index in the MIM waveguiding segment, respectively.

For the Au-SiO_2-Au MIM waveguiding segment, three different excited eigenmodes can be identified [4.1, 4.4]. Since each of these modes has different eigenmode indices and is excited at different energies, three operating regimes can be identified; each regime shows either an independent mode or the start of the rise of additional modes. The cut-off energies of the three regimes can be identified by comparing the real and imaginary components of the calculated mode indices. The modes are considered when they have a significant eigenmode index beyond the cutoff regime. The plots of mode index and propagation length as function of energy as well as the associated regimes are shown in Figs. 4.1(a) and 4.1(b) respectively.

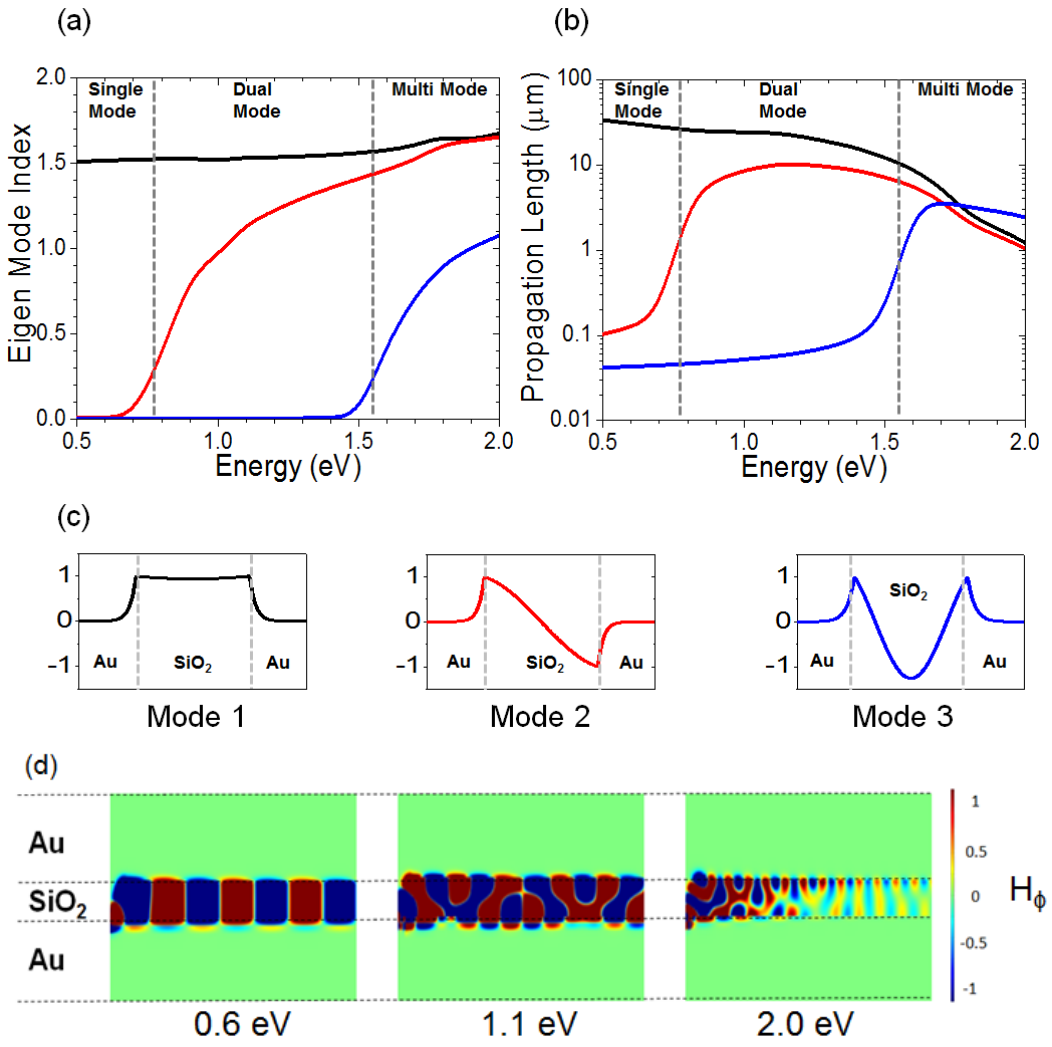

Figure 4.1: Eigenmode analysis of intrinsic modes supported by the Au-SiO_2-Au MIM waveguiding segment calculated in theory. (a) Mode index vs photon energy. (b) Propagation length vs photon energy. Dashed lines indicate cut-off energies of the three regimes. (c) Theoretical mode profile of modes 1, 2 and 3. Mode 1 achieves the longest propagation length of 30 μm at 0.6 eV. Dashed lines indicate different material interfaces. (d) Image plots for real values of H_ϕ captured between 0 to 5μm away from the source at photon energies of 0.6 eV, 1.1 eV and 2.0 eV [4.5].

The three regimes of the MIM waveguiding segment indicate the possibility of exciting either single or multiple plasmon-polariton modes with respect to applied voltage bias. The applied bias affects the maximum energy of plasmon polaritons excited by the tunnelling current. For each of these different modes, we can identify their individual mode profiles as shown in

Fig. 4.1(c). Modes 1 and 3 are seen to be even while mode 2 is odd with a strong dip in the centre.

For this pMIM structure, the tunnelling current excites transverse magnetic (TM) waves which have a magnetic field component H_ϕ perpendicular to the plane of incidence and an electric field E_r parallel to the plane of incidence in the direction of the propagating waves. The image plots for magnetic field H_ϕ excited at the photon energies of 0.6, 1.1 and 2.0 eV for an Au-SiO2-Au configuration are illustrated in Fig. 4.1(d). With this pMIM design, it can be shown that different plasmon polariton modes can be electrically excited for different applied biases. The presence of multiple propagating modes allows waveguide mode manipulation for parallel data transmission and wider communication bandwidth [4.6], [4.7].

In the above discussions, an eigenmode analysis has been performed for the Au-SiO_2-Au MIM waveguiding segment, giving the intrinsic eigenmodes. The values of mode index and propagation length were theoretically obtained from calculation of the complex wavenumber k_x for eigenwaves propagating in the MIM waveguiding segment and compared with those derived in simulation by fitting spectra of the excited magnetic field as shown in Fig. 4.2.

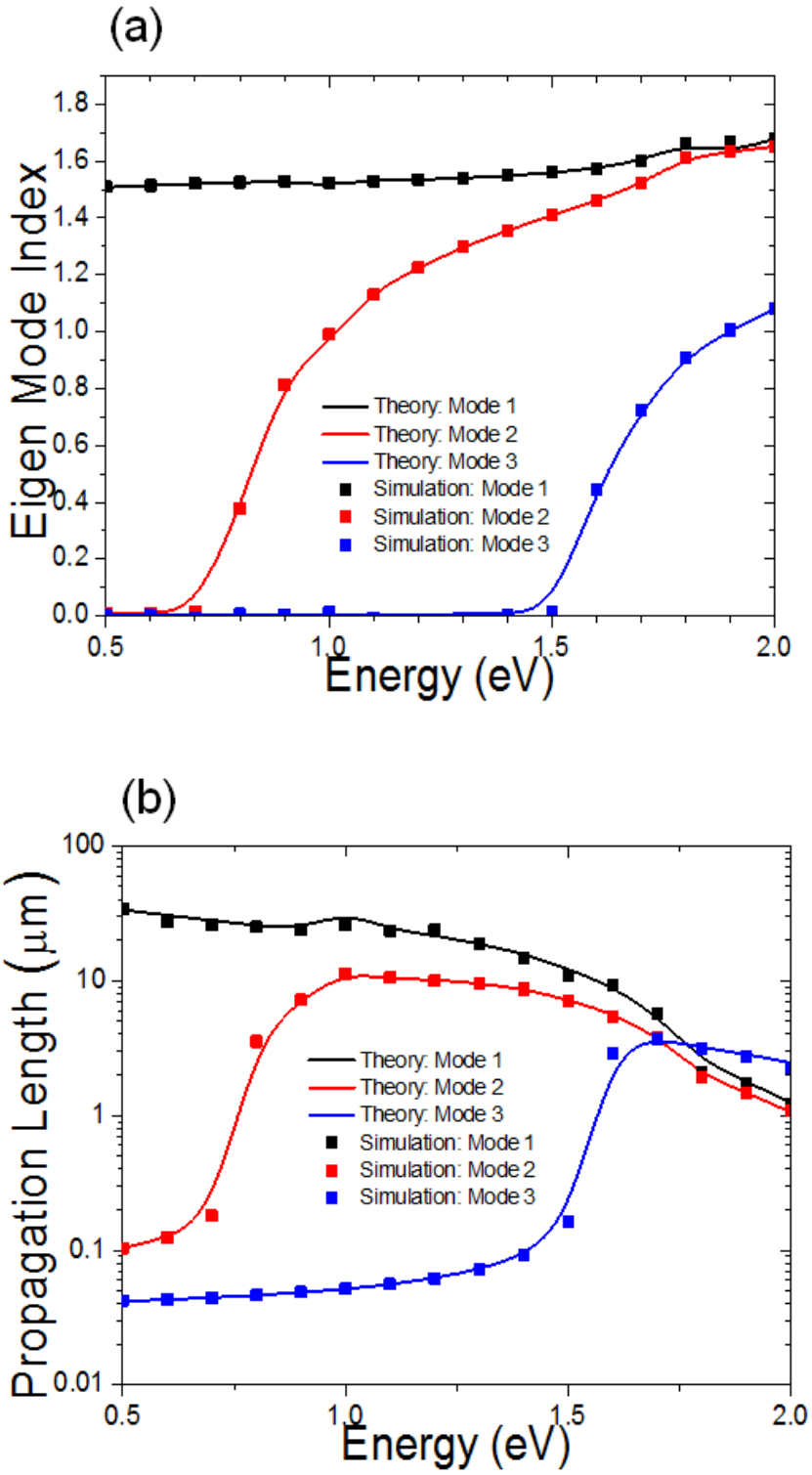

Figure 4.2: Eigenmode analysis of intrinsic modes supported by Au-SiO_2-Au MIM waveguiding segment of the pMIM calculated in theory and in simulation. (a) Mode index as a function of photon energy for first three modes. (b) Propagation length vs photon energy for first three low-order modes [4.5].

The pMIM structure has a stronger emission than the MIM stucture and all the coupled power can be used to efficiently excite eigenmodes of the MIM waveguiding segment of the pMIM. To demonstrate the excitation efficiency, an energy value corresponding to each operation regime is selected as a reference. Hence, 0.6 eV, 1.1 eV and 2.0 eV are selected for energies lying within the boundaries of single, dual and multimode regimes respectively. Photon energy of 0.6 eV shows excitation of a single propagating SPP mode while energies of 1.1 eV and 2.0 eV show excitation of multiple eigenmodes as shown in Fig. 4.1(d). To obtain further insights into the types of excited modes, individual modes are extracted from the image plots of the real values of H_ϕ shown in Fig. 4.1(d). The real values of the H_ϕ field profile corresponding to image plots at 0.6 eV, 1.1 eV and 2.0 eV along the direction of the propagating waves are as shown in Figs. 4.3(a), (b) and (c), respectively. The H_ϕ field profile is calculated at the top interface between Au cathode and SiO_2 insulator for distances up to 50 μm away from the tunnelling current source.

To investigate excited fields in the pMIM structure, a Fourier analysis on the complex H_ϕ field profile is performed. To study the mode index of the waves excited by the source, a Fast Fourier Transform was performed for the complex magnetic field $H_\phi(\mathrm{r})$ obtained from FEM simulation along the MIM waveguiding segment of the pMIM at different photon energies. To extract the complex mode index of the excited plasmon-polaritons, the Fourier images were fitted with the Fourier image of omnidirectionally propagating eigenwaves in the MIM waveguiding segment of pMIM with the complex wavenumber k_x,

$$H(k_r, z_0) = \frac{1}{\sqrt{2\pi}} \int_{\frac{1}{Re(k_x)}}^{\infty} H(r, z_0) e^{-ik_r r} dr =$$

$$\frac{1}{\sqrt{2\pi}} \int_{\frac{1}{Re(k_x)}}^{\infty} H_0(z_0) H_0^1(k_x r)\, e^{-ik_r r} dr \approx -\frac{1+i}{\sqrt{2\pi}} \frac{H_0(z_0)}{\sqrt{k_x(k_r - k_x)}} \qquad (4.1)$$

For all the regimes, curve fitting demonstrated excellent agreement for both complex magnetic field $H_\phi(\mathrm{r})$ as shown in Fig. 4.4 and complex wavenumber k_x as shown in Fig. 4.2, as well as confirmed the number of excited waves in all three regimes considered.

The normalised absolute values of the Fourier transform (F.T) are plotted against mode index and shown in Figs. 4.3(d), (e) and (f) for energies of 0.6 eV, 1.1 eV and 2.0 eV respectively. An energy of 0.6 eV shows a single peak around mode index of 1.5 while an energy of 1.1 eV shows two peaks corresponding to the mode indices of 1.1 and 1.5. The peak at mode index 1.5 is a result of mode 1 while the new peak at mode index 1.1 is a result of mode 2. At an energy of 2.0 eV, only two peaks at mode indices 1.6 and 1 are seen. The peak seen at 1.6 can be attributed to both modes 1 and 2 having very similar mode indices at energy 2.0 eV as shown in Fig. 4.1(a) while the peak at mode index 1.0 is due to mode 3. The obtained spectra align closely with those of omnidirectionally excited eigenwaves calculated from theory. Also, this is in accordance with the study in Fig. 4.1(a) where it is observed that only one, two and three modes are excited strongly in single, dual and multi mode regimes, respectively. Similarly, the normalised Fourier images of real and imaginery values of the F.T of H_ϕ are in accordance with both theory and simulation as shown in Fig. 4.4.

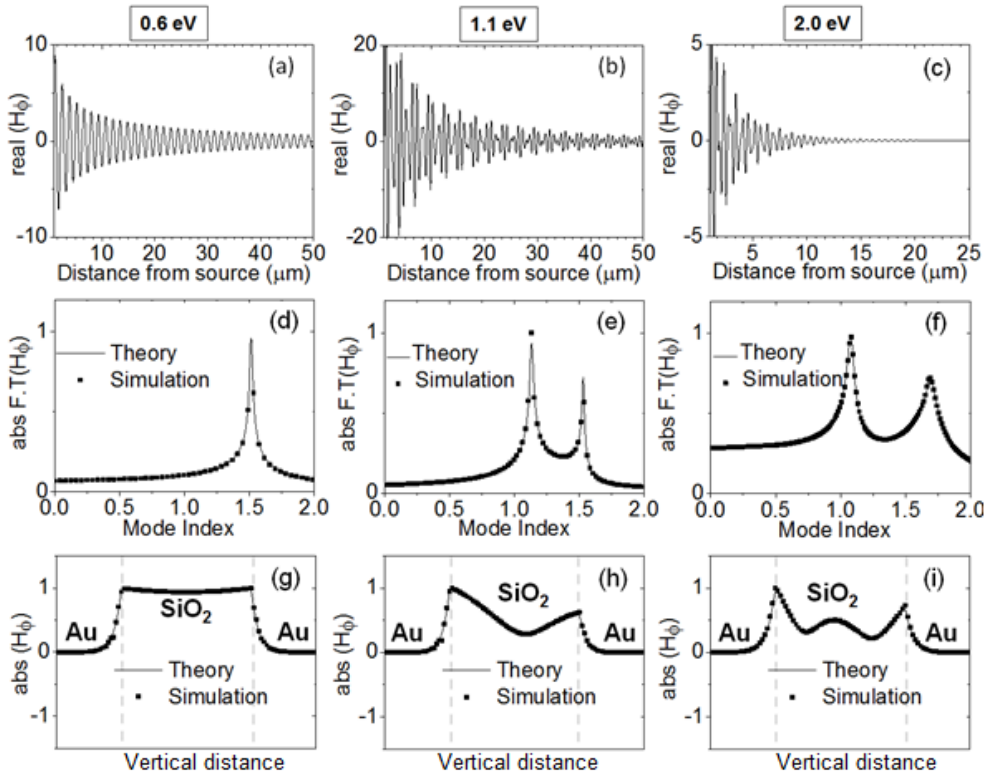

Figure 4.3: Field plots of real(H_ϕ) vs propagating distance at photon energies of (a) 0.6 eV, (b) 1.1 eV, (c) 2.0 eV; normalised absolute value of Fourier transformed (H_ϕ) vs mode index for (d) 0.6 eV, (e) 1.1 eV, (f) 2.0 eV; $|H_\phi|$ across vertical interface for (g) 0.6 eV, (h) 1.1 eV, (i) 2.0 eV. The simulated mode profile closely mirrors the theoretical mode profile, demonstrating the existence of excited eigenmodes in the different regimes and the obvious absence of leaky modes [4.5].

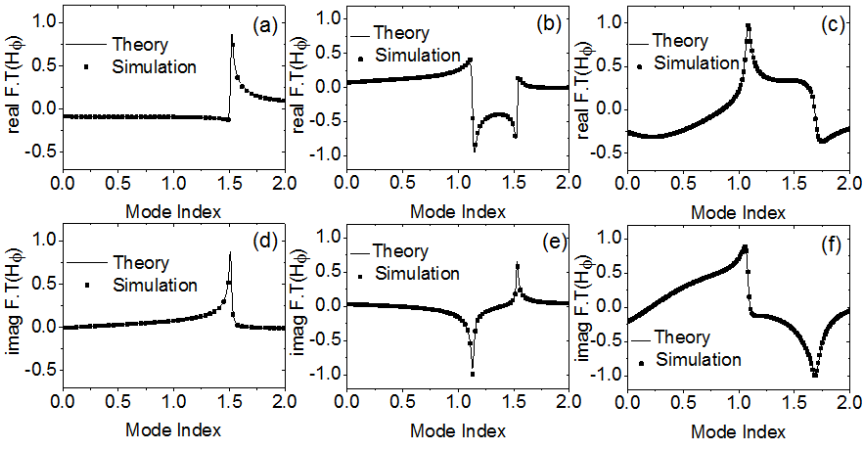

Figure 4.4: Normalised Fourier images of Re(H_ϕ) as a function of mode index for photon energies of (a) 0.6 eV, (b) 1.1 eV, (c) 2 eV; normalised Fourier images of Im(H_ϕ) vs mode index for (d) 0.6 eV, (e) 1.1 eV, (f) 2 eV [4.5].

To further confirm that the theoretically calculated modes have been observed, H_ϕ mode profile across the vertical interfacesis was considered. For an accurate study, appropriate field monitors were placed at suitable distances away from the tunnelling current source. The propagation lengths of each excited mode were determined in order to know how far they propagated and the extent of their influence on the mode profile with propagation length. In accordance with Fig. 4.1(b), mode 1 has a propagation length of 30 μm at 0.6 eV. At 1.1 eV, mode 1 and mode 2 have a propagation length of 20 μm and 8 μm respectively. At 2.0 eV, mode 1 and mode 2 have similar propagation lengths of 2 μm while mode 3 has a propagation length of 1 μm. This means that modes 1 and 2 diminish when the energy increases while mode 3 only starts to show its influence at higher energies.

Hence, in order to observe the individual contributions to the mode profile for real values of H_ϕ, monitors were placed 5μm away from the source for energies 0.6 eV and 1.1 eV and monitors were placed 0.5 μm away from the source for energy 2.0 eV. Superposition was then performed for the theoretically calculated individual mode profiles shown in Fig. 4.1(c) for particular energies. The final mode profile for absolute values of H_ϕ calculated in theory is shown together with simulated values in Figs. 4.3(g), 4.3(h) and 4.3(i) for energies of 0.6 eV, 1.1 eV and 2.0 eV. Similarly, the mode profiles for real and imaginery values of H_ϕ are in accordance with both theory and simulation as shown in Fig. 4.5.

To arrive at these mode profiles, a field analysis of the onmidirectional excited waves was performed. To analyze the excited waves in the MIM waveguiding segment of pMIM by a compact source, the complex magnetic

field $H_\phi(z)$ obtained from FEM simulations across the MIM waveguiding segment was investigated at different photon energies. Those field profiles were fitted with the corresponding distributions of magnetic field $H_y(z)$ taken from the eigenvalue analysis for several low-order modes. This fitting showed excellent agreement between the eigenvalue theory and FEM simulation shown in Fig. 4.5 and confirmed the excitation of one eigenwave in the single mode regime, two eigenwaves in the dual mode regime, and three eigenwaves in the multi mode regime.

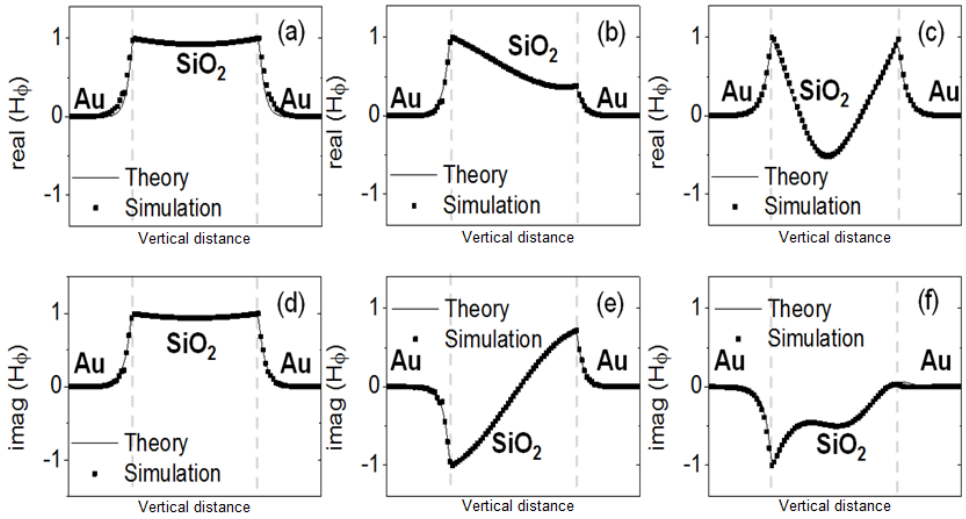

Figure 4.5: Real part of H_ϕ across the MIM structure for photon energies of (a) 0.6 eV, (b) 1.1 eV, (c) 2 eV; imaginary part of H_ϕ across vertical interface for (d) 0.6 eV, (e) 1.1 eV, (f) 2 eV [4.5].

For both real and imaginery values of H_ϕ, the simulated mode profile closely mirrors that of the theoretical mode profiles, further demonstrating the efficient excitation of the confined eigenwaves with absence of leakage radiation.

From the information obtained thus far, long travelling waves of more than 10 μm can be electrically excited at relatively low voltage bias and hence low energies. Taking Au-SiO_2(500 nm)-Au MIM waveguiding segment of the

pMIM as an example, the operation voltage bias for the single-mode regime is 0.2 to 0.7 volts. These long travelling waves operating in the single mode regime are the focus of studies investigating propagating SPP excitations aimed at creating a low power compact on-chip propagating plasmon source.

4.3. Cut-off energies of different operating regimes

Having demonstrated that an externally applied bias induced tunnelling current can be used to excite desired eigenmodes in different operating regimes of a pMIM structure, design guidelines involving insulator thickness and permittivity are proposed to tune the cutoff energies of these regimes. The variation of cut-off energy with insulator thickness and insulator permittivity for the single and dual-mode regime is shown in Figs. 4.6(a) and 4.6(b) respectively. From the results obtained, it can be concluded that thinner insulators with lower permittivity values exhibit higher cut-off energies. This means that cut-off energies can be tuned to excite desired modes with the required voltage bias. Knowledge of cut-off energies signifies control over the number of modes excited [4.8].

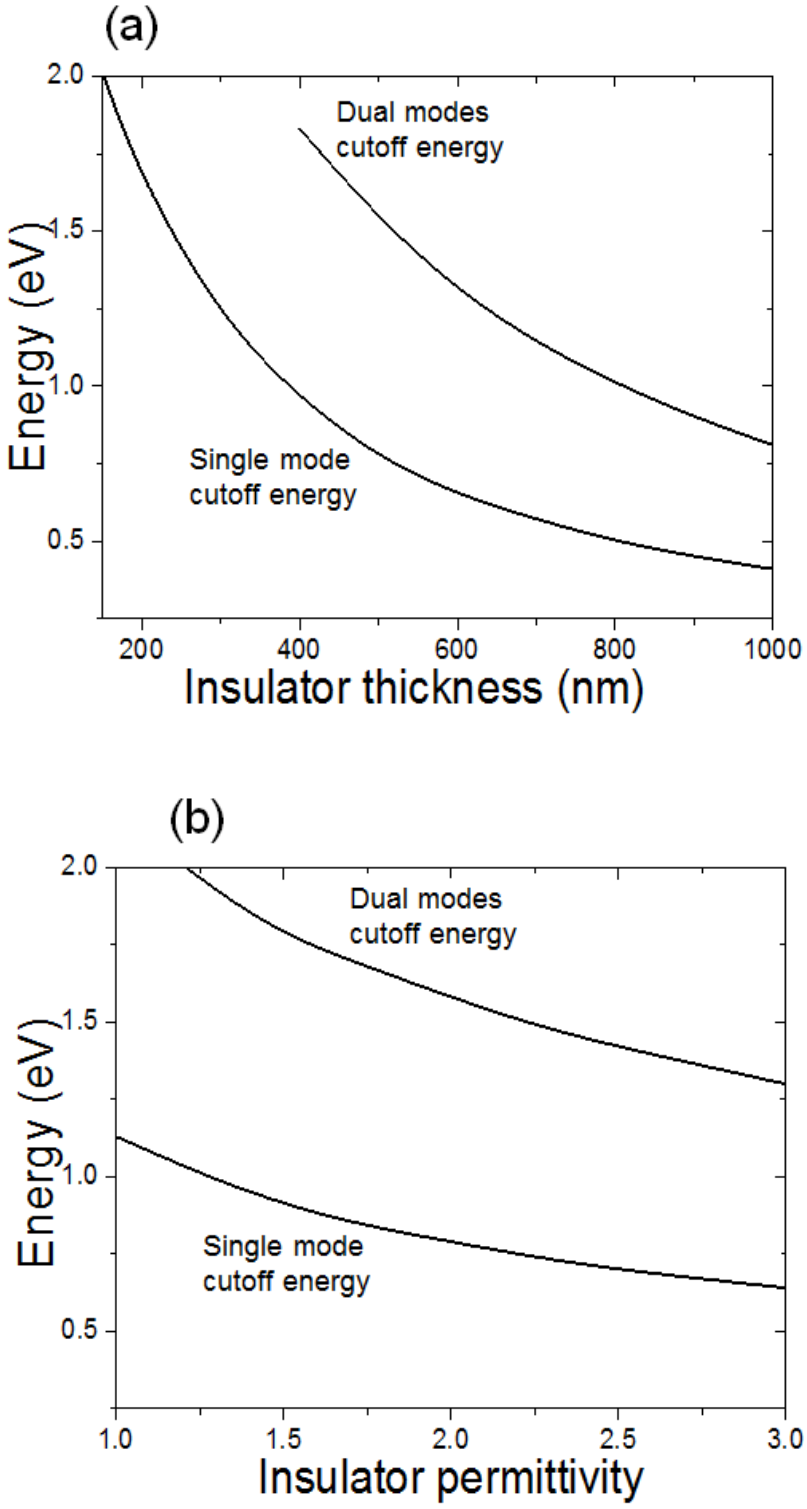

Figure 4.6: Cut-off energies of single and dual mode regimes as a function of (a) insulator thickness and (b) insulator permittivity. Thinner insulators with lower permittivity exhibit higher cut-off energies. This means that cut-off energies can be tuned to excite desired modes within a (low) required voltage bias [4.5].

4.4. Theoretical formulation of decomposition of excited waves into intrinsic eigenmodes

Since the energy spectra from 0.5 eV to 2 eV are of interest, power decomposition can be performed to determine the amount of power that goes into each eigenmode. To do so, a representation of the excited magnetic fields must first be obtained. The excited field representation is as shown in Eqn. 4.2 and is only valid in the absence of radiation modes. This means that all power goes into the excitation of eigenmodes.

$$H_\phi(r,z) = \sum_n A_n H_n(r,z), r \geq r_0 \qquad (4.2)$$

H_ϕ refers to the excited magnetic field while H_n refers to the magnetic eigenfields with mode number *n*; *r* is the radial distance away from the tunnelling current source. For these eigenfields to hold, they must first be orthogonal. This means that eigenfields of mode number *n* and *m* have to satisfy the relationship given by

$$\int_{-\infty}^{\infty} H_n(r,z)H_m(r,z)\,dz = 0, n \neq m. \qquad (4.3)$$

Once the eigenfields are proven to be orthogonal, the decomposition coefficients, A_n can be derived for eigenfields of mode number *n* based on

$$A_n = \frac{\int_{-\infty}^{\infty} H_\phi(r_0,z)H_n(r_0,z)dz}{\int_{-\infty}^{\infty} {H_n}^2(r_0,z)dz}. \qquad (4.4)$$

Thereafter, we can obtain the integrated power flux *I* based on Eqn. 4.5 provided that Eqns. 4.6 and 4.7 are satisfied.

$$I_n = 2\pi r_0 |A_n|^2 \int_{-\infty}^{\infty} S_{rn}(r_0,z)\,dz \qquad (4.5)$$

$$I_0 = 2\pi r_0 \int_{-\infty}^{\infty} S_{r\emptyset}(r_0,z)\,dz \qquad (4.6)$$

$$I_0 = \sum_n I_n, \tag{4.7}$$

where S_{rn} and $S_{r\emptyset}$ refer to the time average Poynting vector/power flow in the radial direction for eigenfields with mode number *n* and excited eigenwaves, respectively. The Poynting vector is the instantaneous power flow due to instantaneous electric and magnetic fields. I_n and I_0 refer to the integrated power flux for the eigenfields and excited electromagnetic fields respectively. S_r can be calculated based on Eqn. 4.8 where the factor $\frac{1}{2}$ is due to the averaging of the sinusoidal waveforms [4.9].

$$\bar{S} = \frac{1}{2} Re\{\bar{E} \times \bar{H}^*\}$$

Using cylindrical coordinates of $r, \emptyset, z$,

$$\bar{S} = \tfrac{1}{2} Re \begin{Bmatrix} \hat{r}(E_z {H_\emptyset}^* - E_\emptyset {H_z}^*) - \hat{z}(E_r {H_\emptyset}^* - E_\emptyset {H_r}^*) + \\ \widehat{\emptyset}(E_r {H_z}^* - E_z {H_r}^*) \end{Bmatrix}$$

$$S_r = \tfrac{1}{2} Re(E_z {H_\emptyset}^* - E_\emptyset {H_z}^*) \tag{4.8}$$

where sign convention dictates either inwards or outwards power flow.

4.5. Identification and efficient excitation of long travelling SPPs

The total power obtained numerically at the start of the interface of the waveguiding segment of the pMIM can be theoretically decomposed into individual constituents that go into the excitation of each eigenmode. Here we only consider the excitation of just three eigenmodes since they are the most dominant in the energy spectra of interest from 0.5 to 2 eV. These decomposed theoretical eigenmodes can be summed to obtain the total power which should agree very well with the total power obtained numerically. From the eigenmode analysis of the pMIM segment shown in Fig. 4.1, we can study the characteristics of each eigenmode. Mode 1 is essentially a surface mode across the energy spectrum of interest while mode 2 is essentially a volume mode up to 1.7 eV. From 1.7 eV to 2 eV, it behaves as a surface mode. Mode 3 behaves as volume mode across the energy spectrum. Extracting both excited eigenfields and eigenmodes using numerical FEM simulations and theoretical calculations allows us to arrive at the following decomposition for the triangular, concave and convex tip profiles which are shown in Fig. 4.7 to Fig. 4.9. These three tips are studied for their high coupling efficiency. The total theoretical power is calculated from the sum of power into the individual eigenmodes while the total numerical power is the power that is coupled into the MIM waveguiding segment.

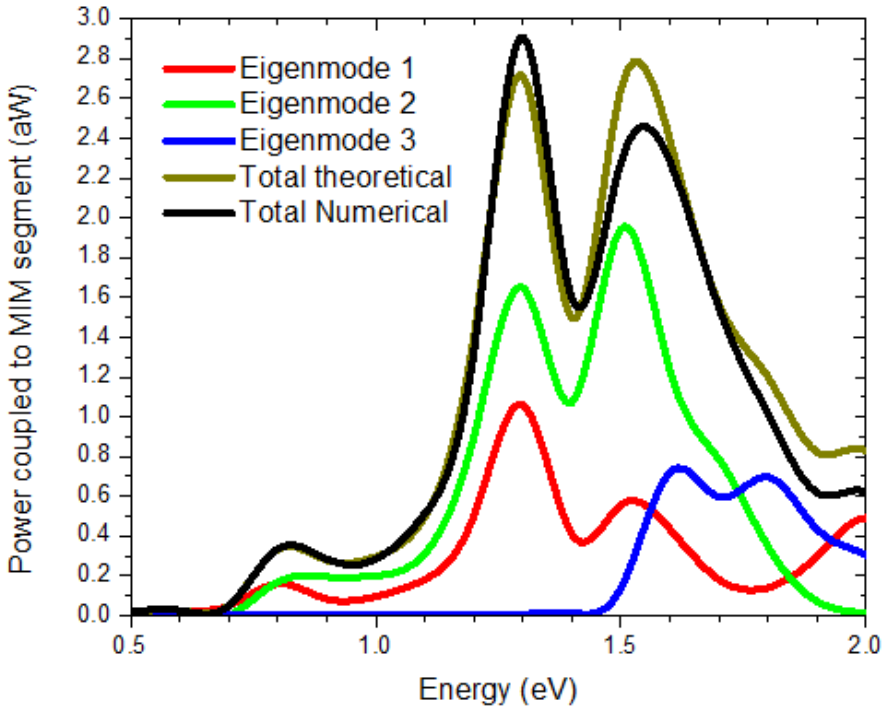

Figure 4.7: Eigenmode decomposition for pMIM with triangular tip profile

For the triangular tip shown in Fig. 4.7, the power profile in the single mode regime from 0.5 to 0.7 eV is dominated by mode 1. While it is desired to have just a single surface wave, this power is low. In the dual modes regime from 0.7 to 1.5 eV, volume mode 2 dominates surface mode 1. Mode 1 is still excited but the majority of the power goes into the excitation of mode 2. In the multimode regime from 1.6 to 2 eV, mode 3 dominates the power contribution beyond 1.7 eV. Beyond 1.7 eV, surface waves in modes 1 and 2 are still excited but with much lower power contributions than in the single or the dual-mode regime. Although the surface waves in multimode regime have higher frequency and hence higher group velocity, they transmit information faster but they have a high attenuation as well. There is a small difference between the total power calculated numerically and that extracted theoretically. This could be due to the need to consider the contribution of

more eigenmodes which make up the eigenwaves. Considering more eigenmodes contribution would make the two values even more similar.

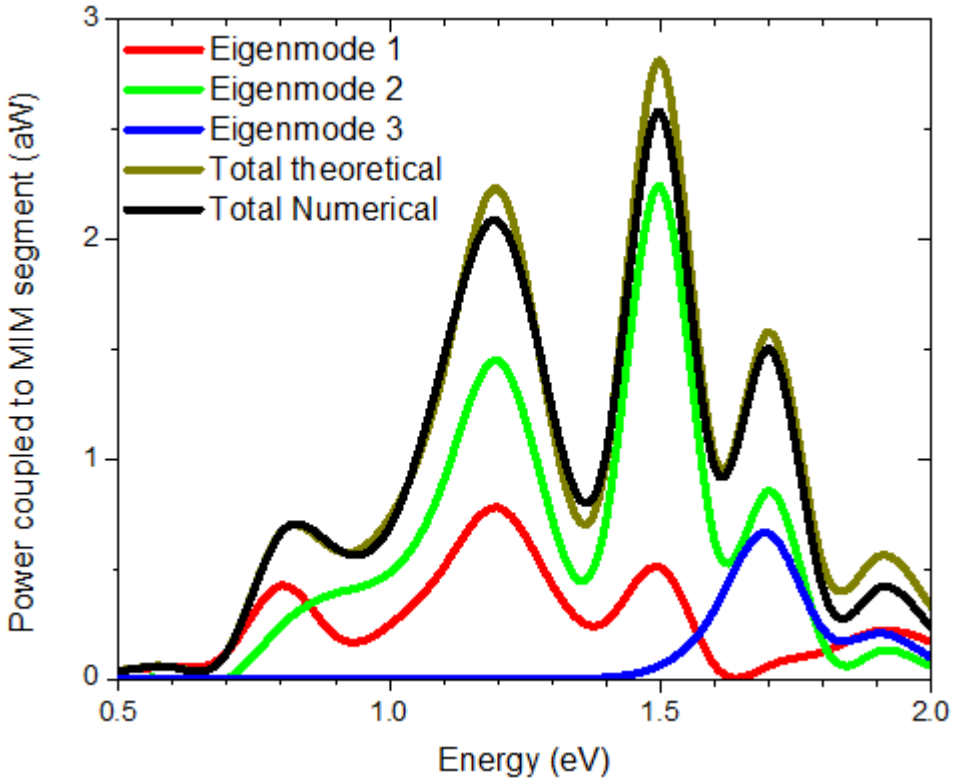

Figure 4.8: Eigenmode decomposition for pMIM with concave tip profile

For the concave tip referred to in Fig. 4.8, mode 1 dominates mode 2 for 0.7 to 0.9 eV of the dual mode regime. This means that we can make use of surface waves of mode 1 below 0.9 eV in the dual mode regime. The power contribution into excitation of mode 1 in the dual mode regime for concave tip is even greater than the power contribution of mode 1 for the triangular tip. This is true below 1.3 eV in the dual mode regime. The contribution to surface waves for mode 2 is similar to mode 1 in the multimode regime.

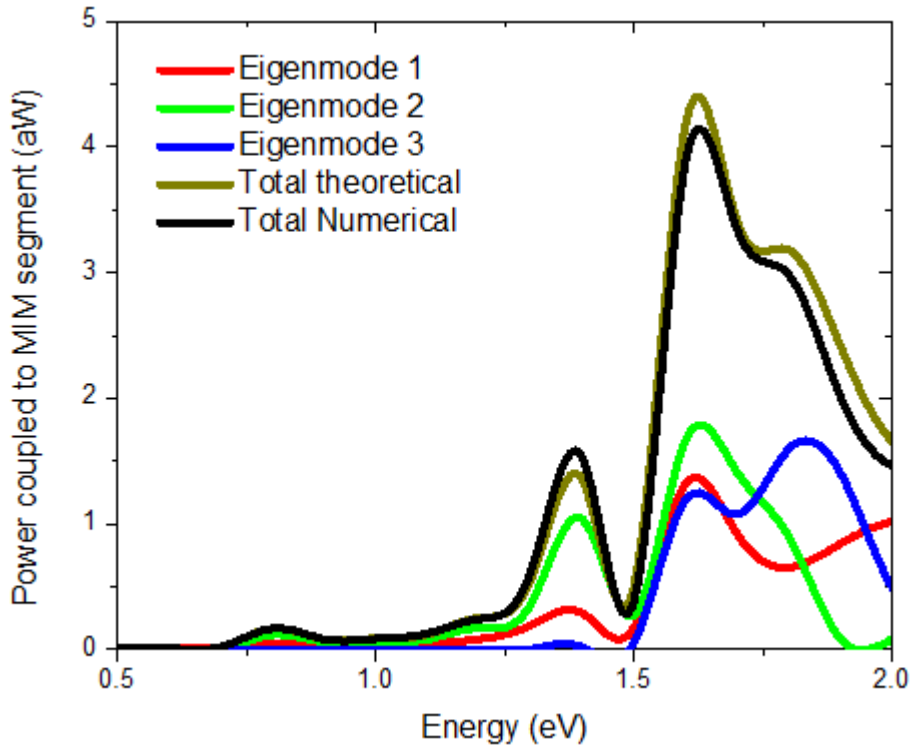

Figure 4.9: Eigenmode decomposition for pMIM with convex tip profile

For the convex tip profile shown in Fig. 4.9, power in the single mode regime is low compared to the dual and multimode regimes. Mode 2 dominates much of the dual-mode regime and contributes to surface modes from 1.7 eV to 1.8 eV. In the multi-mode regime, mode 3 dominates from 1.8 eV to 2 eV. To excite long travelling SPPs, it is best to operate in the single and dual-mode regime, with preference given to the single-mode regime. The concave tip profile allows for a dominant presence of mode 1 in both the single and dual-mode regimes which is desired for long propagation length.

4.6. Summary

Plasmon polaritons are excited in the MIM waveguiding segment in the form of eigenwaves which are made up of intrinsic eigenmodes. By controlling the applied voltage bias, desired modes in the single, dual and multimode regimes can be excited. Single and dual mode operation allows highly efficient excitation of long travelling SPPs. Cut-off energies of eigenmodes in pMIM structures can also be tuned by varying insulator thickness and permittivity in the MIM waveguiding segment. By decomposing eigenwaves into intrinsic eigenmodes, the circular concave tip can be used to excite single mode SPPs with propagation length up to 30 μm. These excited eigenmodes can be efficiently excited with no leakage radiation due to the thick metal layers. For on-chip applications, a thinner metal thickness has to be considered, however the leakage radiation can be made small to not affect the efficiency of propagating SPPs.

4.7. References

[4.1] S.A. Maier, *Plasmonics: Fundamentals and Applications* (Springer, 2007)

[4.2] C. Lin and T.K. Gaylord, "Multimode metal-insulator-metal waveguides: Analysis and experimental characterization," Physical Review B, 85(8), 085405 (2012)

[4.3] C. Xia, C. Yin, and V.V. Kresin, "Photoabsorption by volume plasmons in metal nanoclusters," Physical Review Letters, 102(15), 156802 (2009)

[4.4] S.V. Zhukovsky, A. Andryieuski, J.E. Sipe, and A.V. Lavrinenko, "From surface to volume plasmons in hyperbolic metamaterials: General existence conditions for bulk high k waves in metal dielectric and graphene dielectric multilayers," Physical Review B, 90(15), 155429 (2014).

[4.5] W.K. Phua, Y. Akimov, L. Wu, H.S. Chu, P. Bai and A. Danner, "Highly efficient tunable and localised on-chip electrical plasmon source using protruded metal-insulator-metal structure", Optics Express, 24(10), 10663-10674 (2016)

[4.6] E.P. Fitrakis, T. Kamalakis and T. Sphicopoulos, "Slow light in insulator-metal-insulator plasmonic waveguides", Journal of the Optical Society of America B, 28(9), 2159-2164 (2011)

[4.7] Y. Fang and M. Sun, "Nanoplasmonic waveguides: towards applications in integrated nanophotonic circuits," Light: Science and Applications, 4(6), e294 (2015).

[4.8] L.H. Gabrielli, D. Liu, S.G. Johnson, and M. Lipson, “On-chip transformation optics for multimode waveguide bends,” Nature Communications, 3, 1217 (2012).

[4.9] R. Ruppin, “Electromagnetic energy density in a dispersive and absorptive material”, Physics Letters A, 299(2), 309-312 (2002)

Chapter 5. Leakage radiation in pMIM structures with finite metal thickness

5.1. Introduction

The pMIM structure is able to efficiently excite plasmon polaritons with no leakage radiation due to the infinitely thick metal layers which were considered in theory and simulation. In order to adopt pMIM structures for use in on-chip applications, the thickness of the metal layers has to be realistically considered. A thin metal layer reduces the device footprint when adopted for use on the optoelectronic integrated circuits. However, when the metal layers become thinner, undesired leakage radiation [5.1-5.3] could arise. Leakage radiation is actually emitted power from the excitation source that is lost due to emission into the surroundings. This serves to lower the efficiency of the excited plasmon polaritons and results in damping of the plasmon propagation lengths.

A pMIM structure with finite substrate thickness and no detectable leakage radiation allows plasmon polaritons to be excited with high efficiencies and results in negligible power loss. While leakage radiation that comes with pMIM structures of finite substrate thickness is generally undesirable, it also serves a purpose in allowing detection of excited SPPs, as is commonly used in leakage radiation microscopy [5.1, 5.4-5.7]. However, apart from excited plasmon polaritons, leakage radiation has an additional component which is often neglected in the form of direct emission of the

excitation source. The direct emission is most prominent at energies located off resonances of excited plasmon polaritons and is particularly relevant in the pMIM structure due to the presence of the exciting tunnelling current. Apart from the direct emission of the excitation source, resonant peaks due to localised SPPs at the protruded tip as discussed in Ch. 3 may also be detected. Since most leakage radiation studies are concerned with resonant peaks due to propagating SPPs, the resonant peaks due to localised SPPs may be misinterpreted as propagating SPPs in the MIM waveguiding segment.

5.2. Detection of leakage radiation

Leakage radiation is experimentally measured by using a spectrum collection system which consists of an inverted optical microscope equipped with a spectrometer and an electron multiplying charge coupled device CCD (EMCCD) [5.8]. The CCD converts detected photons into electron charges which are then measured. These detected photons are generated when the tunnelling electrons lose energy and couple onto plasmon states. In order to detect these photons, the finite Au substrate is deposited on top of an optical adhesive (OA)/glass substrate. The setup to detect leakage radiation is shown in Fig. 5.1 using the pMIM structure with a triangular tip as an example. Leakage radiation originates from the direct emission of excitation source and excited plasmon polaritons. Direct leakage radiation from excitation source should not be neglected.

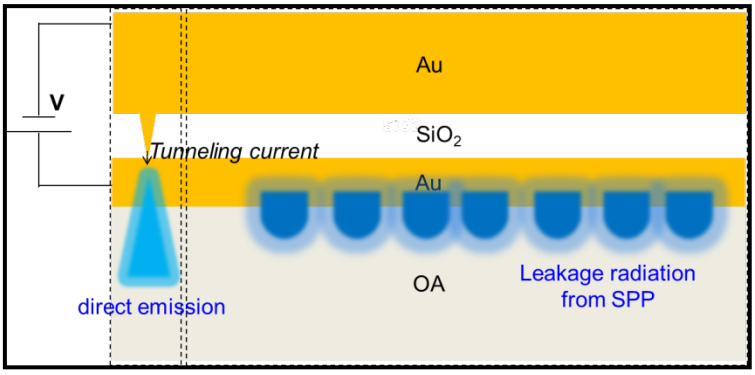

Figure 5.1: Schematic of leakage radiation from the pMIM structure

By performing a parametric sweep of Au substrate thicknesses from 5nm to 100nm, substantial (more than 10 % deviation in $|H_{\emptyset}|$ profile) leakage radiation can be observed for Au substrate thicknesses less than 70 nm, which is comparable to the skin depth [5.9] of Au at 1 THz [5.10]. For the

subsequent discussions, focus will be placed on specific Au substrate thicknesses of 5 nm and 50 nm which are smaller than skin depth and thicknesses of 100 nm, 250 nm and 500 nm which are larger than skin depth.

Leakage radiation from both direct emission and excited plasmon polaritons is evident from both $|H_{\emptyset}|$ and $|F.T(H_{\emptyset})|$ profile as thickness of Au substrate decreases as shown in Fig. 5.2 and Fig. 5.3, respectively. From Fig. 5.2, the $|H_{\emptyset}|$ profile indicates the theoretical mode profile of mode 1 at 0.6 eV. This is similar in Fig. 5.3 where the peak seen at mode index 1.5 due to mode 1 at 0.6 eV becomes less sharp for Au substrate thicknesses of 50 nm and 5 nm.

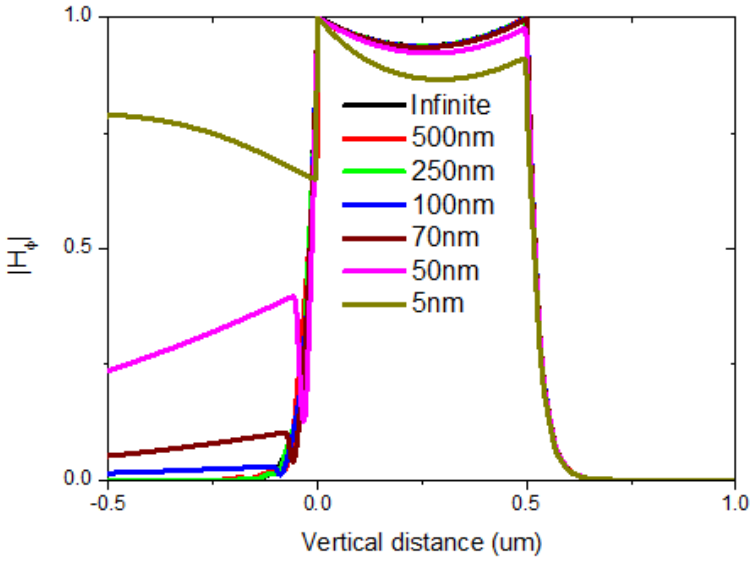

Figure 5.2: Evidence of leakage radiation as exhibited in $|H_{\phi}|$ profile for varying substrate thickness for the mode at 0.6 eV.

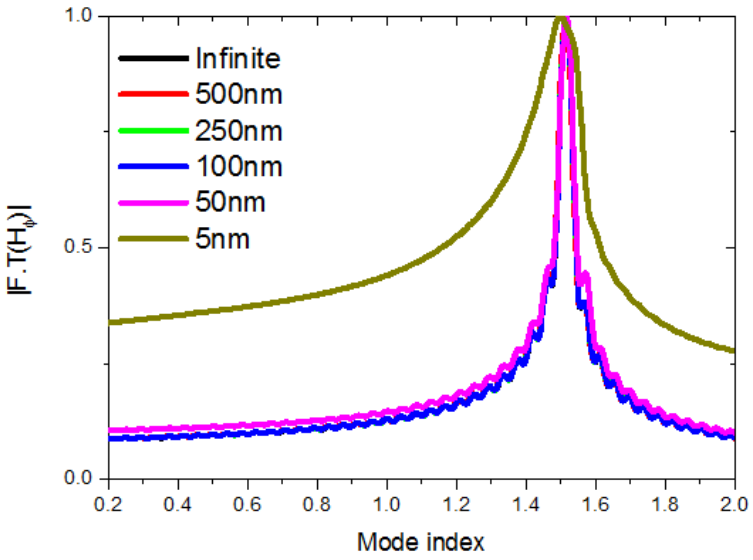

Figure 5.3: Evidence of leakage radiation as exhibited in normalised absolute value of Fourier transformed (H_ϕ) vs mode index varying substrate thickness for the mode at 0.6 eV.

5.3. Investigation of finite substrate thicknesses

Investigating the effects of substrate thickness on emitted power as shown in Fig. 5.4 and using the tunnelling current density at 0.2 eV for a 1 nm gap, the emitted power shows an additional resonant peak with thinner substrates at 2.3 eV once substrate thickness becomes less than skin depth. This additional peak is due to the enhanced emitted power as a result of the excitation of plasmon polaritons at the bottom Au/glass interface of pMIM on glass substrate since 2.3 eV corresponds to the SPP peak at the Au/glass interface. There is a sharp peak for the 5nm Au substrate because the Au substrate has decreased to less than the skin depth, leading to the enhanced emitted power. The resonant peaks at 0.8 eV and 1.3 eV are seen to exhibit a lower emitted power for a 5 nm Au substrate than the 50 nm Au substrate. This could be due to the substantial leakage radiation diminishing the total emitted power.

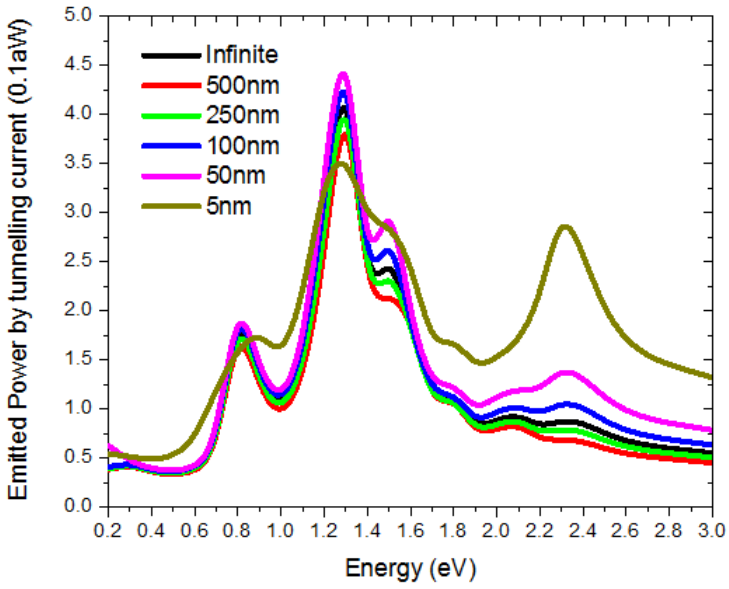

Figure 5.4: Emitted Power (aW) vs Energy (eV) for pMIM structure with a triangular tip for varying substrate thickness if tunnelling current is kept constant at 0.2 eV across different energies

To investigate the effects of substrate thickness on leakage radiation, leakage radiation integrated over the surface 250 nm below the Au substrate at the Au/OA interface for a pMIM structure with a triangular tip is extracted (in simulation). The distance of 250 nm is chosen to have a reasonable detection magnitude of the leakage radiation. The extracted leakage radiation as a function of Au substrate thickness is shown in Fig. 5.5. Since leakage radiation is made up of both direct emission and plasmon polaritons, there is a need to compare emitted power from tunnelling current, power coupled into MIM waveguiding segment and leakage radiation spectra. The presence of a finite Au substrate leads to a shift to higher energies for all detected resonant peaks due to leakage radiation affecting the efficiency of plasmon polariton excitation which results in a less collective and broader resonance. Excited plasmon polaritons along the top Au/SiO_2 interface, SiO_2/bottom Au interface, Au tip/SiO_2 interface have all been detected but they are seen to shift from 0.8 eV, 1.3 eV and 1.5 eV to higher energies at 1.2 eV, 1.6 eV and 1.8 eV, respectively for a 5 nm Au thickness. The thinner the Au substrates, the stronger the contribution from both direct emission and plasmon polaritons. When Au substrates become very thin at 5 nm, the contribution of propagating SPPs along the SiO_2/bottom Au interface increases significantly while the localised SPPs along the Au tip/SiO_2 interface becomes more dominant than that of the top Au/SiO_2 interface.

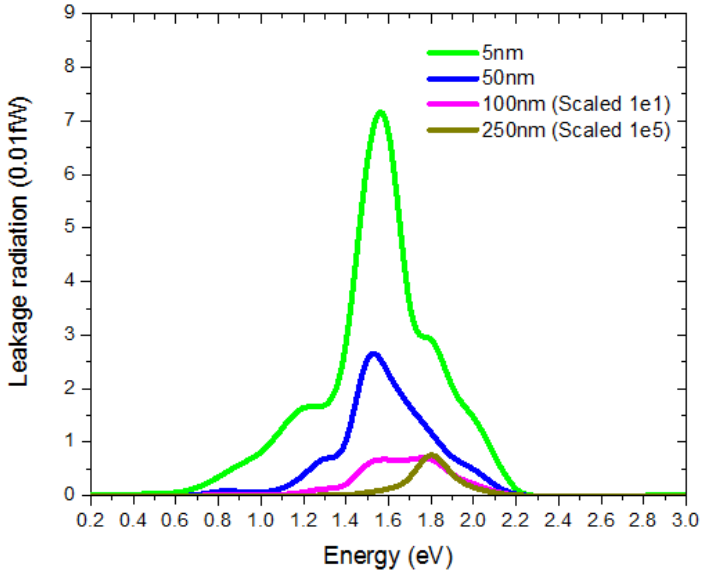

Figure 5.5: Leakage radiation (fW) vs Energy (eV) for pMIM structure with a triangular tip for varying substrate thickness

To investigate how different tip profiles at different substrate thicknesses affect the leakage radiation spectra, the leakage radiation profile of different tips were studied for 5 nm, 50 nm, 100 nm and 250 nm Au substrate thicknesses as shown in Fig. 5.6, Fig. 5.7, Fig. 5.8 and Fig. 5.9 respectively. Triangular, concave and convex tip profiles are seen to provide more dominant contributions to leakage radiation than the rectangular tip profile or if there was no tip.

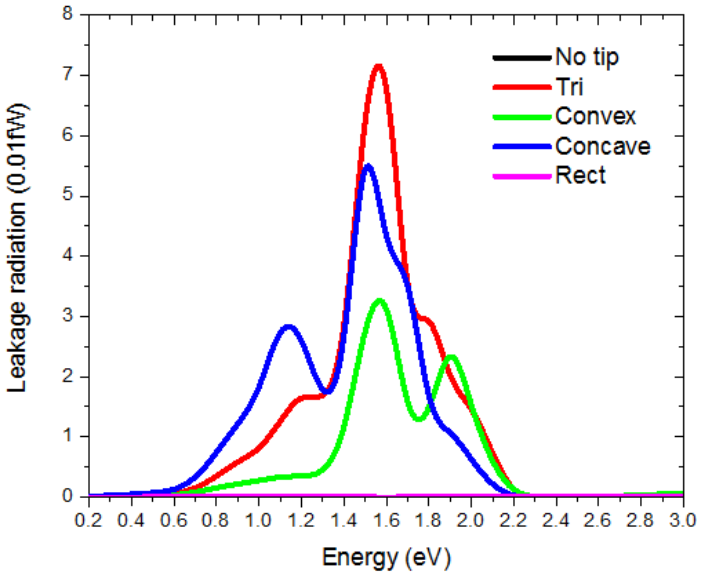

Figure 5.6: Leakage radiation for different tips for a 5 nm Au substrate thickness

For the three dominant convex, triangular, and concave tip profiles, the resonant peak along top Au/SiO_2 interface shifts from 0.8 eV to 1.1 eV and 1.2 eV for concave and triangular tips, respectively. The resonant peak for a convex tip diminishes due to the small radiation magnitude at the resonant energy. There are fewer shifts for all resonant peaks of the concave tip profile due to its shape which leads to a more localised resonance. Along the SiO_2/bottom Au interface, the resonant peaks shift from 1.4 eV, 1.3 eV and 1.2 eV to 1.6 eV, 1.6 eV and 1.5 eV for the convex, triangular, and concave tip profiles, respectively with the triangular tip exhibiting the strongest leakage radiation followed by the concave and convex tips. Along the Au tip/SiO_2 interface, the resonant peaks shift from 1.6 eV, 1.5 eV and 1.5 eV to 1.9 eV, 1.8 eV and 1.8 eV for the convex, triangular, and concave tip profiles, respectively.

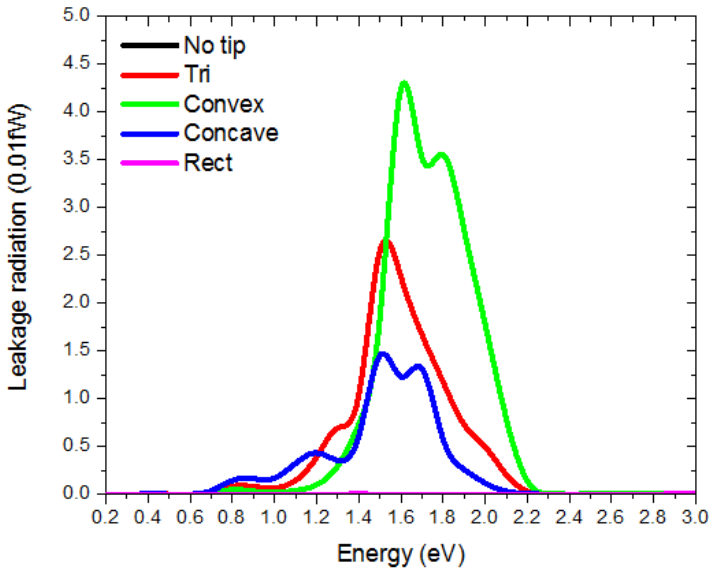

Figure 5.7: Leakage radiation for different tips for 50 nm Au substrate thickness. Leakage radiation for "Rect" and "No tip" profiles are negligible as compared to "Tri", "Convex" and "Concave" tip profiles.

As the Au thickness increases to 50 nm, the resonant peak along the top Au/SiO_2 interface remains the same for all three tip profiles, albeit at a lower magnitude. Along the SiO_2/bottom Au interface, the resonant peaks remain the same but the magnitude decreases for both the triangular and concave tips, but not the convex tip. This could be due to the convex tip profile having stronger resonances at higher energies. Upon normalisation with the tunnelling current density which shows exponential increase at large energies, the resonant peaks for the convex tip profile is much stronger than those of the triangular and concave tips. Such phenomena occur similarly along the Au tip/SiO_2 interface for the resonant peak of the convex tip at 1.9 eV. The resonant peak for the triangular tip diminishes while that of the concave tip remains approximately the same.

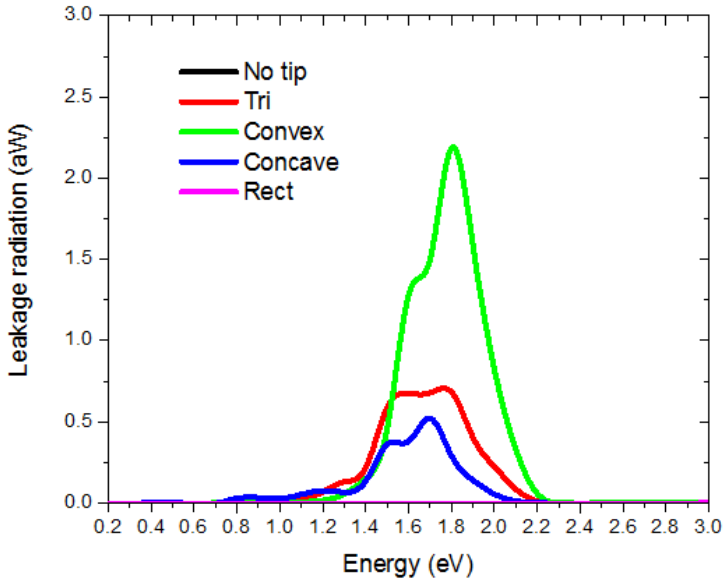

Figure 5.8: Leakage radiation for different tips of 100 nm Au substrate thickness. Leakage radiation for "Rect" and "No tip" profiles are negligible as compared to "Tri", "Convex" and "Concave" tip profiles.

At even larger substrate thicknesses of 100 nm, the resonant peak along the top Au/SiO_2 interface diminishes, leaving just the resonant peaks along the SiO_2/bottom Au interface and the Au tip/SiO_2 interface. The resonant peaks along the SiO_2/bottom Au interface are still visible but are very much reduced in magnitude. These resonant peaks along the SiO_2/bottom Au interface become even smaller than that of the Au tip/SiO_2 interface. This shows that at 100 nm Au thickness, leakage radiation becomes very much reduced with the contribution of excited localised SPPs from direct emission slightly exceeding those of propagating SPPs.

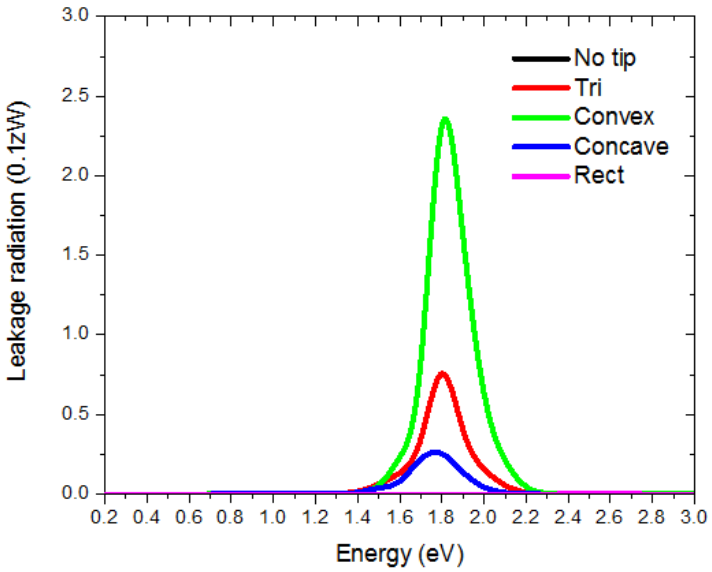

Figure 5.9: Leakage radiation for different tips of 250 nm Au substrate thickness. Leakage radiation for "Rect" and "No tip" profiles are negligible as compared to "Tri", "Convex" and "Concave" tip profiles.

For a large Au substrate thickness of 250 nm, only resonant peaks along the Au tip/SiO_2 interface can be detected and the leakage radiation readings are very small, meaning leakage radiation studies do not provide much information for large substrate thickness.

With finite substrates of decreasing thickness, peaks shift to higher energies in the leakage radiation spectra than that of spectra for emitted power and coupled power into the MIM waveguiding segment. Leakage radiation is observed to exhibit a higher intensity as seen for thinner Au substrates less than skin depth, particularly thicknesses of 5 nm and 50 nm. This is due to the stronger contribution of leakage radiation from excited plasmon polaritons in the MIM waveguiding segment. When the metal thickness in the pMIM structure is larger than 100 nm or around 150% of the SPP skin depth, the leakage radiation becomes negligible.

For substrate thickness approximately equal to or larger than skin depth, the convex tip profile provides strongest detection of leakage radiation for excited plasmon polaritons along the Au tip/SiO_2 interface. At substrate thicknesses larger than skin depth, the resonant peak along the top Au/SiO_2 interface diminishes.

For substrate thickness smaller than skin depth, excited plasmon polaritons along SiO_2/bottom Au interface show greater dominance than that of the Au tip/SiO_2 interface. This means that finite Au substrate thicknesses smaller than skin depth have to be adopted in order detect plasmon polaritons that is largely excited in the MIM waveguiding segment rather than at the tip.

5.4: Summary

Studies show that leakage radiation depends on the skin depth of SPPs in metal. When the bottom Au anode thickness in the pMIM structure is larger than 150% of the SPP skin depth of Au at 1THz, the leakage radiation becomes negligible. For an Au-SiO_2-Au pMIM structure, the Au thickness should be larger than 100 nm. Although the leakage radiation is undesired, it can be used to detect excited propagating SPPs in pMIM structures. When the bottom Au anode is thinner than the skin depth, the propagating SPPs that are largely excited in the MIM waveguiding segment can be detected rather than localised SPPs from the direct emission of the tunnelling current source. The use of a finite Au substrate thickness allows leakage radiation to be used as a means to detect excited propagating SPPs. A preliminary experiment is conducted to test such detection method in pMIM structures and is detailed in Ch. 6.

5.5. References

[5.1] A. Drezet, A. Hohenau, D. Koller, A. Stepanov, H. Ditbaucher, B. Steinberger, F.R. Aussenegg, A. Leitner and J.R. Krum, “Leakage radiation microscopy of surface plasmon polaritons”, Materials Science and engineering B, 149(3), 220-229 (2008)

[5.2] Q. Jiang, A. Pham, M. Berthel, S. Huant, J. Bellessa, C. Genet and A. Drezet, “Directional and singular surface plasmon generation in chiral and achiral nanostructures demonstrated by leakage radiation microscopy”, ACS Photonics, 3(6), 1116-1124 (2016)

[5.3] A. Hohenau, J.R. Krenn, A. Drezet, O. Mollet, S. Huant, C. Genet, B. Stein and T.W. Ebbesen, “Surface plasmon leakage radiation microscopy at the diffraction limit”, Optics Express, 19(25), 25749-25762 (2011)

[5.4] B. Hecht, H. Bielefeldt, L. Novotny, Y. Inouye and D.W. Pohl, “Local excitation, scattering and interference of surface plasmons”, Physical Review Letters, 77(9), 1889-1892 (1996)

[5.5] A. Bouhelier, T. Huser, H. Tamaru, H.J. Guntherodt, D.W. Pohl, F.I. Baida, and D. Van Labeke, “Plasmon optics of structured silver films”, Physical Review B, 63(155404), 1-9 (2001)

[5.6] A.L. Stepanov, J.R. Krenn, H. Ditlbacher, A. Hohenau, A. Drezet, B. Steinberger, A. Leitner and F. Aussenegg, “Quantitative analysis of surface plasmon interaction with silver nanoparticles”, Optics Letters, 30(12), 1524-1526 (2005)

[5.7] S. Massenot, J. Grandidier, A. Bouhelier, G. Colas des Francs, L. Markey, J.C. Weeber, A. Dereux, J. Renger, M.U. Gonzalez and R.

Quidrant, "Polymer metal waveguides characterization by fourier plane leakage radiation microscopy" Applied Physics Letters, 91(24), 243102 (2007)

[5.8] W. Du, T. Wang, H.S. Chu, L. Wu, R. Liu, S. Sun, W.K. Phua, L. Wang, N. Tomczak and C.A. Nijhuis, "On-chip molecular electronic plasmon sources based on self-assembled monolayer tunnel junctions", Nature Photonics, 10(4), 274-280 (2016)

[5.9] X.B. Xu, M. Liu, J.S. Luo, Y.Y. Wang, Z. Yi, X.B. Li, Y.G. Yi and Y.J. Tang, "Nanoscale energy confinement and hybridisation of surface plasmons based on skin depth in Au/Ag core-shell nanostructures", Plasmonics, 10(4), 797-808 (2015)

[5.10] M. Shalaby, H. Merbold, M. Peccianti, L. Razzari, G. Sharma, T. Ozaki, R. Morandotti, T. Feurer, A. Weber, L. Heyderman, B. Patterson and H. Sigg, "Concurrent field enhancement and high transmission of THz radiation in nanoslit arrays", Applied Physics Letters, 99(4), 041110 (2011)

Chapter 6. Preliminary experimental measurement of plasmon polaritons generated from pMIM structures

6.1. Introduction

To test the feasibility of the proposed pMIM design and to gain insights on the excited plasmon polaritons by examining experimentally-measured leakage radiation spectra, a partnership was established with collaborators to design, fabricate and measure excited plasmon polaritons from a practical pMIM structure that can be realised experimentally. Fabrication of very small gaps with a separation less than 1 nm between two electrodes has been difficult to realise without the use of molecular junctions [6.1, 6.2]. One such molecular junction which shows great potential is the self-assembled monolayer (SAM) which is exactly one molecule thick [6.3]. SAMs allows the tunnelling behaviour of the molecular junction to be controlled by tuning the chemistry of the molecule with an applied bias [6.3, 6.4]. The pMIM structure was fabricated with thin metal substrates so as to allow detection of excited SPPs via real and back focal plane images and extracted leakage radiation.

There exist different relations between detected SPPs and leakage radiation. One relation between leakage radiation spectra and propagating SPP resonant peaks has been proposed in a Kretschmann configuration whereby propagating SPP resonant peaks are often interpreted by an observation of a strong minimum in the leakage radiation spectra which is a function of the angle of incidence [6.5-6.12]. However, there have been many challenges to

this interpretation which in turn suggests that reflectance minimums in leakage radiation experiments do not correspond to propagating SPP resonant peaks [6.13-6.18]. Apart from Kretschmann configuration, propagating SPP resonant peaks were also proposed to be derived from the back focal plane images of the leakage radiation spectra [6.3, 6.19]. To better address concerns of the role of elastic and inelastic tunnelling processes on detected propagating SPPs from leakage radiation spectra, a theoretical formalism has been proposed to provide a correlation between propagating SPPs and the leakage radiation spectra in pMIM structures.

6.2. Practical material selection for study

Although materials such as Au and SiO_2 are adopted for use as the metal cathode and the insulator medium in both theoretical and numerical studies of MIM waveguiding segment and pMIM structures, they are not always practical for fabrication experimentally. Instead of the SiO_2 insulator which doubles as a tunnelling junction and a waveguiding medium, molecular tunnelling junctions in the form of self-assembled monolayers (SAMs) can be adopted as the tunnelling junction while polydimethylsiloxane (PDMS) insulator or air can be adopted for use as the waveguiding medium.

SAMs have been recently shown to exhibit properties that can be used to control the frequency of a tunnelling charge transfer plasmon mode [6.4]. The polarisation and frequency of the generated plasmon polaritons can also be controlled by varying the applied bias [6.3].

Due to the use of SAM as the molecular tunnelling junction, Eutectic Gallium Indium (EGaIn) is used in place of Au as the cathode. The use of EGaIn as a cathode is immensely useful as a contact for molecular junctions since it is a liquid metal with non-Newtonian behaviour. It flows when a shear stress is applied and behaves as a solid at rest. When EGaIn is brought into contact with SAM, it does not penetrate the SAM but instead deforms it, resulting in a well-defined junction. In air, EGaIn becomes passivated with a highly conductive 0.7 nm layer of native oxide, predominantly Ga_2O_3.

Au remains the material of choice for the anode while OA/glass is used as the substrate layer so as to detect leakage radiation as an indication of excited plasmon polaritons. OA refers to the optical adhesive that is used to

glue the Au onto the glass substrate. The molecular SAM serves as the tunnelling barrier through which electrons tunnel and generates the tunnelling current. The tunnelling barrier height is determined by the electronic energy levels of the SAM molecule while the tunnelling barrier width is determined by the length of the SAM. Because SAM is used, the tunnelling gap is always exactly one molecule thick.

The tunnelling barriers created using SAM can form either symmetrical or asymmetrical tunnelling barriers. These tunnelling barriers generate the corresponding symmetric and asymmetric current versus voltage response curves. One such SAM with a symmetric tunnelling barrier is that of $S(CH_2)_{n-1}CH_3$. To facilitate discussion, a simplified form of SC_n will be used instead. n refers to the carbon number and can be assigned a value of 10, 12, 16 and 18. It has large highest occupied molecular orbital (HOMO) – lowest unoccupied molecular orbital (LUMO) gaps of 8-9 eV. Considering EGaIn and Au electrodes, their Fermi levels fall approximately in the middle of the HOMO-LUMO gap of the SAM. Neither HOMO nor LUMO level of the SAM can participate in charge transport in the bias window of ±1.8 eV. Direct tunnelling (DT) dominates the charge transport for both bias directions as seen in the energy level diagram in Fig. 6.1.

For the SAM with an asymmetric tunnelling barrier such as (4-((4-(ferrocenyl)phenyl)ethynyl)phenyl)methanethiol (S-OPE-Fc), it has a HOMO level centered at -5 eV at the ferrocenyl unit (Fc) just below the Fermi levels of the electrodes. With positive bias, the HOMO level falls below the Fermi levels of both EGaIn and Au electrodes and cannot participate in charge transport. At negative bias, the HOMO energy level of Fc falls between the

Fermi levels of the electrodes and participates in charge transport via sequential tunnelling (ST). This means that electrons first tunnel from HOMO energy level to Au and then tunnel from EGaIn to HOMO level as shown in the energy level diagram in Fig. 6.2. LUMO is close in energy to the vacuum level and is not shown. The arrows correspond to the direction of the tunnelling electrons.

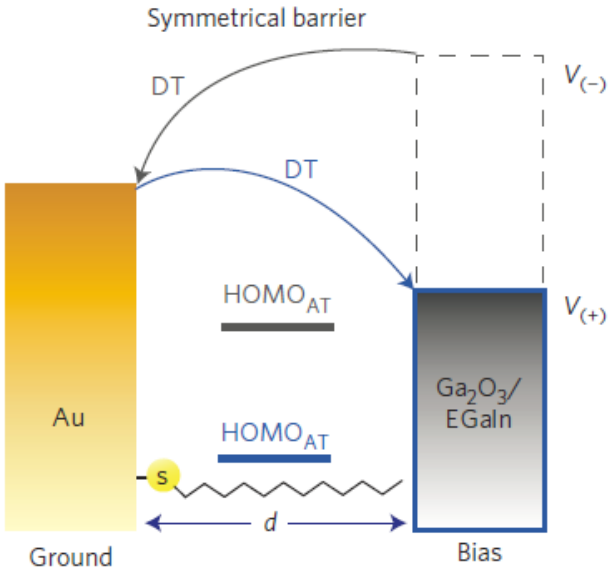

Figure 6.1: Energy level diagram with symmetric tunnelling barrier SAM [6.3].

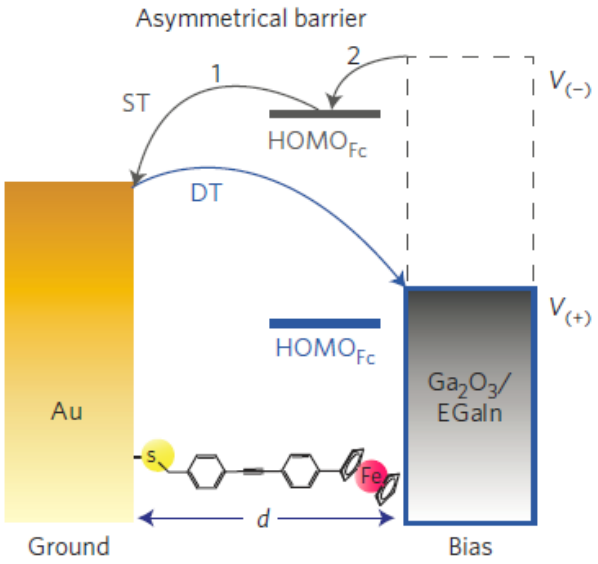

Figure 6.2: Energy level diagram with asymmetric tunnelling barrier SAM [6.3].

Since the mechanism of charge transport is believed to be similar [6.20-6.22] to that of SAMs with symmetric tunnelling barriers, these SAMs of SC_n were used for experimental studies. SAMs participates in charge transport and forms good molecular diodes as shown in Fig. 6.3.

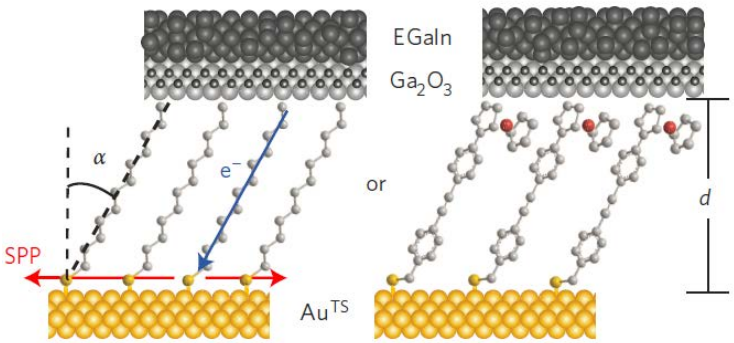

Figure 6.3: Tunnel junctions of SAM of SC_n (left) and SAM of S-OPE-Fc (right) [6.3].

The tunnelling direction along the SAM backbone is indicated by the blue arrow. A is the tilt angle of the SAM while d is the tunnelling barrier width.

6.3. Experimental setup

Similar to the setup described in Sec. 5.2, the optical properties of the SAM based tunnel junctions can be characterised by using an inverted optical microscope equipped with a spectrometer and an EMCCD. The optical characteristics were measured at the back side of these junctions through the semi-transparent Au anode with a 100x oil objective with numerical aperture of 1.49 when the junctions were biased. A 2 min integration time is used to record the plasmon emission spectra for both real (image) plane and back focal plane. The optical paths for the real plane and back focal plane images are indicated by the red and blue dashed lines respectively. When real plane images are recorded, lenses L_1 and L_2 were used. When back focal plane images were recorded, an extra lens L_3 is used together with L_1 and L_2. This can be shown in Fig. 6.4. The Au layers of 50 nm thickness were sufficiently thin to detect both localised SPP emission and SPP leakage radiation. The segment where the EGaIn is in contact with the SAMs can be classified as the protruded tip segment while the EGaIn-PDMS-SAM region can be classified as the MIM waveguiding segment. Instead of PDMS, an air gap can also be introduced. The protruded tip segment has a diameter of about 50 μm while the geometrical contact of the protruded tip segment is around 1000 μm^2. This constitutes a practical pMIM structure with a protruded tip segment (EGaIn-SAM-Au-OA) and a MIM waveguiding segment (EGaIn-PDMS-SAM-Au-OA or EGaIn-Air-SAM-Au-OA).

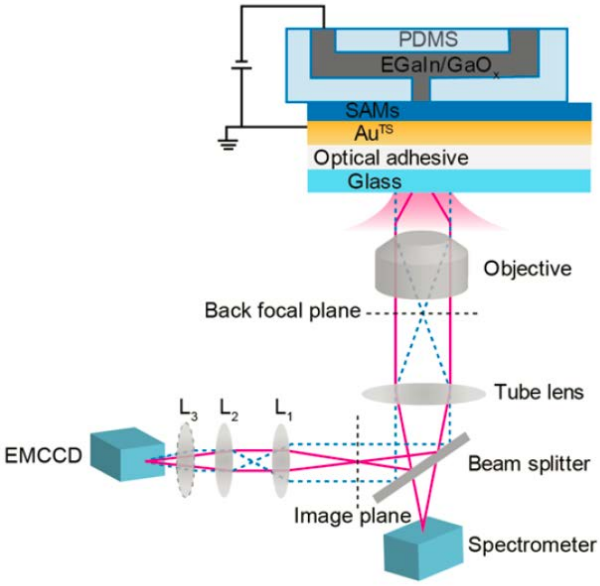

Figure 6.4: Schematic of optical characterisation setup [6.3].

6.4. Detection of excited plasmon polaritons using real and back focal plane images

Real plane images were extracted with an SC_{12} SAM biased at -1.8 V. The negative bias is on the EGaIn and the Au electrode is grounded. The real plane images for Au film thicknesses of 50 nm and 15 nm were as shown in Fig. 6.5 (a) and (b). These images were then overlaid on top of an optical image taken from the microscope as shown in Fig. 6.5(c) and 6.5(d) respectively.

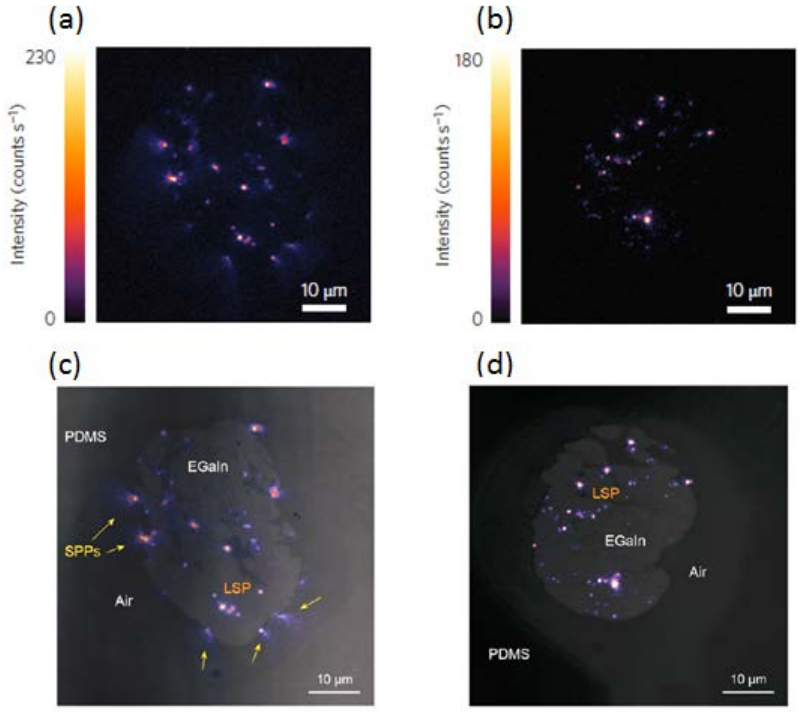

Figure 6.5: Images of plasmon polaritons excited in pMIM structure in the real plane for (a) 50 nm Au and (b) 15 nm Au. Real plane and optical images overlay for (c) 50 nm Au and (d) 15 nm Au [6.3].

From the images shown in Fig. 6.5, two observations can be made. First, both localised (LSPs) and propagating SPPs were seen to be excited. The localised SPPs are mainly excited in the protruded tip segment while the

propagating SPPs were excited at the interface between the protruded tip segment and the MIM waveguiding segment along the EGaIn-PDMS-SAM or the EGaIn-Air-SAM interface. The plasmon emission in the protruded tip segment is spatially inhomogeneous because the effective electrical contact area is estimated to be 10^4 times smaller than the geometrical contact area [6.23, 6.24].

The presence of the two types of localised and propagating SPPs can be further confirmed with the back focal plane images for Au film thicknesses of 50 nm and 15 nm were as shown in Fig. 6.6 (a) and (b).

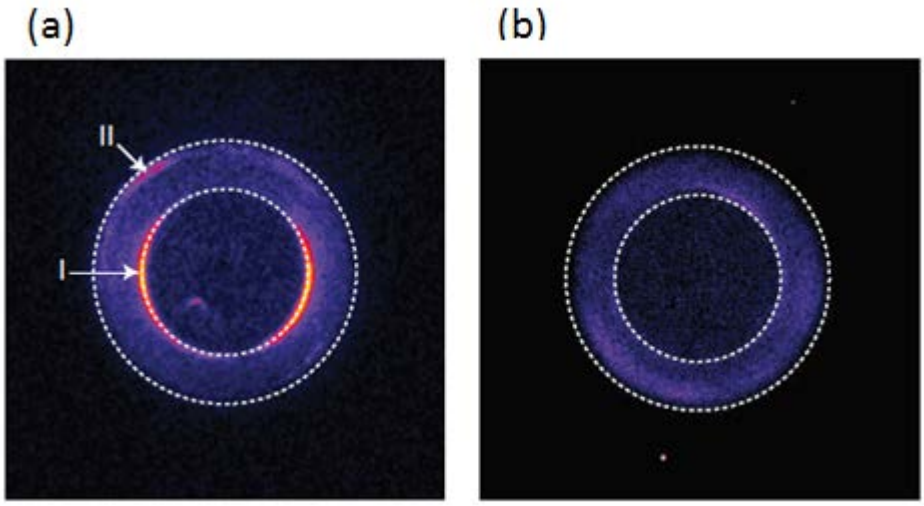

Figure 6.6: Images of plasmon polaritons excited in pMIM structure in the back focal plane for (a) 50 nm Au and (b) 15 nm Au [6.3].

The back focal plane image for the 50 nm Au pMIM structure shows two kinds of narrow arcs, confirming the excitation of the two types of SPP modes. SPP mode I can be attributed to propagating SPPs along SAM/Air interface while mode II is attributed to propagating SPPs along SAM/PDMS interface. For the thinner 15 nm Au pMIM structure, only localised SPPs are detected within the protruded tip segment as the propagating SPPs are damped

along the SAM-Air and SAM-PDMS interfaces. These modes are visible as discontinuous rings due to the non-uniform plasmon polariton excitation.

To understand the plasmon modes observed in both the real and back focal plane, the dispersion relations of SPPs were solved using the transfer matrix method. In the calculation, the refractive indices of air, PDMS and OA are taken as 1.0, 1.4 and 1.56 respectively. SAM is considered as a 2 nm air gap. The permittivity of Au and EGaIn were used to calculate the dispersion relations. The permittivity of EGaIn was measured and deduced by ellipsometry at wavelengths between 300 nm and 800nm. The Drude model was used to deduce the permittivity values above 800 nm similar to Appendix A. For Gallium, ω_p = 9.954 eV, γ_g = 1.796 eV. For Indium, ω_p = 17.321 eV, γ_g =0.038 eV [6.25]. The Drude model for EGaIn was estimated as a linear combination of the Drude models of Gallium (75.5%) and Indium (24.5%). The dispersion relation of SPPs in the three regions of the pMIM is shown in Fig. 6.7.

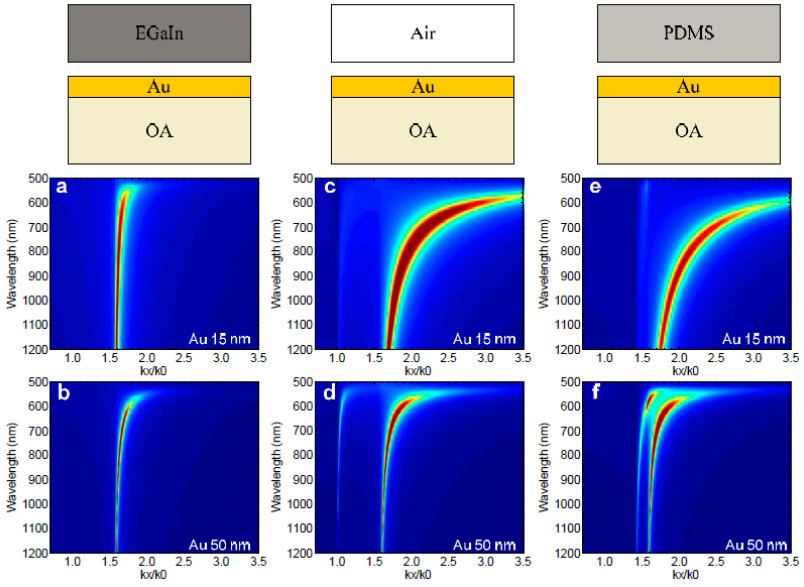

Figure 6.7: Dispersion relation of SPPs in the pMIM structure for 15 nm and 50 nm Au thickness in regions (a-b) EGaIn-SAM-Au-OA, (c-d) Air-SAM-Au-OA and (e-f) PDMS-SAM-Au-OA [6.3].

For all three regions, the SPP modes around mode index (k_x/k_o) ≈1.60 are present for both thicknesses except that the SPP mode is more confined with the thicker gold film. This mode corresponds to the SPP at the Au/OA interface. Because the numerical aperture of the oil objective is 1.49, this SPP mode cannot be detected through leakage radiation. In the protruded tip segment (EGaIn-SAM-Au-OA region), only localized surface plasmons are possible to be observed. SPP modes in the Air-SAM-Au-OA and PDMS-SAM-Au-OA regions of the MIM waveguiding segment depend on the thickness of the Au electrode. For the 50 nm gold film, besides the SPP mode at the Au-OA interface with mode index of 1.60, there are also SPP modes at the Au/SAM interface with mode index of 1.015 (λ = 850 nm) in Air-SAM-Au-OA region and at the Au/SAM interface with mode index of 1.465 (λ = 850 nm) in PDMS-SAM-Au-OA region. On the contrary, the propagating SPP modes are largely damped at similar interfaces for the 15 nm Au film. This phenomenon exists due to the collected spectra covering a larger area of the tip than the MIM waveguiding segment. In the previous numerical studies on pMIM structure in Ch.3, the waveguiding segment is assumed to be much larger than the protruded tip segment. These calculations confirm the experimental observations of the excitation of the two types of SPP modes.

6.5. Detection of excited plasmon polaritons using leakage radiation

Applying leakage radiation studies as a means to detect SPPs, the cross-sectional area at the site of the tunnelling current generation in the protruded tip segment can be modelled by an MIM structure that makes use of self-assembled monolayers (SAM) as a molecular tunnelling junction is proposed as shown in Fig. 6.8.

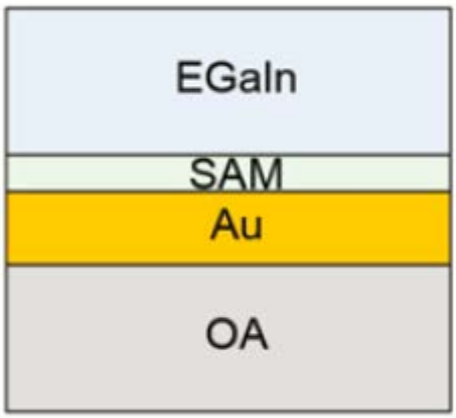

Figure 6.8: MIM structure to model cross-sectional area at the site of the tunnelling current generation in the protruded tip segment [6.3].

To show that leakage radiation can be used to detect excited propagating SPPs, there is a need to predict the leakage radiation spectra of excited propagating SPPs from FEM simulations, taking into account both elastic and inelastic electron tunnelling mechanisms which make up the excited tunnelling current. The obtained leakage radiation spectra are then compared with that observed experimentally.

In elastic tunnelling process, elastic tunnelling electrons excite plasmons, change the dielectric environment and determine the plasmon resonance. This elastic tunnelling profile as a function of photon energy can be obtained in two ways. The first way is to use a Gaussian shape profile as an

approximation once the plasmon resonance is known. The second way is to extract the excited eigenfield profile at the interface where plasmon polaritons are excited.

In inelastic tunnelling process, tunnelling electrons lose energy and couple to plasmon states. The lost energy is converted into emitted light. The metric used here is the probability of energy loss, P_{loss} where

$$P_{loss} = 1 - \frac{\hbar\omega}{eV} \qquad (6.1)$$

where V is the applied bias and ħω is the photon energy. Physically this means that when a bias voltage is applied on the tunnel junction, electrons that inelastically tunnel through the barrier lose energy which can range from zero to the applied bias voltage and couple to the plasmonic modes of the tunnel junction. This lost energy decays as photon emission.

The theoretical leakage radiation spectra can be predicted by considering a coupling of both elastic and inelastic tunnelling mechanisms. Using Fig. 6.8 as a benchmark of study, FEM numerical simulations were performed to obtain the field profile as a result of elastic tunnelling. For this MIM structure on a glass substrate, the EGaIn cathode, SAM, Au anode and OA/glass substrate are assigned a thickness of 1 µm, 0.5 µm, 50 nm, 2 nm and 1 µm respectively. In the numerical model, PML boundary conditions are adopted. A localised tunnelling current J is modelled using a 1 nm radius cylinder within the 2 nm thick SAM layer. Au thickness of 50 nm was adopted. The excited plasmonic eigenfields were calculated by solving the Maxwell's equations with the localised tunnelling current $\bar{J}$ as the excitation source. The eigenfields of |H| at Au/OA interface is extracted a distance away from the source, around 750 nm. It shows the plasmon mode with a full width

half maximum (FWHM) of around 0.5 eV. The shape of this broadband response is independent of the distance from the excitation source. This serves as equivalent spectra from the elastic tunnelling mechanism as shown in Fig. 6.9. To calculate the spectra from the inelastic tunnelling mechanism, Eqn. 6.1 is made use of, with voltage bias ranging from 1.5 to 2.2 eV to derive the plot shown in Fig. 6.9 as well.

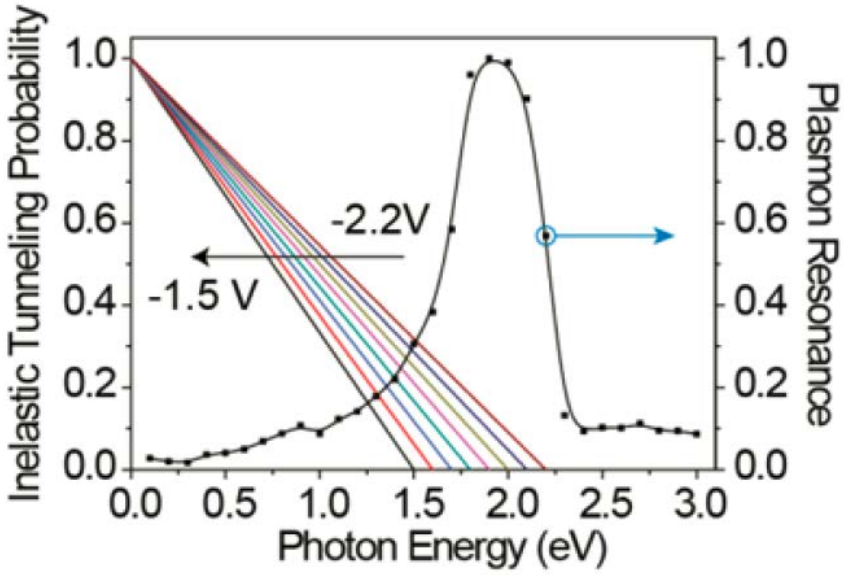

Figure 6.9: Inelastic tunnelling probability at different biases and the plasmonic resonance of the structure in Fig. 6.8 [6.3].

.

From the two spectra obtained from both elastic and inelastic tunnelling mechanism, the theoretical leakage radiation spectra can be calculated by multiplying the spectra together. This allows the spectrum shown in Fig. 6.10 to be derived.

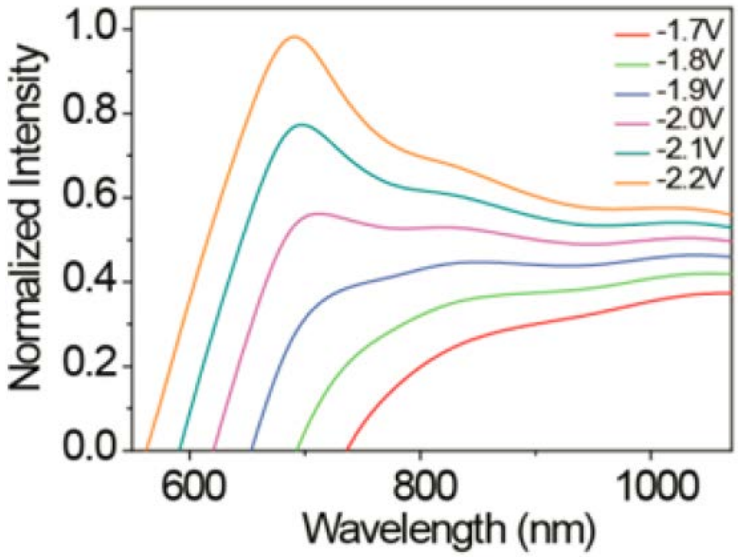

Figure 6.10: Theoretical leakage radiation spectra by considering both inelastic tunnelling probability and plasmonic resonance [6.3].

To see if the theoretical leakage radiation spectrum matches the values calculated experimentally, the response of the spectrum collection system which is shown in Fig. 6.11 needs to be taken into account. This spectrum collection system includes the transmission of the whole microscope system, the reflection of the mirror system in the spectrometer and the CCD quantum efficiency of the spectrometer as described in Sec. 6.3.

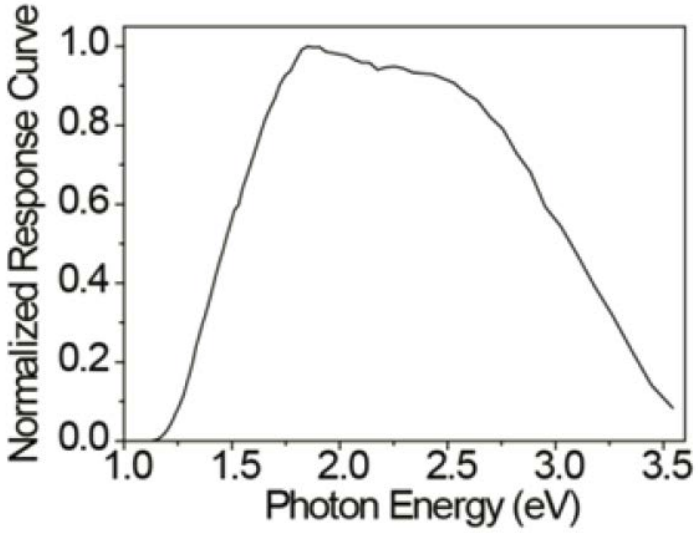

Figure 6.11: Spectral response of spectral collection system [6.3].

By taking into account the response of the spectrum collection system which is shown in Fig. 6.11, the resultant spectrum can be derived as shown in Fig. 6.12. Comparing it with the leakage radiation spectra obtained experimentally as shown in Fig. 6.13, a very good correlation can be observed between the calculated spectra and the experimental spectra. This means that both elastic and inelastic tunnelling processes contribute to the excitation of plasmon polaritons.

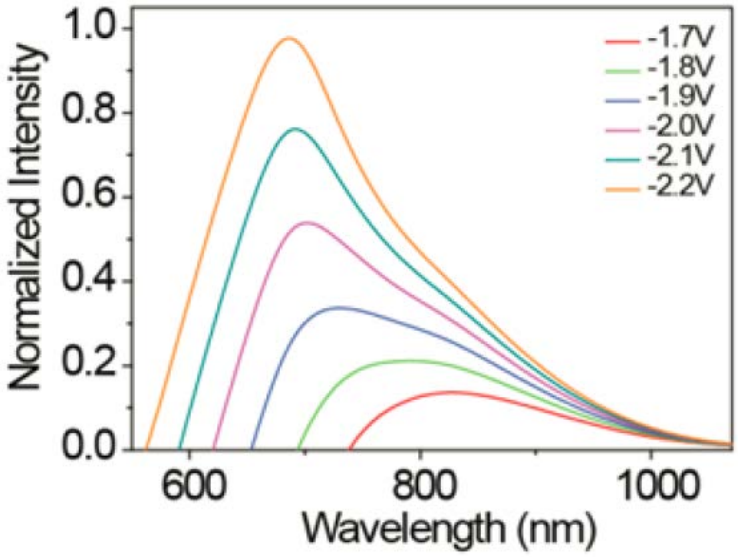

Figure 6.12: Calculated spectra by considering the inelastic tunnelling probability, the plasmonic resonance and the spectra response of the spectrum collection system [6.3].

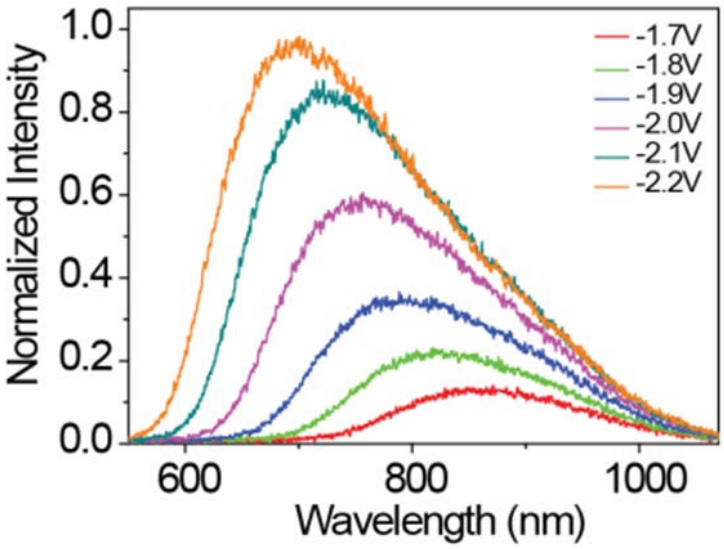

Figure 6.13: Experimental spectra at different biases [6.3].

To further show that leakage radiation spectra can be used to provide insights behind detected excited plasmon polaritons, the magnitude of the total electric field is plotted at SPP resonance energy at 2.0 eV and energies off SPP resonance at 1.2 eV and 2.8 eV as shown in Fig. 6.14. The energies off SPP resonance are energies where direct emission from tunnelling current is expected to dominate. These simulation results are independent of applied bias and account for the resonant energy states for plasmon coupling and hence light emission.

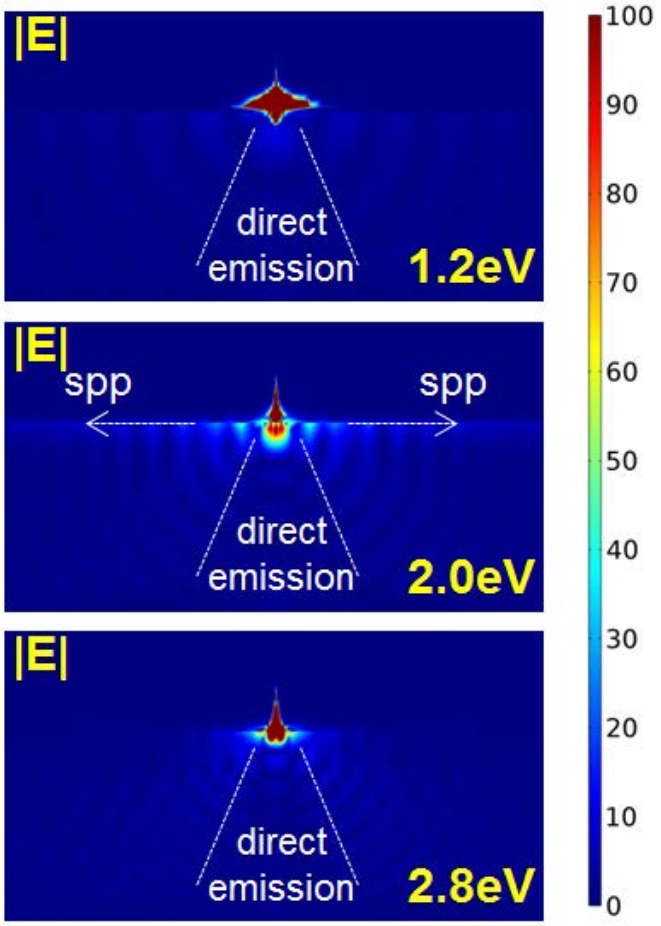

Figure 6.14: Magnitude of total electric field at on/off SPP resonance.

6.6: Summary

Working with experimental collaborators, a practical pMIM structure with a protruded tip segment (EGaIn-SAM-Au-OA) and a MIM waveguiding segment (EGaIn-PDMS-SAM-Au-OA or EGaIn-Air-SAM-Au-OA) with 15 nm and 50 nm Au anode were fabricated and excited SPPs were measured. By taking into considerations both elastic and inelastic electron tunnelling mechanism which make up the excited tunnelling current, the observed leakage radiation spectra can also be attributed to the excited propagating SPPs in the structure. The model used for FEM simulations forms an important basis to implement design principles for the pMIM on-chip plasmon source studied in this thesis.

While the pMIM structure can be made compact with negligible leakage radiation, the highly efficient plasmon polaritons are excited with symmetric directivity. Such symmetric directivity can be further manipulated to obtain asymmetric directivity in order to mimic an ideal on-chip source which is highly directional.

6.7. References

[6.1] B. Xu and N.J. Teo, “Measurement of single molecule resistance by repeated formation of molecular junctions”, Science, 301(5637), 1221 (2003)

[6.2] K. Liu, Ph. Avouris, J. Bucchignano, R. Martel, S. Sun and J. Michl, “Simple fabrication scheme for sub-10nm electrode gaps using electron beam lithography”, Applied Physics Letters, 80(5), 865-867 (2002)

[6.3] W. Du, T. Wang, H.S. Chu, L. Wu, R. Liu, S. Sun, W.K. Phua, L. Wang, N. Tomczak and C.A. Nijhuis, “On-chip molecular electronic plasmon sources based on self-assembled monolayer tunnel junctions”, Nature Photonics, 10(4), 274-280 (2016)

[6.4] S.F. Tan, L. Wu, J.K. Yang, P. Bai, M. Bosman and C.A. Nijhuis, “Quantum plasmon resonances controlled by molecular tunnel junctions”, Science, 343(6178), 1496–1499 (2014)

[6.5] H. Raether, “Surface plasmons on smooth and rough surfaces and on gratings”, Springer, 1986

[6.6] E. Kretschmann and H. Raether, “Radiative decay of nonradiative surface plasmons excited by light”, Z.Naturforsch, 23(12), 2135-2136 (1968)

[6.7] S.A. Maier, *Plasmonics: Fundamentals and Applications* (Springer, 2007)

[6.8] L. Novotny and B. Hecht, “Principles of nano-optics”, Cambridge University Press, 2nd edition (2012)

[6.9] P. Berini and I. De Leon, “Surface plasmon polariton amplifiers and lasers”, Nature Photonics, 6, 6-24 (2012)

[6.10] E.T. Arakawa, M.W. Williams, R.N. Hamm and R.H. Ritchie, “Effect of damping on surface plasmon dispersion”, Physical Review Letters, 31(18), 1127-1129 (1973)

[6.11] I. De Leon, Z. Shi, A.C. Lapis and R.W. Boyd, “Measurement of the complex nonlinear optical response of a surface plasmon polariton”, Optics Express, 39(8), 2274-2227 (2014)

[6.12] M. Mayy, G. Zhu, A.D. Webb, H. Ferguson, T. Norris, V.A. Podolskly and M.A. Noginov, “Toward parametric amplification in plasmonic systems: Second harmonic generation enhanced by surface plasmon polaritons”, Optics Express, 22(7), 7773-7782 (2014)

[6.13] P. Ferguson, R.F. Wallis, M. Belakhovsky, J.P. Jadot and J. Tomkinson, “Surface plasma waves in silver and gold”, Surface Science, 76(2), 483-498 (1978)

[6.14] J.J. Burke, G.I. Stegeman and T. Tamir, “Surface polariton like waves guided by thin lossy metal films”, Physical Review B, 33(8), 5186-5201 (1986)

[6.15] L. Wendler and R. Haupt, “An improved virtual mode theory of ATR experiments of surface polaritons”, Physica Status Solidi B, 143, 131-147 (1987)

[6.16] R. Wakamatsu and K. Saito, “Interpretation of attenuated total reflection dips observed in surface plasmon resonance”, Journal of the Optical Society of America B, 24(9), 2307-2313 (2007)

[6.17] D. Brissinger, L. Salamon and F.D. Fornel, “Unguided plasmon mode resonance in optically excited thin film: exact modal description of Kretschmann-Reather experiment”, Journal of the Optical Society of America B, 30(2), 333-337 (2013)

[6.18] J.J. Foley, H. Harutyunyan, D. Rosenmann, R. Divan, G.P. Wiederrecht and S.K. Gray, “When are surface plasmon polaritons excited in the Kretschmann-Raether configuration”, Scientific Reports, 5, 9929 (2015)

[6.19] P. Bharadwaj, A. Bouhelier and L. Novotny, “Electrical excitation of surface plasmons”, Physical Review Letters, 106(22), 226802 (2011)

[6.20] C.A. Nijhuis, W.F. Reus and G.M. Whitesides, “Molecular rectification in metal–SAM–metal oxide–metal junctions”, Journal of the American Chemical Society, 131(49), 17814–17827 (2009)

[6.21] N. Nerngchanmnong, L. Yuan, D.C. Qi, J. Li, D. Thompson and C.A. Nijhuis, “The role of van der Waals forces in the performance of molecular diodes”, Nature Nanotechnology, 8(2), 113–118 (2013)

[6.22] H. Jeong, D. Kim, G. Wang, S. Park, H. Lee, K. Cho, W.T. Hwang, M.H. Yoon, Y.H. Jang, H. Song and D. Xiang, “Redox-induced asymmetric electrical characteristics of ferrocene–alkanethiolate molecular devices on rigid and flexible substrates”, Advanced Functional Materials, 24(17), 2472–2480 (2014)

[6.23] F.C. Simeone, H.J. Yoon, M.M. Thuo, J.R. Barber, B. Smith and G.M. Whitesides, “Defining the value of injection current and effective electrical contact area for EGaIn-based molecular tunneling junctions”,

Journal of the American Chemical Society, 135(48), 18131–18144 (2013)

[6.24] C.S.S. Sangeeth, A. Wan, and C.A. Nijhuis, “Equivalent circuits of a self-assembled monolayer-based tunnel junction determined by impedance Spectroscopy”, Journal of the American Chemical Society, 136(31), 11134–11144 (2014)

[6.25] R. Berndt, J.K. Gimzewski and P. Johansson, “Inelastic tunneling excitation of tip-induced plasmon modes on noble-metal surfaces”, Physical Review Letters, 67(27), 3796 (1991)

[6.26] J.A. Hutchison, H. Uji-i, A. Deres, T. Vosch, S. Rocha, S. Müller, A.A. Bastian, J. Enderlein, H. Nourouzi, C. Li and A. Herrmann, “A surface-bound molecule that undergoes optically biased Brownian rotation”, Nature Nanotechnology, 9(2), 131–136 (2014)

Chapter 7. Double protruded metal-insulator-metal (p^2MIM) structure for asymmetric directivity of excited plasmon polaritons

7.1. Introduction

For an on-chip source to excite plasmon polaritons with high directionality, there is first a need for the symmetric directivity to be further manipulated to obtain asymmetric [7.1-7.3] directivity. This is particularly useful in pMIM structures where all the emitted power should nominally be directed in the desired direction. Directivity can be achieved by manipulating the substrate layer to introduce regular or irregular corrugations such as gratings [7.4, 7.5], similar to those mentioned in Ch. 2, which serve to obstruct and redirect the power flow. Much of these techniques require complex fabrication processes and are difficult to implement. There is a need for potential solutions that can circumvent such complex fabrication processes. The reduction of complex fabrication processes introduces fewer uncertainties and deviations in the design parameters of the pMIM structure. One potential solution is to make use of surface eigenmodes excited on nanostructures placed below the tip of pMIM structures. This surface eigenmode profile is generated by the excited tunnelling current and shows a correlation with the circular dichroism (CD) signature which include left handed circularly polarised (LCP) and right handed circularly polarised (RCP) components. Hence the CD signature can be used to predict the surface eigenmode profile

which can in turn be used to predict the directivity patterns as shown in section 7.3. The localised SPPs on the surface of the nanostructures can be used to tune the directivity of propagating SPPs. The surface eigenmode profile of the localised SPPs can be controlled with a rotated nanostructure or by engineering smart nanostructures.

The study of surface eigenmode profile on nanostructures placed in pMIM structures pose a huge challenge experimentally since there is no way to extract the surface eigenmode profile once the nanostructure is enclosed within the pMIM structure. Leakage radiation measurements require finite substrate thicknesses in order to extract a detectable signal and as a result, much focus will be on the resonant peaks of excited propagating SPPs in the pMIM's waveguiding segment, not the localised SPPs on the surface of the nanostructure as discussed in Ch. 5. The surface eigenmode profile on the nanostructure cannot be extracted from the leakage radiation spectra either.

The tunnelling current excitation of localised SPPs on nanostructures can be studied from numerical simulations. However the use of numerical simulations is limited to only simple nanostructures due to the large computational cost involved. A theoretical approach is proposed to establish a correlation between the excited localised SPP eigenmodes and the circular dichroism signature on the nanostructures. As a proof of concept, this correlation is used as a basis to predict and validate the surface eigenmodes of basic and well-studied nanostructures such as the gammadion from section 7.4 onwards. It allows the prediction of excited localised SPP eigenmodes without having to undertake huge numerical computations. Such studies can further be extended to design practical nanostructures or coupled basic nanostructures to

induce a desired surface eigenmode profile in order to generate directivity. The well-established gammadion chiral nanostructure is chosen to validate the accuracy of the model used in the rest of the thesis. This chapter serves as an important starting point for future work in the excitation of plasmon polaritons with high directivity. More work can be done to implement this concept, for instance by engineering more easily-fabricated nanostructures or designing basic coupled nanostructures to induce a desired surface eigenmode profile in order to generate highly directional plasmon polaritons.

7.2. Proposed p^{2}MIM design and implementation

A method of achieving asymmetric directivity of excited SPPs is to harness the field profile or hot spots of surface eigenmodes on a metal nanostructure placed below the protruded tip, forming a double protruded metal-insulator-metal (p^{2}MIM) structure. This can be seen as shown in Fig. 7.1.

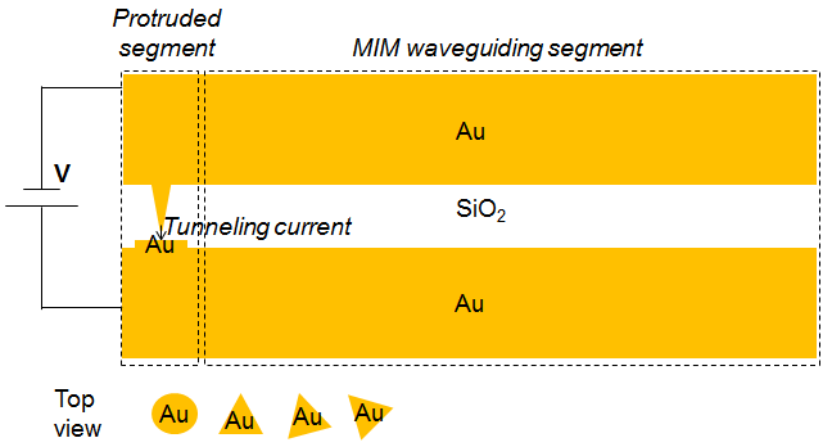

Figure 7.1: p^{2}MIM as a method to redirect excited SPPs. Circular and triangular basic nanostructures are used as an example.

Depending on the nanostructure design adopted, different surface eigenmode profiles can be achieved due to the excited localised SPPs on the surface of the nanostructure. With the surface eigenmode profile, the excited localised SPPs can be used to control the direction of propagating SPPs in the waveguiding segment of the p^{2}MIM. Propagating SPPs can then spread outwards in a particular direction with stronger output power.

7.3. Correlation between surface eigenmodes excited by tunnelling current with circular dichroism (CD) signature of nanostructures

The p^2MIM structure provides a very good avenue for directionality control since it makes use of a tunnelling current which excites localised SPPs, providing directionality predictions equivalent to the CD signature of excited localised SPPs from optical excitations [7.6-7.8]. In numerical simulations, the magnitude of the DC tunnelling current that is dependent on applied bias can be used as an input source. For numerical analysis, the current source is assumed to take into account current flow in both directions between the top and bottom electrodes. When the tunnelling current is incident from the top and interacts with the nanostructure, the current produces a magnetic field (H) in the clockwise direction, in accordance to the right hand rule. This is equivalent to having a right handed circularly polarised (RCP) light interacting with the nanostructure. In a similar fashion, if the current is incident from the bottom of the nanostructure, the H field is generated in the anticlockwise direction. This is equivalent to having a left handed circularly polarised (LCP) light interacting with the nanostructure. From the direction of the H field, the direction of the induced electric (E) field can be identified. This can be seen in Fig 7.2.

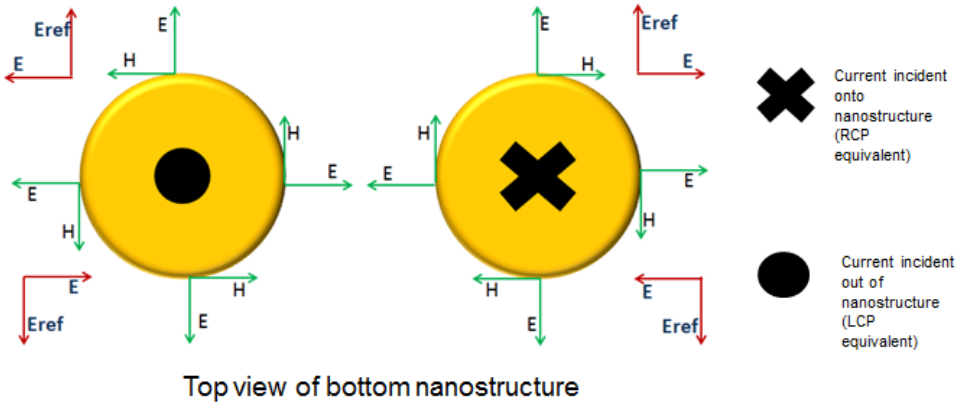

Figure 7.2: Current excitation equivalent to circularly polarised light.

Numerical current simulations only take into account current density and hence considers excited tunnelling current passing into and out of plane of the nanostructure. Since this current should generate surface eigenmodes equivalent to circularly polarised light, the surface eigenmodes which are observed actually correspond to the CD signature for similar nanostructures. The CD signature of surface eigenmodes on basic nanostructures can be derived from the plasmon hybridisation theory.

7.4. Prediction of excited surface eigenmode profile for basic nanostructures using plasmon hybridisation theory

Using light excitation as the governing mechanism, we derive the CD signature of excited eigenmodes in these basic nanostructures from the plasmon hybridisation theory. Plasmon hybridisation is a method which provides a simple and intuitive explanation behind how plasmons [7.9] supported by elementary metal nanoparticles or nanostructures interact with one another, forming different energy states and hence inducing different behaviour at the plasmon resonance frequencies [7.10].

Plasmon interaction can be supported by elementary nanostructures, namely nanosphere, nanorice and nanostar [7.10-7.12]. The theoretical formalism [7.13, 7.14] was applied to the interaction between nanosphere and surface [7.15]. There were also studies on new plasmon modes creation when two nanoparticles are placed close together to form a nanoparticle pair [7.16, 7.17]. Hybridisation studies allow the field distributions to be shown, allowing for the identification of different modes for a particular nanoparticle or nanostructure. Fundamental physics of local charge distribution can be applied to provide an intuitive picture on how hybridised plasmon modes arise.

Considering an RCP light incident into a piece of paper (xy plane), there is a rotation in the polarisation of light from the E_y direction to the E_x direction as shown in Figure 7.3. Similarly for LCP light, the rotation of the polarised light is from the E_y direction to the negative E_x direction. For both LCP and RCP light polarisation, the dominant polarisation is along the x and y directions. Hence, by considering the two dominant polarisation of light on

nanostructures, we are able to determine the types of plasmon modes that can be excited on nanostructures.

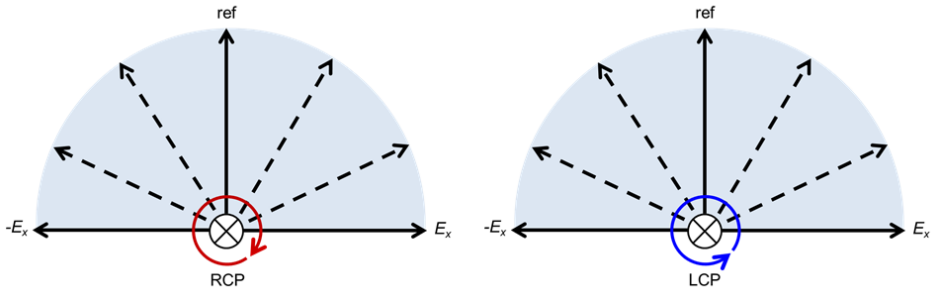

Figure 7.3: Rotation in light orientation for RCP and LCP, with light normally incident onto the xy-plane. Dotted lines indicate the field components in the xy-plane [7.18].

Basic planar nanostructures are nanostructures which act as building blocks from which all complex nanostructures can be built. Examples of basic planar nanostructures include that of circular, triangular, square and rectangular nanostructures. When basic planar nanostructures of subwavelength dimensions are considered, an electric dipole moment can be excited in the nanostructure with an incident light source of known polarisation. Different dipole moments will be induced depending on the polarisation of the excitation light source. Defining an electric dipole moment in the configuration shown in Fig. 7.4, the impact of induced dipole moments from $-E_x$, E_x, $-E_y$ and E_y polarisation can be considered.

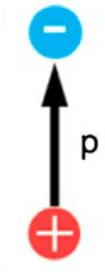

Figure 7.4: Electric dipole moment and its corresponding charge distribution [7.18].

Figures 7.5(a), 7.5(b), 7.5(c) and 7.5(d) each show a single planar rectangular nanostructure and its corresponding dipole moment induced with $-E_x$, E_x, $-E_y$ and E_y light polarisation respectively. Although there are four polarisation modes, only two hybridised modes are essentially excited because the structure is not chiral and does not possess a circular dichroism (CD) signature, meaning that its mirror image can be superimposed onto itself.

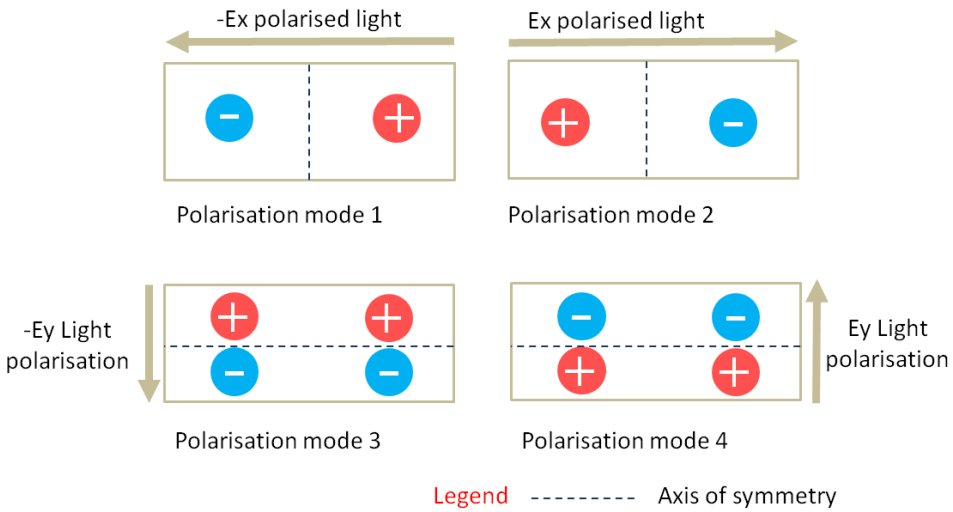

Figure 7.5: Polarisation modes on single rectangular nanostructure for incident light polarised in directions (a) $-E_x$, (b) E_x, (c) $-E_y$ and (d) E_y.

The above observation is seen to be similar for circular, square and triangular nanostructures as shown in Fig. 7.6, Fig. 7.7 and Fig. 7.8 respectively.

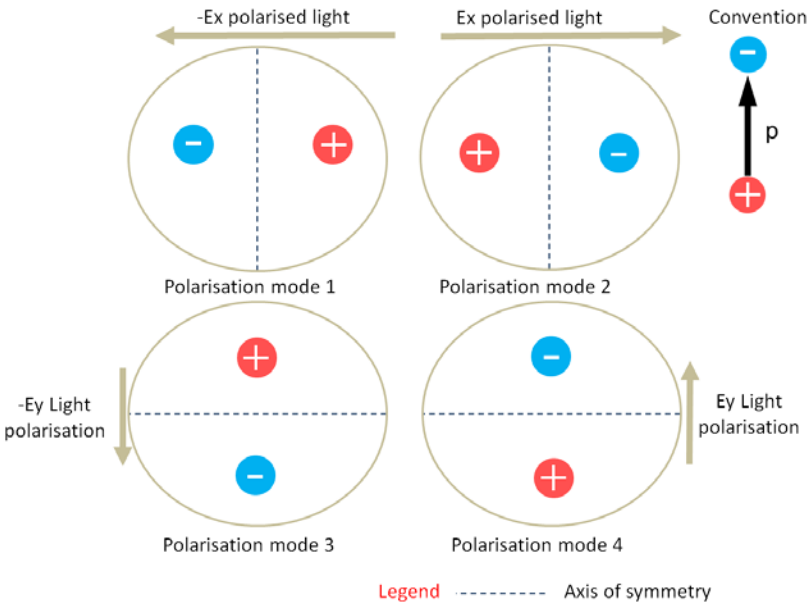

Figure 7.6: Polarisation modes on single circular nanostructure for incident light polarised in directions (a) –Ex, (b) Ex, (c) –Ey and (d) Ey.

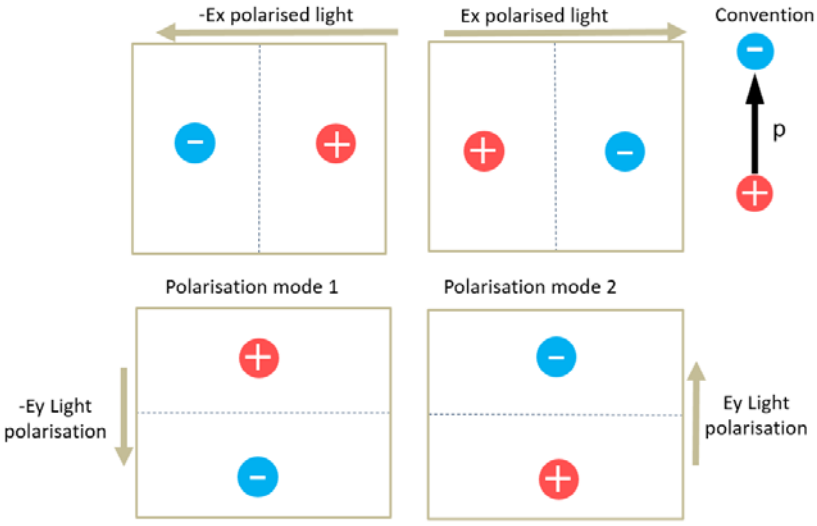

Figure 7.7: Polarisation modes on single square nanostructure for incident light polarised in directions (a) $-E_x$, (b) E_x, (c) $-E_y$ and (d) E_y.

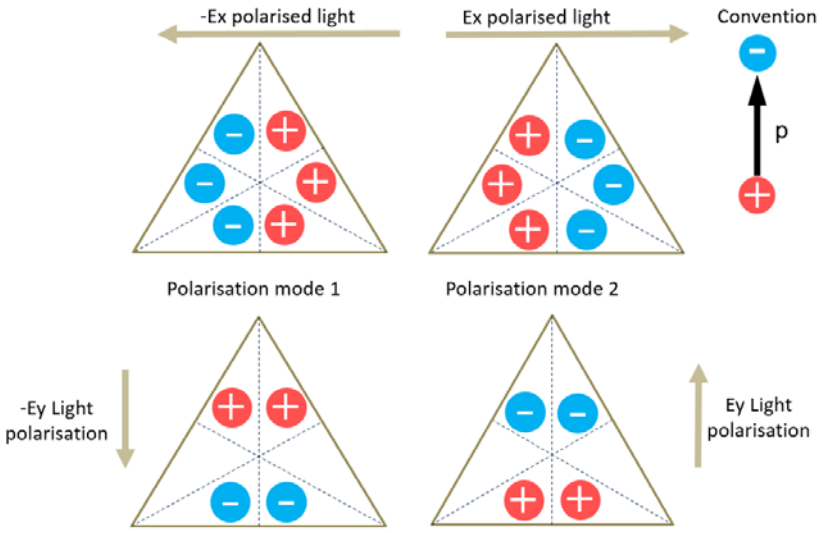

Figure 7.8: Polarisation modes on single triangular nanostructure for incident light polarised in directions (a) $-E_x$, (b) E_x, (c) $-E_y$ and (d) E_y.

Considering the superposition of the electric dipole field profiles from both LCP and RCP light, the CD signature of the circular, square, triangular and vertical rectangular nanostructures can be derived as shown in Fig. 7.9 to Fig. 7.12, respectively.

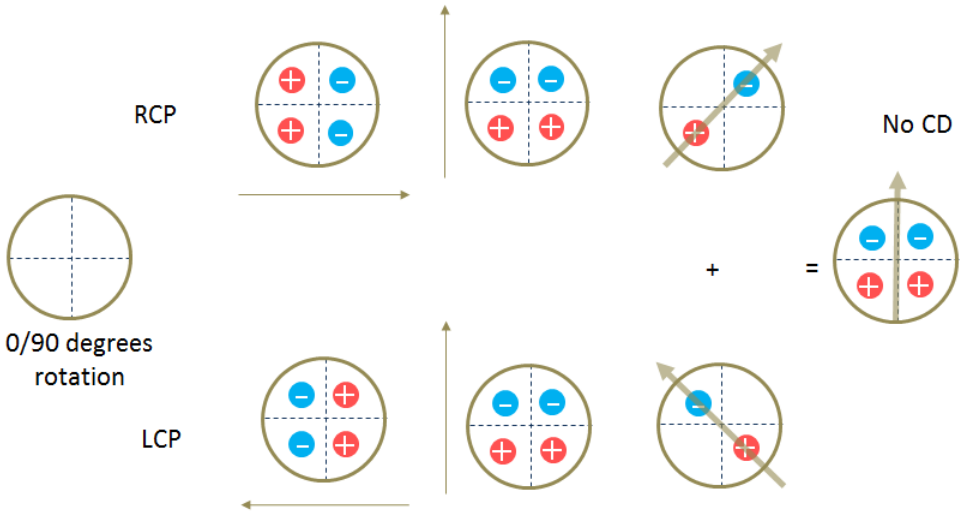

Figure 7.9: CD signature of circular nanostructure

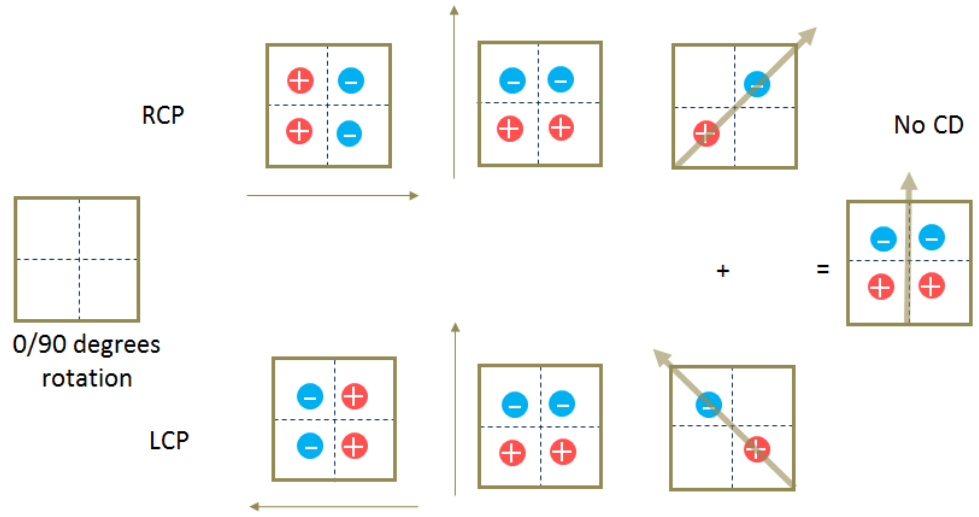

Figure 7.10: CD signature of square nanostructure

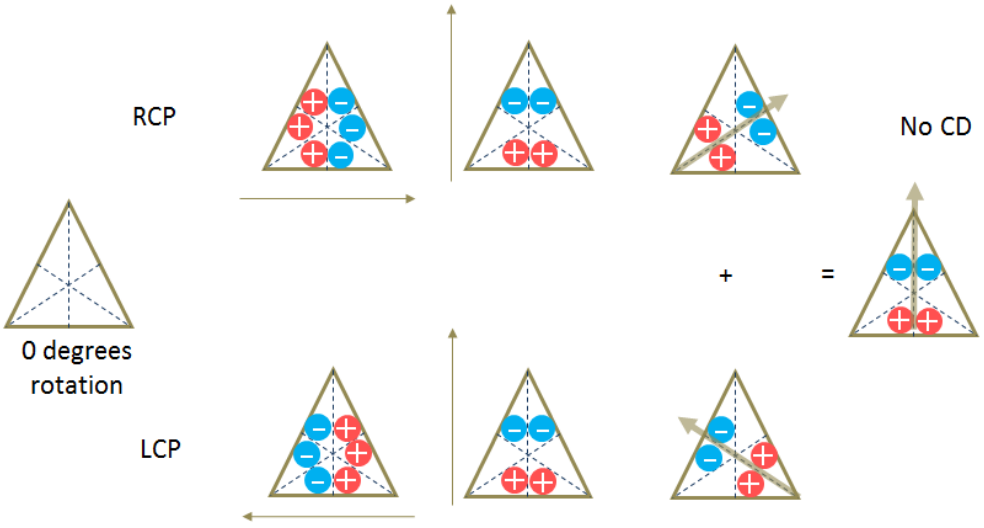

Figure 7.11: CD signature of triangular nanostructure

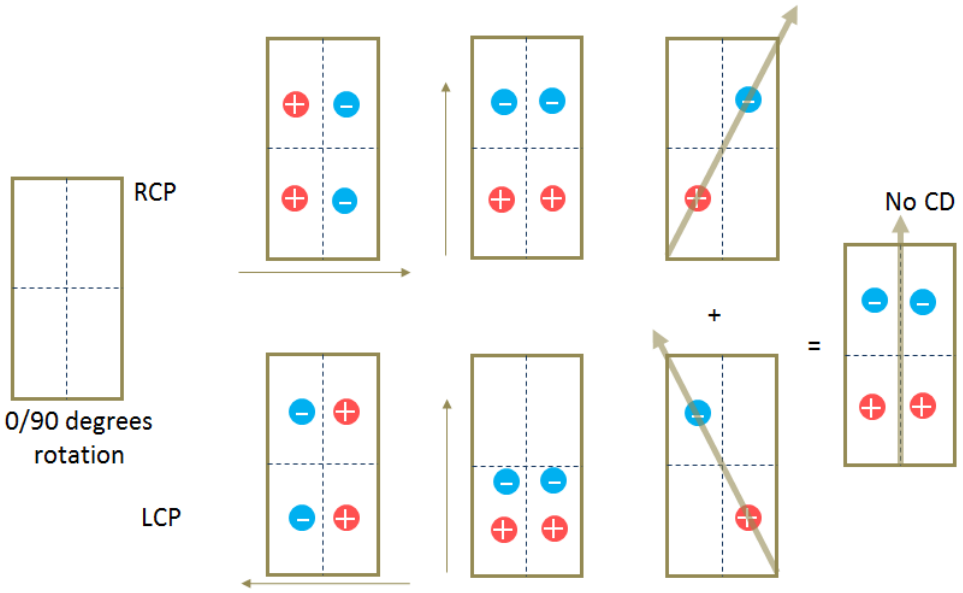

Figure 7.12: CD signature of vertical rectangular nanostructure

Since the four mentioned basic nanostructures do have a mirror image along the y axis that can be superimposed on their original images, it is expected that there will be no CD signature which is shown in accordance to the plasmon hybridisation theory applied in the proposed manner. According to the CD signature, all non-rotated basic nanostructures including the square, triangle, circle and rectangle should exhibit the same surface eigenmode profile and hence the same preference for SPP propagation. While there is no CD signature for these basic nanostructures, a CD signature can be induced via angular rotation, assuming that the incident light remains along the same plane, with the reference direction along the positive y direction. By inducing rotation in an anticlockwise manner from 0 degrees to 75 degrees, a CD signature can be induced for all basic nanostructures. An example for a triangular nanostructure is shown in Fig. 7.13.

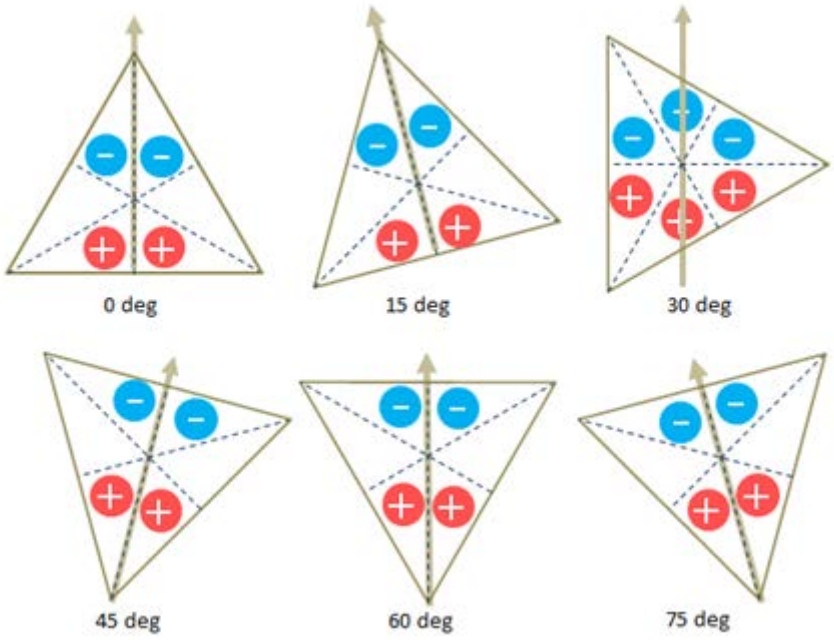

Figure 7.13: Theoretically predicted surface eigenmode profiles from tunnelling current excited rotated triangular nanostructures of varying degrees.

Further it has been found that the very means of rotation further induces a flip in CD signature from positive to negative or vice versa. At 15 and 75 degrees rotation, LCP character is dominant, resulting in a positive CD signature. At 45 degrees rotation, RCP character is dominant, resulting in a negative CD signature.

The equivalent E_z field distribution for an equivalent light excitation is obtained from simulation for the triangular nanostructure as shown in Fig. 7.14 which provides good agreement with that predicted from theory. The triangular nanostructure structure shown in Fig. 7.14 has a width of 200 nm and a periodicity of 800 nm. It is 100 nm thick and suspended in air. Gold is used for the triangular nanostructure. The permittivity value of gold is obtained from the optical handbook [7.19]. The triangular nanostructure was simulated using the finite-difference time-domain (FDTD) method with Lorentz-Drude model to account for the damping of the metal. Perfectly

matched layer were applied to both vertical and horizontal axes of the domain. The simulation grid size is set to 4 nm in all directions to obtain accurate transmission, scattering and reflection spectra. The triangular nanostructure was rotated and its E_z field distribution extracted for varying rotation angles. Since the circular nanostructure has a similar geometry regardless of its angle of rotation, it does not exhibit any CD signature even if it's rotated.

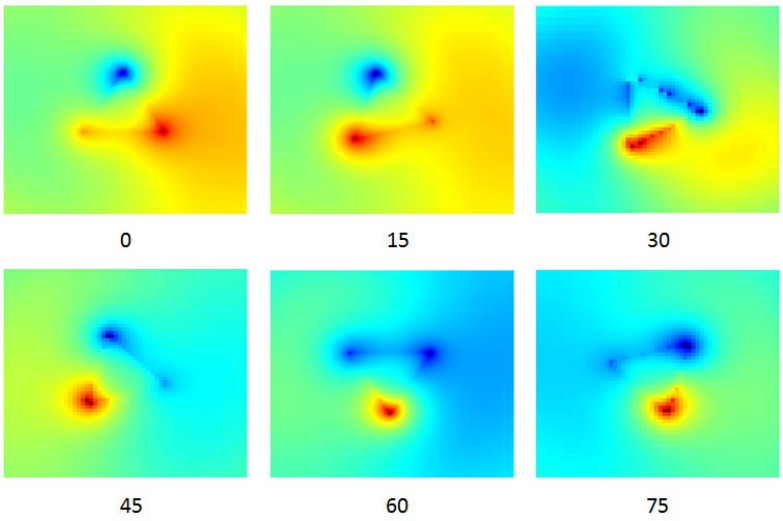

Figure 7.14: E_z field distribution for rotated triangular nanostructure varying from 0 to 90 degrees.

To validate the dominance of RCP or LCP in the CD signature, the CD spectra of the triangular nanostructure was extracted as observed from numerical simulations. The absorption spectra of the triangular nanostructure was obtained using left and right handed circular polarised light and the difference taken, giving the CD spectrum shown in Figure 7.15. CD is given as

$$CD = A_L - A_R \qquad (7.1)$$

where A_L/A_R refers to the absorption of LCP/RCP, respectively.

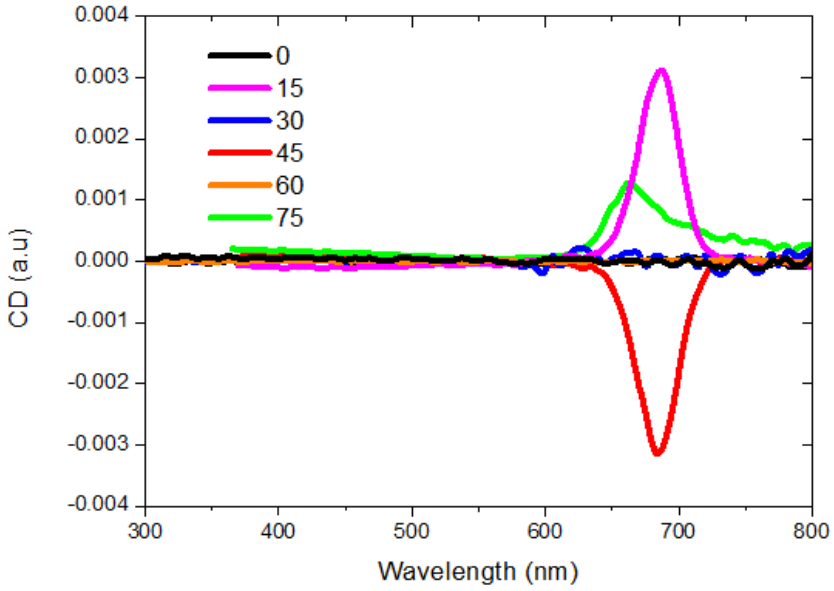

Figure 7.15: CD spectra of triangular nanostructure suspended in air.

The CD spectra obtained from numerical simulations correlates with the postulated CD signature seen in Fig. 7.13. An interesting phenomenon that can be observed from the plasmon hybridisation studies of rotated structures is that although the 30 degrees-rotated triangular nanostructure is expected to exhibit a CD signature based on intuition, this is not the case as in accordance to theory.

In order to obtain a distinct signature of surface eigenmodes for a tunnelling current excitation, there is a need to perform a rotation of these basic nanostructures. Using a triangular nanostructure that is rotated from 0 to 75 degrees as a test of concept for future design considerations, the results from numerical simulations are as shown in Fig. 7.16. The simulation setup mirrors that of pMIM structures discussed in Ch. 3.

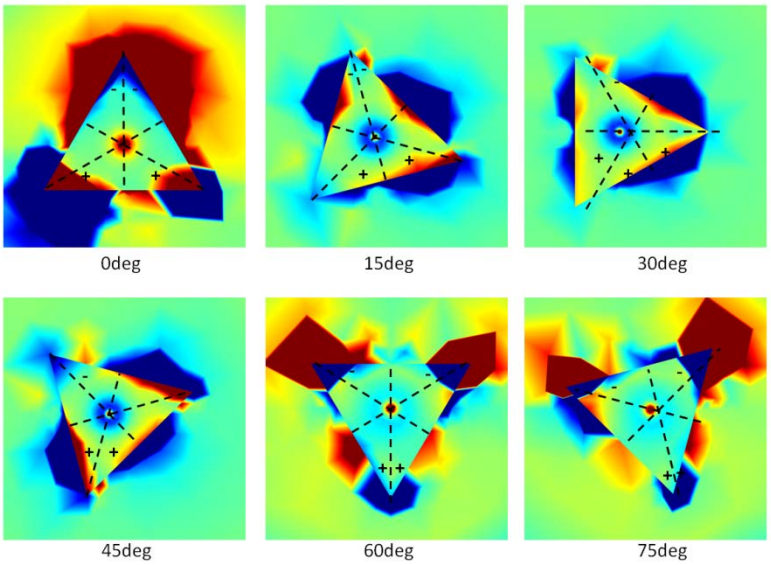

Figure 7.16: Numerically obtained surface eigenmode profiles of rotated triangular nanostructures from tunnelling current excitation.

7.5. Prediction of excited surface eigenmode profile for complex nanostructures using plasmon hybridisation theory

The plasmon hybridisation theory can be further extended to investigate the surface eigenmodes of complex nanostructures. Complex planar nanostructures can usually be easily decomposed into basic building blocks. One such example is the gammadion which is made up of vertical and horizontal rectangular nanostructures. Since the fundamental building blocks of the gammadion can be easily identified, it serves as a good candidate for plasmon hybridisation studies, allowing structural decomposition for easy analysis. The methodology can be validated against other simulations or experimental results. Hybridisation studies allow the field distributions to be shown, allowing for the identification of different modes for a particular structure. Contrary to other studies on resonance modes [7.20], this study utilises the decomposition of a single planar gammadion nanostructure into smaller fundamental nanoparticle elements so as to analyse the field distribution. In the case of complex planar nanostructures, they can be decomposed into fundamental nanoparticle elements depending on the shape of these complex planar nanostructures. For instance, in the case of the left handed gammadion nanostructure, it can be decomposed into several nanowire structures as shown in Fig. 7.17. Similar concepts can be applied to the right handed gammadion nanostructure as well.

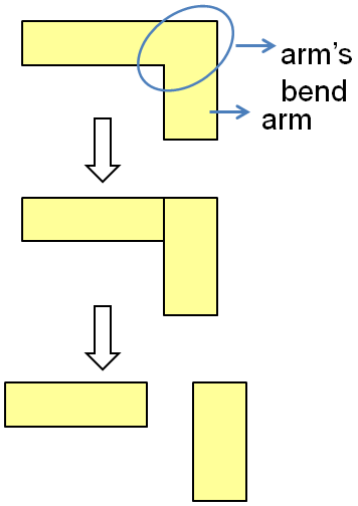

Figure 7.17: Dissection of Gammadion's arm and arm's bend [7.18].

The gammadion's arm and arm's bend are as labelled and it is planar where the arm and arm's bend are interconnected. Treating each nanowire individually, different polarised modes can be induced in accordance to Fig. 7.5 and Fig. 7.12 depending on the polarisation of the excitation light source.

If vertical (y) direction is used as the reference direction for light polarisation, two hybridisation states can be attained through the superposition of the dipole moments in the E_y and E_x polarisation as well as E_y and $-E_x$ polarisation, respectively. The derived charge distribution at each arm and arm's bend of the gammadion are shown in Fig. 7.18(a), 7.18(b) and 7.18(c). This allows resultant dipole moments to be derived in Fig. 7.18(d) and Fig. 7.18(e). Since the y direction is used as the reference direction for light polarisation, two other corresponding polarisation modes can be expected in Fig. 7.18(f) and Fig. 7.18(g). These two hybridised states (Figs. 7.18(d), 7.18(e) and Figs. 7.18(f), 7.18(g)) are a result of opposite field polarity at the arms of the gammadion, derived as a result of charge cancellations due to superposition.

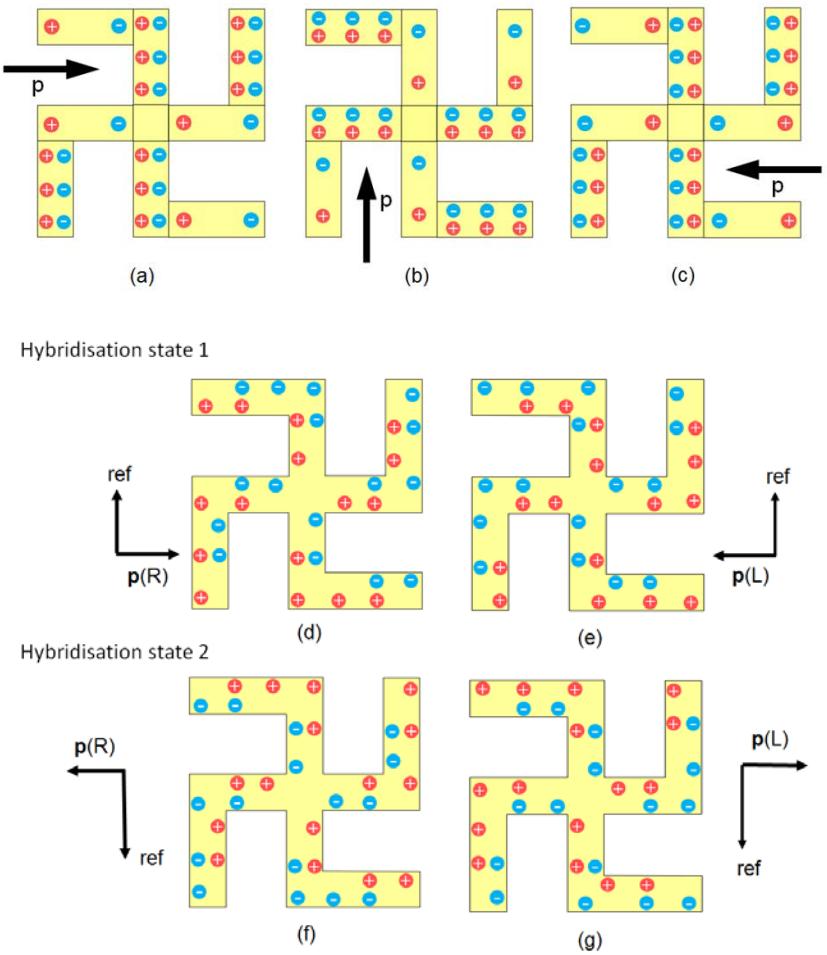

Figure 7.18: Electric dipole moment induced in a single gammadion nanostructure with (a) E_x (b) E_y and (c) $-E_x$ light polarisation. (d) Hybridisation state 1 with RCP. (e) Hybridisation state 1 with LCP. (f) Hybridisation state 2 with RCP. (g) Hybridisation state 2 with LCP [7.18].

If the horizontal (x) direction is used as the reference direction for light polarisation, hybridisation states shown in Figs. 7.19(a), 7.19(b), 7.19(c) and 7.19(d) would be expected.

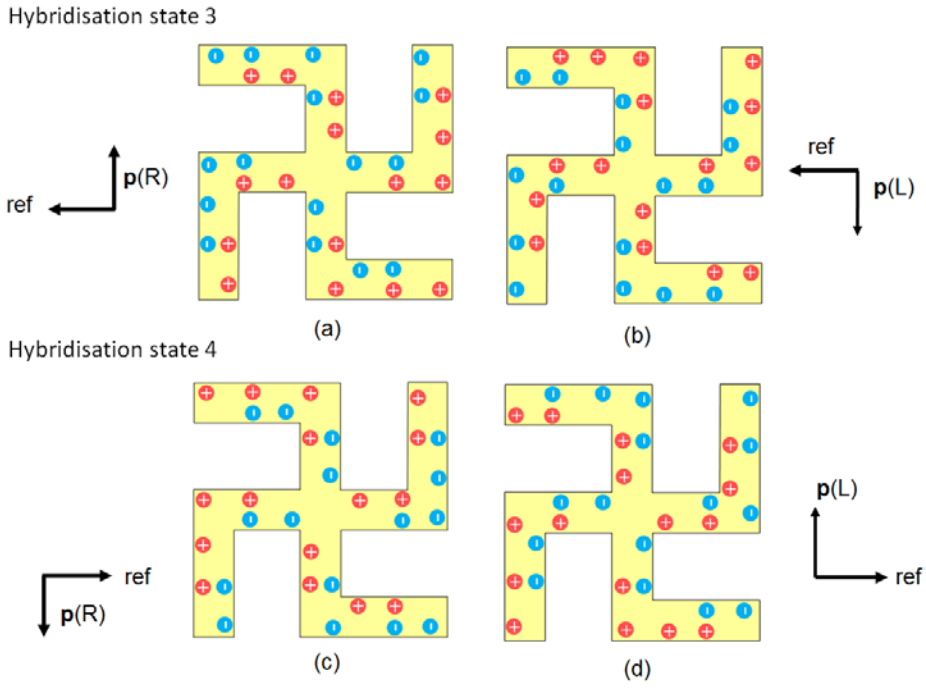

Figure 7.19: (a) Hybridisation state 3 with RCP. (b) Hybridisation state 3 with LCP. (c) Hybridisation state 4 with RCP. (d) Hybridisation state 4 with LCP [7.18].

What this means is that 4 hybridisation states can essentially be excited because the structure is asymmetric. However only 2 hybridisation states can be excited at any one time based on the reference direction adopted. Further, the asymmetric gammadion nanostructure has a rotational symmetry which serves to enhance the chiral effect. To verify the theory, numerical simulations were performed on the left handed gammadion nanostructure shown in Fig. 7.20.

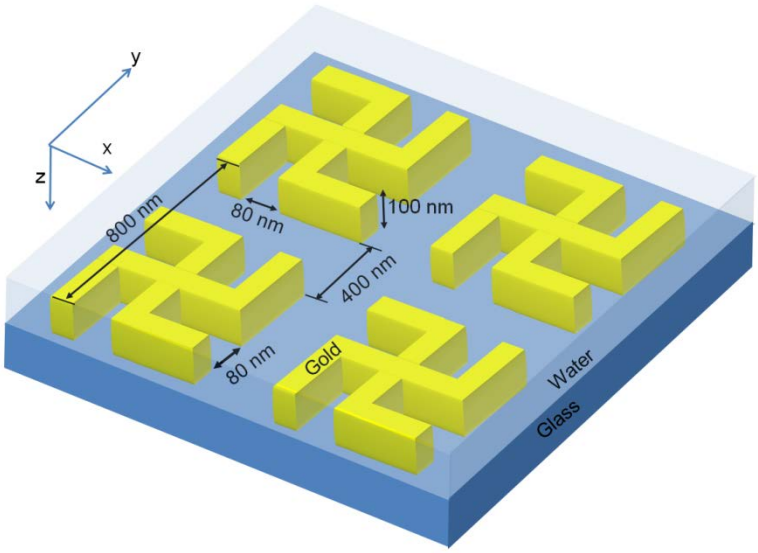

Figure 7.20: Schematic layout of the left handed gammadion structure. Left/right circular polarised wave is incident in the z direction into the planar array [7.18].

As an individual unit, the planar gammadion nanostructure exhibits chiral handedness. The conductive and inductive coupling that results in the gammadion nanostructure forms the hybridised plasmon modes in the CD spectrum. The effects of different modes for sensing chiral molecules are discussed using field distribution, Bloch wave theory and charge distribution, thereby explaining the origin of the CD modes. A left handed gammadion structure shown in Fig. 7.20 was selected to apply the plasmon hybridisation method and study the origin of the CD modes. Such configuration facilitates fabrication and use in a liquid medium for biosensing applications. Similar concepts can be applied to the right handed gammadion structure as well. The incidence of RCP light on the left handed gammadion structure is first considered. Since CD is based on the difference in absorption between the LCP and RCP light, the differences between two linearly polarised waves that contribute to the circular rotation of the waves is considered.

The gammadion structure shown in Fig. 7.20 has a width of 80 nm and a periodicity of 800 nm. It is 100 nm thick, placed on glass substrate and

surrounded by water. Gold is used for the gammadion because it does not oxidise, is chemically inert and biologically compatible. The permittivity values of glass, water, and gold are obtained from the optical handbook [7.19]. The gammadion was simulated using the finite-difference time-domain (FDTD) method with Lorentz-Drude model to account for the damping of the metal. Periodic boundary conditions are used to account for the gammadion array and apply perfectly matched layer to the vertical axis of the array. The simulation grid size is set to 4 nm in all directions to obtain accurate transmission, scattering and reflection spectra. The absorption spectra of the gammadion were obtained and the CD spectrum was derived as shown in Figure 7.21(a). Since the gammadion is a left handed structure, it is expected that more right handed circular polarised light is absorbed [7.21]. This is due to the electric field vector of the right handed circularly polarised light having stronger interactions with the induced electric dipole moments of the left handed gammadion structure. Hence, the CD of the gammadion array is negative at the visible light spectrum, as calculated from Eqn. 7.1.

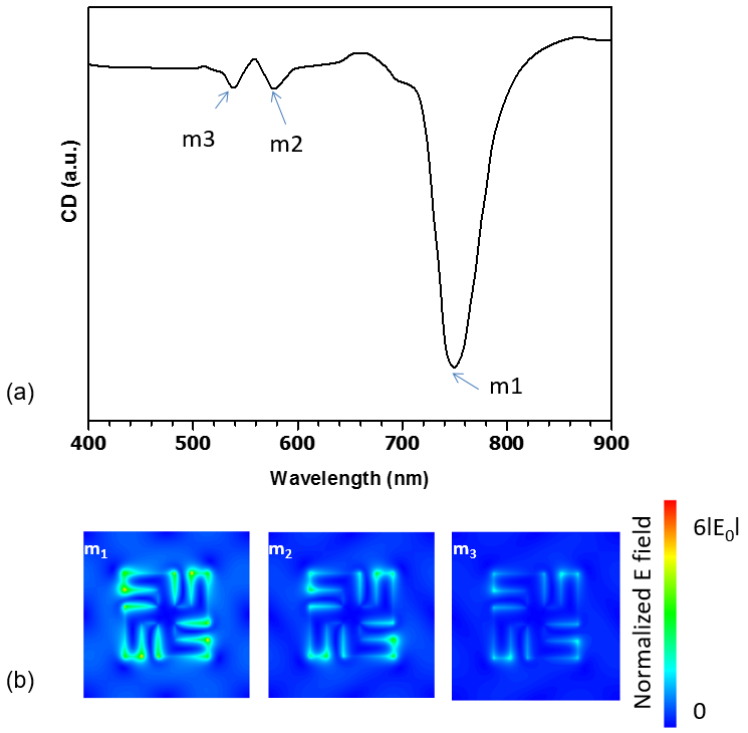

Figure 7.21: (a) Modes obtained from gammadion structure. Mode m1 correspond to Bloch mode while modes m2 and m3 are localised plasmonics modes. (b) Normalised E field distribution of the three modes [7.18].

From Fig. 7.21(a), there are three distinctive CD modes m1, m2 and m3 corresponding to valleys observed at wavelengths of 751 nm, 578 nm, and 524 nm respectively. Mode m1 has the largest CD, while modes m2 and m3 are close to each other and have smaller CD values. Fig. 7.21(b) shows the normalised E_z field distribution of the three modes. Mode m1 was observed to have the largest field distribution spread compared to modes m2 and m3. Mode m1 also shows stronger electric field intensity near the edges of the gammadion. The field distribution is used to investigate the origin of the CD modes. The large and intense field distribution in mode m1 is a result of the interaction between adjacent gammadion structures in a collective array. Secondly, mode m1 is located near the period. The mode arising from the period of the gammadion is given as

$$\lambda_{SPP} = \frac{n_{SPP} a_0}{\sqrt{2}} \qquad (7.2)$$

where a_0 is the period of the structure, n_{SPP} and λ_{SPP} is the effective index and wavelength of the surface plasmon respectively.

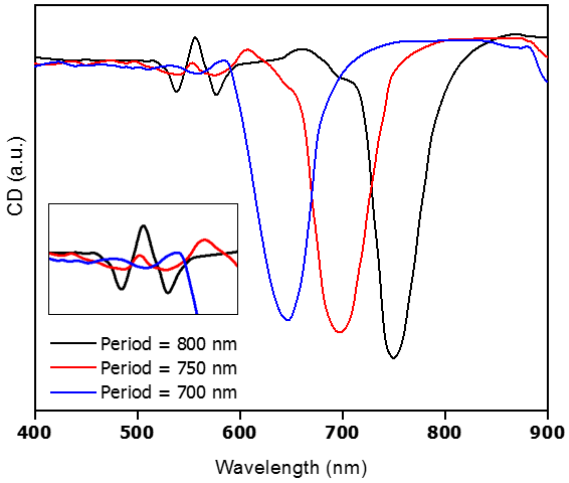

Figure 7.22: Blue shift (Bloch mode effect) in spectrum of mode m1 with a decrease in structure periodicity [7.18].

Figure 7.22 shows the CD spectra with different periods. It is observed that mode m1 blue shifted from 755 nm to 645 nm as the period is reduced from 800 nm to 700 nm. This demonstrates that mode m1 is dependent on the period of the gammadion array and is labelled as the plasmonics CD Bloch mode [7.22, Appendix C].

Modes m2 and m3 are near each other and have similar CD. Their CD is smaller in amplitude because of the inductive and conductive coupling in each individual gammadion nanostructure [7.23]. In addition, the field distribution is localised onto a very small field spread on the gammadion/water interface. Modes m2 and m3 can be deduced to originate from localised surface modes with different polarity distribution. Plotting the dipolar field profile for mode m2 as shown in Fig. 7.23(a) and Fig. 7.23(b),

regions of maxima and minima field intensity are observed to be congregated around the edges, particularly at the regions whereby the adjacent arms are in close proximity to each other. Only fields that are oriented in the z direction are plotted in this figure. There is strong coupling between positive and negative poles, resulting in enhanced local electric field intensity. Similar features can be observed from mode m3 as well, with its field plots and corresponding schematic being shown in Figs. 7.23(c) and 7.23(d), respectively.

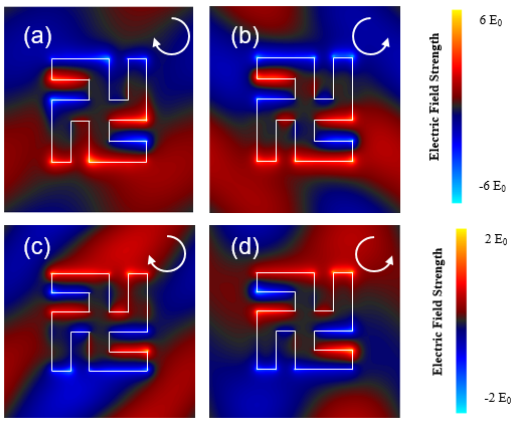

Figure 7.23: E field profile (a) Mode m2 RCP hybridised state. (b) Mode m2 LCP hybridised state. (c) Mode m3 RCP hybridised state. (d) Mode m3 LCP hybridised state [7.18].

The E field profile of the mode m2 hybridised state with RCP and LCP exhibits a polarity profile in the arms and arms' bend that is inversely related to the m3 hybridised state with RCP and LCP. The pair of modes, m2 and m3 is the result of the presence of a mixture of inductive and conductive coupling respectively, as termed in [7.17]. As discussed, hybridisation can be defined as the formation of different energy states as a result of interactions resulting from both inductive and conductive coupling [7.10]. The E field profile for modes m2 and m3 shown in Figs. 7.23(a) to 7.23(d) resembles the derived

electric dipole moments in Figs. 7.18(d) to 7.18(g). This strong agreement further augments the validity of applying plasmon hybridisation method on complex nanostructures.

Considering the planar gammadion nanostructure, when the basic nanowire nanostructures are placed close together, there will be dipole interactions resulting in inductive and conductive coupling which in turn leads to the formation of different energy/hybridisation states. The interaction of the induced dipole moments between adjacent/neighbouring nanoparticle elements makes up the overall induced dipole moment for the entire nanostructure. Inductive coupling occurs as a result of the coupling of dipoles between the arms and their adjacent arms' bends while conductive coupling refers to the coupling of the resultant dipoles in the structure. Within the gammadion, there exists not just coupling between purely two transverse or two longitudinal dipoles but also coupling between a transverse and longitudinal dipole. Extending the mathematical formulation for interaction energy between a longitudinal dipole and a point source [Appendix D.1], we can calculate the interaction energy between two purely transverse/longitudinal dipoles [7.11, Appendix D.2-D.5] which is given by

$$H_{int} = \gamma \frac{p_1 p_2}{4\pi\varepsilon_0 r^3}, \qquad (7.3)$$

where $p_{1,\,2}$ are dipole moments and r is the distance away from the interaction centre. Parameter γ is called the interaction index and can be assigned +1 or -2, depending on whether it is a transverse or longitudinal coupling. H_{int} between a transverse and longitudinal dipole [Appendix D.5] is derived to be

$$H_{int} = \frac{\left(\frac{3}{2}d\right)p_1 p_2}{4\pi\varepsilon_0 r^4} \qquad (7.4)$$

γ has a value of 3d/2r. This means that H_{int} decreases to zero more rapidly for coupling between longitudinal and transverse dipoles than coupling between two purely transverse/longitudinal dipoles. Apart from the merging of the partial charges of the dipoles as r increases, the reason for the rapid decrease in H_{int} is due to the increased separation of the charges on the far ends of the longitudinal and transverse dipole.

Hence, we can define modes m2 and m3 as hybridised modes. From the earlier derivation, the rapid decrease of H_{int} affects the strength of the CD signal for both modes m2 and m3. Earlier, Figs. 7.18(d) and 7.18(e) shows the sign distribution of the whole gammadion structure. The polarity of the field at the arm and arm's bend of the gammadion determine the nature of the modes in the absorption spectrum. This subsequently affects the nature of the modes in the CD spectrum. Mode m2 lies at a higher resonance wavelength (578 nm) than mode m3 (524 nm). The different polarity profile for m2 and m3 hybridised state with LCP and RCP explains why the CD modes m2 and m3 are at different wavelength.

Hence, by changing the gap distance between the arm and the adjacent arm's bend of the gammadion, the CD of modes m2 and m3 will change. In Fig. 7.24(a), we observed that the CD magnitude of mode m2 and m3 decreases as the gap increases from 70 to 90 nm. This is due to weaker inductive coupling between dipoles on the adjacent arms. In Fig. 7.24(b), the wavelength of mode m2 blue shifted and m3 red shifted. The weakened interaction between the dipoles causes the energy difference between the two hybridisation states to decrease, hence decreasing the wavelength difference between mode m2 and m3 simultaneously [Appendix E]. On the other hand,

decreasing the gap distance causes stronger inductive coupling. The stronger interaction results in larger energy difference between the two hybridisation states and causes a higher wavelength difference between mode m2 and m3. A larger CD difference is observed for m2 and m3.

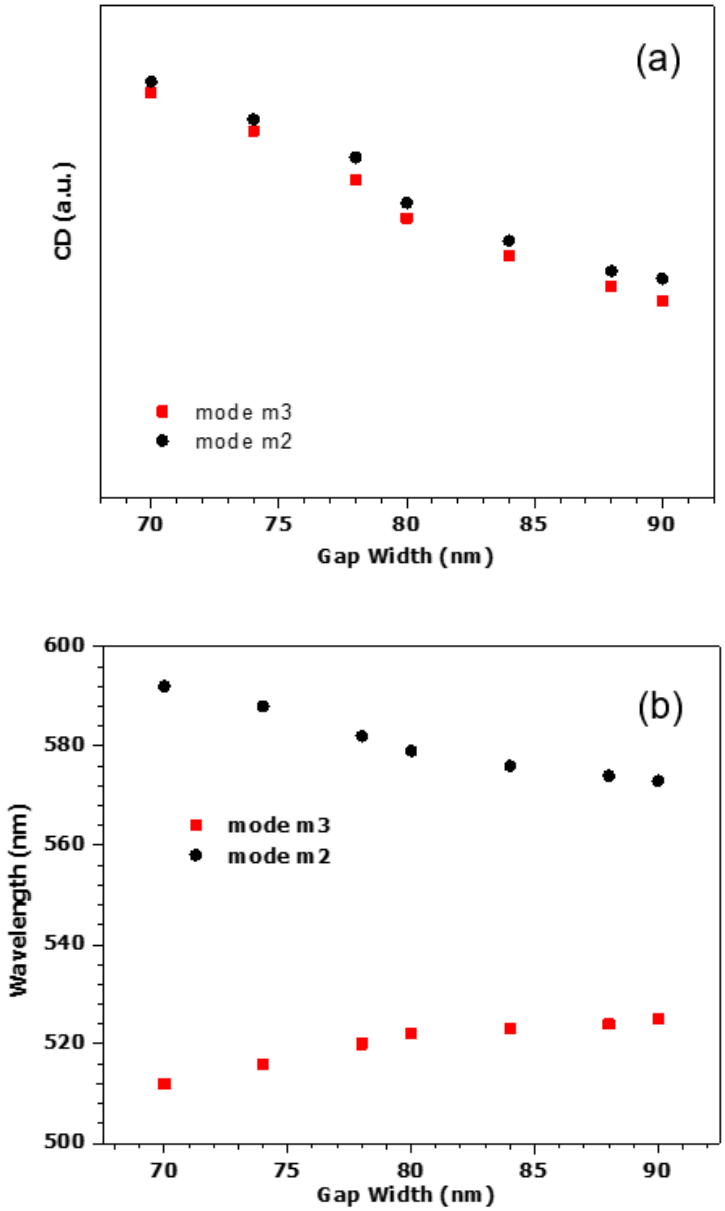

Figure 7.24: (a) CD plot for mode m2 and m3 with various gap widths. (b) Wavelength shift of mode m2 and m3 with various gap widths [7.18].

Since mode hybridisation occurs simply because of inductive and conductive coupling, this means that a single structure can support more than

one hybridisation mode. Also, from the field intensity plots, mode m2 is seen to give slightly stronger CD signal than mode m3. This in turn infers a stronger absorption for mode m2 than mode m3 and hence a stronger CD. Since mode m2 occurs at a higher wavelength than mode m3, this means that there is a higher probability of absorption at higher wavelength, cumulating in the stronger CD signal attained.

In theory, the hybrid modes of m2 and m3 in the CD spectrum can be explained using the Born-Kuhn oscillation model for optical activity. The arm and arm's bend of the gammadion can be approximated by two harmonic oscillators [7.24], which give rise to inductive and conductive coupling. Hence, as the distance between the arm and arm's bend increases, the coupling weakens [7.24]. By using the Maxwell equation for dispersive dielectric materials, $\overline{D} = \varepsilon_0 \overline{\mathrm{E}} + \overline{\mathrm{P}}$, the Born-Kuhn model gives two solutions for the average refractive index of the chiral gammadion with LCP and RCP light incidence. Using the two electron chiral molecule oscillation model and considering nonlocality of the first order dispersion [7.25], the solutions to the Born-Kuhn oscillation model is given as

$$\omega_{2,3}{}^2 = \omega_0{}^2 + \xi, \qquad (7.5)$$

where the subscripts refer to modes m2 and m3. The parameter ω_0 is the natural frequency of the oscillation pair (or the CD hybrid modes) and ξ is the coupling between arm and arm's bend. As the gammadion is asymmetrical, the coupling between the arm and arm's bend is different, thereby giving rise to the shift in wavelength as shown in Fig. 7.24(b).

7.6. Summary

The protruded segment was manipulated to implement asymmetric directivity. Such asymmetric directivity is possible by harnessing excited surface eigenmodes on a metal nanostructure placed below the protruded tip, forming a double protruded metal-insulator-metal (p^2MIM) structure. The localised SPPs on the surface of the nanostructures are then used to tune the directivity of propagating SPPs. There exists a correlation between localised SPP eigenmodes excited by tunnelling current with the circular dichroism (CD) signature of nanostructures excited by circularly polarised waves. This allows us to predict the excited localised SPP eigenmodes on basic triangular, circular and rectangular nanostructures using the plasmon hybridisation method. Using the plasmon hybridisation method as a tool, the localised SPP eigenmodes of basic and complex nanostructures can be determined. This serves as a basis from which a nanostructure can be designed to create a desired surface eigenmode profile which induces asymmetric directivity.

7.7. References

[7.1] A.F. Koenderink, “Plasmon nanoparticle array waveguides for single photon and single plasmon sources”, Nano Letters, 9(12), 4228-4233 (2009)

[7.2] A.G. Curto, G. Volpe, T.H. Taminiau, M.P. Kreuzer, R. Quidant and N.F. van Hulst, “Unidirectional emission of a quantum dot coupled to a nanoantenna”, Science, 329(5994), 930-933 (2010)

[7.3] R. Esteban, T.V. Teperik and J.J. Greffet, “Optical patch antennas for single photon emission using surface plasmon resonances”, Physical Review Letters, 104(2), 026802 (2010)

[7.4] F. Huang, X. Jiang, H. Yang, S. Li and X. Sun, “Tunable directional coupling of surface plasmon polaritons with linearly polarised light”, Applied Physics B Lasers and Optics, 122(1), 1-6 (2016)

[7.5] R.H. Ritchie, E.T. Arakawa, J.J. Cowan and R.N. Hamm, “Surface plasmon resonance effect in grating diffraction”, Physical review letters, 21(22), 1530-1533 (1968)

[7.6] G.D. Fasman, *Circular dichroism and the conformational analysis of biomolecules*. (Plenum US, New York 1996)

[7.7] N.J. Greenfield, “Using circular dichroism spectra to estimate protein secondary structure”, Nat Protocols, 1(6), 2876 (2007)

[7.8] D.H.A. Correa and C.H.I. Ramos, “The use of circular dichroism spectroscopy to study protein folding, form and function”. African Journal of Biochemistry Research, 3(5), 164 (2009)

[7.9] E. Hendry, T. Carpy, J. Johnston, M. Popland, R.V. Milhaylovskiy, A.J. Lapthorn, S.M. Kelly, L.D. Barron, N. Gadegaard and M.

Kadodwala, “Ultrasensitive detection and characterisation of biomolecules using superchiral fields”, Nature Nanotechnology, 5(11), 783 (2010)

[7.10] E. Prodan, C. Radloff, N.J. Halas and P. Nordlander, “A hybridisation model for the plasmon response of complex nanostructures”, Science, 302(6544), 419 (2003)

[7.11] H. Wang, D.W. Brandl, F. Le, P. Nordlander and N.J. Halas, “Nanorice: A hybrid plasmonic nanostructure”, Nano letters, 6(4), 827 (2006)

[7.12] F. Hao, C.L. Nehl, J.H. Hafner and P. Nordlander, “Plasmon resonances of a gold nanostar”, Nano Letters, 7(3), 729-732 (2007)

[7.13] E. Prodan and P. Nordlander, “Plasmon hybridisation in spherical nanoparticles”, Journal of chemical physics, 120(11), 5444 (2004)

[7.14] K. Bao, H. Sobhani and P. Nordlander, “Plasmon hybridisation for real metals”, Chinese science bulletin, 55(24), 2629 (2010)

[7.15] P. Nordlander and E. Prodan, “Plasmon hybridisation in nanoparticles near metallic surfaces”, Nano letters, 4(11), 2209-2213 (2009)

[7.16] J.B. Lassiter, J. Azipurua, L.I. Hernandez, D.W. Brandl, I. Romero, S. Lal, J.H. Hafner, P. Nordlander and N.J. Halas, “Close encounters between two nanoshells”, Nano Letters, 8(4), 1212 (2008)

[7.17] N. Liu and H. Giessen, “Coupling effects in optical metamaterials”, Angewandte Chemie, 49(51), 9383 (2010)

[7.18] W.K. Phua, Y.L. Hor, E.S.P. Leong, Y.J. Liu and E.H. Khoo, “Study of circular dichroism modes through decomposition of planar nanostructures”, Plasmonics, 1-9 (2015)

[7.19] E.D. Palik, *Handbook of optical constants of solids*, (Academic Press, 1998)

[7.20] R. Zhao, L. Zhang, J. Zhou, Th. Koschny and C.M. Soukoulis, "Conjugated gammadion chiral metamaterial with uniaxial optical activity and negative refractive index", Physical Review B, 83(3), 035105 (2011)

[7.21] A. Rodger and B. Norden, *Circular dichroism and linear dichroism*, (Oxford University Press, 1997)

[7.22] S.A. Maier, *Plasmonics: Fundamentals and Applications*, (Springer Publishers, 2007)

[7.23] Yu.P. Svirko and N.I. Zheludev, *Polarisation of Light in Nonlinear Optics*, Wiley Press, 1998.

[7.24] M. Born, "The natural optical activity of liquids and gases", Physikal Z, 16, 251 (1915)

[7.25] X. Yin, M. Schaferling, B. Metzger and H. Giessen, "Interpreting chiral nanophotonic spectra: The plasmonic Born-Kuhn model", Nano Letters, 13(12), 6238 (2013)

Chapter 8. Conclusion and future work

8.1. Conclusion

The electrical excitation of SPPs using proposed pMIM and p^2MIM structures opens up the possibility of integrating plasmon sources onto nanoscale optoelectronic integrated circuits to facilitate on-chip data communications. pMIM structures provide a source of long propagating surface plasmon polaritons which can propagate a long distance of up to 30 μm. The protruded tip not only provides a source of excitation for the tunnelling current but also serves to enhance the emitted power from the tunnelling current, with the concave tip profile providing the strongest enhancement.

An efficient approach has been proposed to excite long travelling plasmon polaritons. Various eigenmodes can be supported in the pMIM's waveguiding segment and these eigenmodes provides different contributions to the excited propagating SPP eigenwaves. By performing decomposition on the excited propagating SPP eigenwaves, the contribution of each eigenmode can be identified. The magnitude of bias voltages can also be controlled to determine the operating regime of the pMIM so as to excite desired eigenmodes with high efficiencies.

To realise a compact pMIM configuration with negligible leakage radiation, metal substrate can be finite but it has to sustain a thickness of more than 150 percent of the skin depth in the metal, with reference to an Au-SiO_2-

Au pMIM configuration. Leakage radiation can be used as means of detection for excited plasmon polaritons as well as to gather deeper insights behind elastic and inelastic tunnelling processes on the generation of excited plasmon polaritons.

The p^2MIM could improve the directivity of excited plasmon polaritons and builds upon the pMIM structure with the inclusion of a double protrusion in the protruded segment. Such double protrusion includes a bottom nanostructure in addition to a top protruded tip and allows asymmetric directivity to be achieved by exciting localised SPP eigenmodes on the metal nanostructures. These excited localised SPP eigenmodes can be predicted by making use of a correlation with the circular dichroism signature of the nanostructures.

8.2. Future work

While the research for on-chip electrically excited plasmon sources is still very much in its infant stages, the current findings provide the feasibility study of using complex 3D nanostructures in p^2MIM structures to generate large area localised directionally propagating surface plasmon polaritons. It also serves as a proof of concept for further studies to be conducted. Some of the technical problems that can be further studied in the future are detailed as follows.

Firstly, work could be done on enhancing the overall power emitted by the excitation source. In this work, the focus lies on the simplest case of a single protrusion and tip. Hence, the power is calculated per tip. Due to the low magnitude of the tunnelling current, the power emitted by each tip is only in the order of hundreds of aW (1e-18W). One solution to increase the emitted power and apply such proof of concept to real life applications is to make use of a single tip in the center with surrounding tips optimized based on the self-similarity principle [8.1]. The other solution could be to use an array of tips.

Secondly, tunnel junctions with different materials in the gap could be explored. This includes materials such as molecular tunnelling junction. The presence of different tunnel junctions could change the energy barrier and make it easier to excite a tunnelling current which is of stronger intensity.

Thirdly, nanostructures can be engineered on the substrate below the tip to induce the desired surface eigenmode with good directivity. This could at the same time, enhance the overall power emitted by the excitation source.

Lastly, the directivity can be enhanced by making use of engineered gratings on the top/bottom metal electrodes.

To use pMIM and p^2MIM structures in practical applications, an array of protrusions or multiple tips on a single protrusion can be adopted to increase the overall generated power.

8.3. References

[8.1] K. Li, M.I. Stockman and D.J. Bergman, “Self similar chain metal nanospheres as an efficient nanolens”, Physical Review Letters, 91(22) 227402 (2003)

Appendices

A. Extrapolation of material permittivity to low energies

To perform the extrapolation, we use the Drude model.

$$\varepsilon_r(\omega) = 1 - \frac{{\omega_p}^2}{\omega^2 + {\gamma_g}^2} + \frac{i{\omega_p}^2\gamma_g}{\omega^3 + \omega{\gamma_g}^2}$$

$$Real\ component\ of\ \varepsilon_r(\omega) = real\ \varepsilon_r(\omega) = 1 - \frac{{\omega_p}^2}{\omega^2 + {\gamma_g}^2}$$

$$\approx -\frac{{\omega_p}^2}{\omega^2 + {\gamma_g}^2}$$

$$Imaginery\ component\ of\ \varepsilon_r(\omega) = Imag\ \varepsilon_r(\omega) = \frac{{\omega_p}^2\gamma_g}{\omega^3 + \omega{\gamma_g}^2}$$

$$\frac{Imag\ \varepsilon_r(\omega)}{real\ \varepsilon_r(\omega)} = -\frac{\gamma_g}{\omega}$$

$$\gamma_g = -\omega\frac{Imag\ \varepsilon_r(\omega)}{real\ \varepsilon_r(\omega)}$$

$${\omega_p}^2 = -\left(\omega^2 + {\gamma_g}^2\right)real\varepsilon_r(\omega)$$

Having obtained these 2 main expressions, the material properties for e.g. last 3 frequencies of interest that can be used to calculate the average value of γ_g and ${\omega_p}^2$. Then these average values are used in $real\ \varepsilon_r(\omega) = -\frac{{\omega_p}^2}{\omega^2+{\gamma_g}^2}$ and $Imag\ \varepsilon_r(\omega) = \frac{{\omega_p}^2\gamma_g}{\omega^3+\omega{\gamma_g}^2}$ to calculate the next extrapolated frequency of interest.

B. Power emitted by tunnelling current for a pMIM structure with triangular tip of different gap thickness

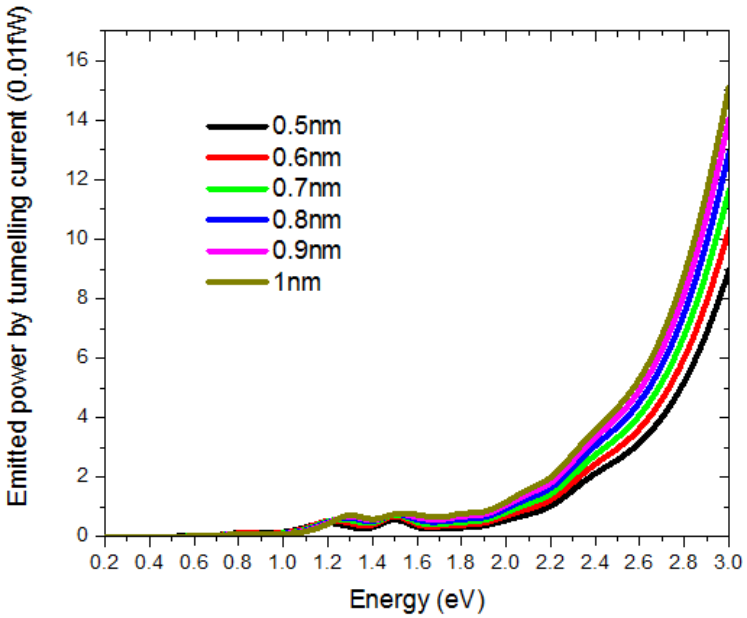

Figure B: Power emitted by tunnelling current (fW) vs Energy (eV) for pMIM triangular tip of different gap thickness if tunnelling current is kept constant for 1nm gap across different gap separations

C. Correlation of mode m1 with period of the gammadion array, a0

The period of the gammadion array, a0 is varied in the equation.

$$\lambda_{SPP} = \frac{n_{SPP} a_0}{\sqrt{n^2+m^2}} \qquad (A6.1)$$

Since the structure is made up of fundamental building blocks, only fundamental SPP modes are considered. For fundamental SPP modes, n = m = 1. The effective localised surface plasmon is given as

$$n_{SPP} = \sqrt{\frac{\varepsilon_{Au}\varepsilon_d}{\varepsilon_{Au}+\varepsilon_d}} \qquad (A6.2)$$

The graph of Eqn. A6.1 with the wavelength positions of mode m1 in the CD spectra for different periods of the gammadion array. The gammadion array with periods of 850 nm, 800 nm, 750 nm, 700 nm and 650 nm is simulated. Figure A6.1 shows the comparison between the model and simulation results.

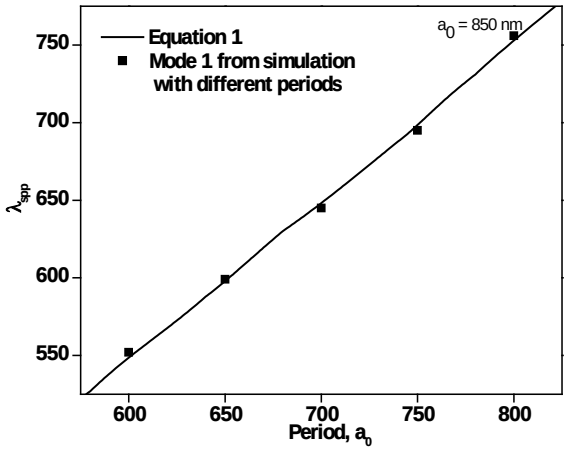

Figure C: Plot of the equation 1 and mode1 from CD spectra.

From Fig. C, Eqn. A6.1 and the wavelength positions of mode m1 in CD spectra matches nicely.

D. Interaction energy to account for conductive coupling

Circularly polarised light involves the superposition of both E_x and E_y polarised waves, assuming that the wave propagates in the z direction. Hence, it requires the consideration of both longitudinal and transverse coupling. Both transverse and longitudinal dipoles can be represented as a separation of positive and negative charges $+q$ and $-q$ respectively. Similarly, a point charge can be represented by a positive charge q. $\frac{1}{4\pi\varepsilon_0}$ refers to the electrostatic constant while r is the distance between the midpoint of the dipoles or point charge and d refers to the length of the dipole.

D.1. Interaction energy, U between a longitudinal dipole and a point charge

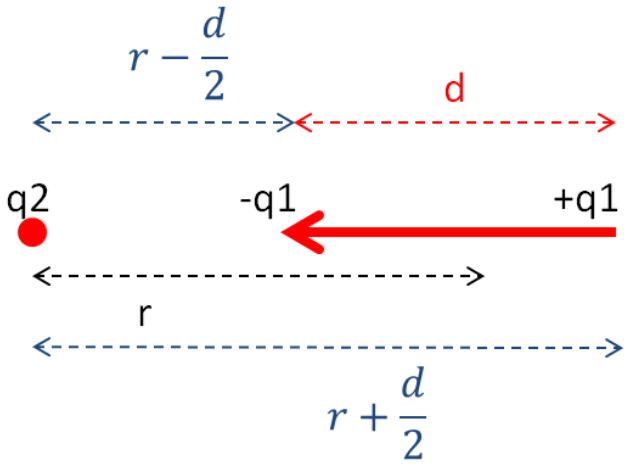

Figure D.1: Coupling between a longitudinal dipole and a point charge

$$U = \frac{1}{4\pi\varepsilon_0}\left[\frac{(q_1)(q_2)}{r+\frac{d}{2}} + \frac{(-q_1)q_2}{r-\frac{d}{2}}\right] = \frac{q_1 q_2}{4\pi\varepsilon_0}\left(\frac{1}{r+\frac{d}{2}} - \frac{1}{r-\frac{d}{2}}\right)$$

$$= \frac{q_1 q_2}{4\pi\varepsilon_0 r}\left(\frac{1}{1+\frac{d}{2r}} - \frac{1}{1-\frac{d}{2r}}\right)$$

To simplify the expression, let $x = \frac{d}{2r}$

Using Taylor Series Expansion ,

$$\frac{1}{1-x} \approx (1-x)^{-1} \approx 1 + x + x^2 + x^3 + x^4 + O(x^5) \approx 1 + x + x^2$$

$$\frac{1}{1+x} \approx (1+x)^{-1} \approx 1 - x + x^2 - x^3 + x^4 + O(x^5) \approx 1 - x + x^2$$

Because d<<r, higher orders of x are neglected.

$$U = \frac{q_1 q_2}{4\pi\varepsilon_0 r}\left(\frac{1}{1+\frac{d}{2r}} - \frac{1}{1-\frac{d}{2r}}\right)$$

$$\approx \frac{q_1 q_2}{4\pi\varepsilon_0 r}\left(1 - x + x^2 - (1 + x + x^2)\right) \approx \frac{-2q_1 q_2 x}{4\pi\varepsilon_0 r}$$

$$\approx \frac{-q_1 d q_2}{4\pi\varepsilon_0 r^2} \approx \frac{-p_1 p_2}{4\pi\varepsilon_0 r^3} \approx \gamma\frac{p_1 p_2}{4\pi\varepsilon_0 r^3}$$

where $p_1 = q_1 d$ and $p_2 = q_2$ and $\gamma = -1$ for longitudinal coupling between dipole and point charge. $p_{1,2}$ refers to the dipole moment of 1 and 2 respectively.

D.2. Interaction energy, U between two transverse dipoles of the same orientation

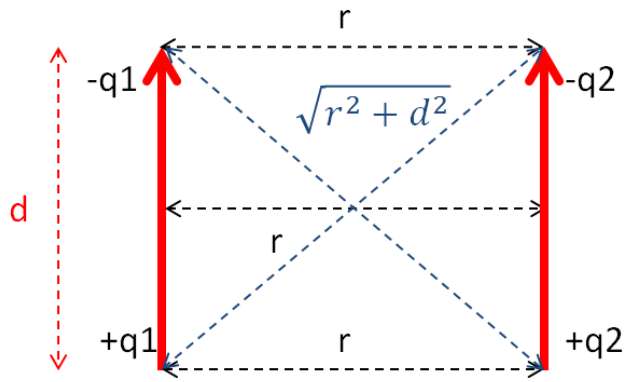

Figure D.2: Coupling between two transverse dipoles of same orientation

$$U = \frac{1}{4\pi\varepsilon_0}\left[\frac{(q_1)(q_2)}{r} + \frac{(-q_1)q_2}{\sqrt{r^2+d^2}} + \frac{q_1(-q_2)}{\sqrt{r^2+d^2}} + \frac{(-q_1)(-q_2)}{r}\right]$$

$$= \frac{q_1 q_2}{4\pi\varepsilon_0}\left(\frac{2}{r} - \frac{1}{r\sqrt{1+\left(\frac{d}{r}\right)^2}} - \frac{1}{r\sqrt{1+\left(\frac{d}{r}\right)^2}}\right)$$

$$= \frac{q_1 q_2}{4\pi\varepsilon_0 r}\left(2 - \frac{2}{\sqrt{1+\left(\frac{d}{r}\right)^2}}\right)$$

To simplify the expression, let $x = \frac{d}{r}$

Using Taylor Series Expansion,

$$\frac{1}{\sqrt{1+x^2}} \approx (1+x^2)^{-\frac{1}{2}} \approx 1 + \frac{x^2}{2} + \frac{3x^4}{8} + O(x^5) \approx 1 + \frac{x^2}{2}$$

Because d<<r, we neglect higher orders of x

$$U = \frac{q_1 q_2}{4\pi\varepsilon_0 r}\left(2 - \frac{2}{\sqrt{1+\left(\frac{d}{r}\right)^2}}\right) \approx \frac{q_1 q_2}{4\pi\varepsilon_0 r}\left(2 - 2\left(1 + \frac{x^2}{2}\right)\right) \approx \frac{q_1 q_2 x^2}{4\pi\varepsilon_0 r}$$

$$\approx \frac{q_1 d q_2 d}{4\pi\varepsilon_0 r^3} \approx \frac{p_1 p_2}{4\pi\varepsilon_0 r^3} \approx \gamma \frac{p_1 p_2}{4\pi\varepsilon_0 r^3}$$

where $p_1 = q_1 d$ and $p_2 = q_2 d$ and $\gamma = 1$ for transverse coupling. $p_{1,2}$ refers to the dipole moment of 1 and 2 respectively.

D.3. Interaction energy, U between two transverse dipoles of different orientation

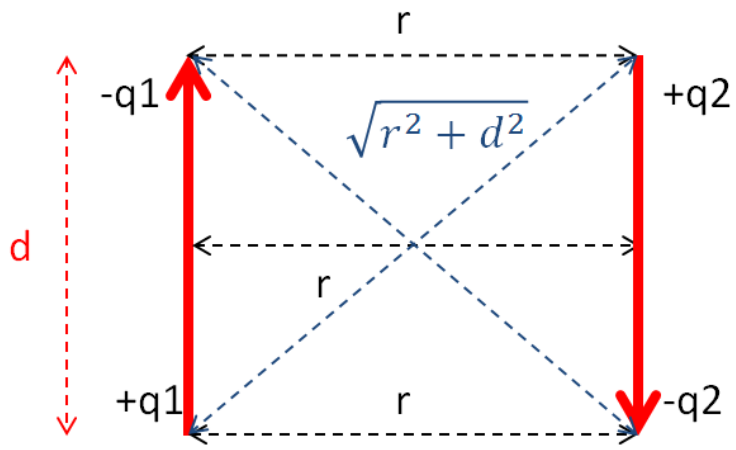

Figure D.3: Coupling between two transverse dipoles of different orientation

$$U = \frac{1}{4\pi\varepsilon_0}\left[\frac{(q_1)(q_2)}{\sqrt{r^2+d^2}} + \frac{(-q_1)q_2}{r} + \frac{q_1(-q_2)}{r} + \frac{(-q_1)(-q_2)}{\sqrt{r^2+d^2}}\right]$$

$$= \frac{q_1 q_2}{4\pi\varepsilon_0}\left(\frac{2}{\sqrt{r^2+d^2}} - \frac{2}{r}\right) = \frac{2q_1 q_2}{4\pi\varepsilon_0 r}\left(\frac{1}{\sqrt{1+\left(\frac{d}{r}\right)^2}} - 1\right)$$

$$= -\frac{2q_1 q_2}{4\pi\varepsilon_0 r}\left(1 - \frac{1}{\sqrt{1+\left(\frac{d}{r}\right)^2}}\right)$$

To simplify the expression, let $x = \frac{d}{r}$

Using Taylor Series Expansion,

$$\frac{1}{\sqrt{1+x^2}} \approx (1+x^2)^{-\frac{1}{2}} \approx 1 + \frac{x^2}{2} + \frac{3x^4}{8} + O(x^5) \approx 1 + \frac{x^2}{2}$$

Because d<<r, we neglect higher orders of x

$$U = -\frac{2q_1q_2}{4\pi\varepsilon_0 r}\left(1 - \frac{1}{\sqrt{1+\left(\frac{d}{r}\right)^2}}\right) \approx -\frac{2q_1q_2}{4\pi\varepsilon_0 r}\left(1 - \left(1 + \frac{x^2}{2}\right)\right)$$

$$\approx \frac{q_1q_2x^2}{4\pi\varepsilon_0 r} \approx \frac{q_1dq_2d}{4\pi\varepsilon_0 r^3} \approx \frac{p_1p_2}{4\pi\varepsilon_0 r^3} \approx \gamma\frac{p_1p_2}{4\pi\varepsilon_0 r^3}$$

where $p_1 = q_1d$ and $p_2 = q_2d$ and $\gamma = 1$ for transverse coupling. $p_{1,2}$ refers to the dipole moment of 1 and 2 respectively.

D.4. Interaction energy, U between two longitudinal dipoles of same orientation

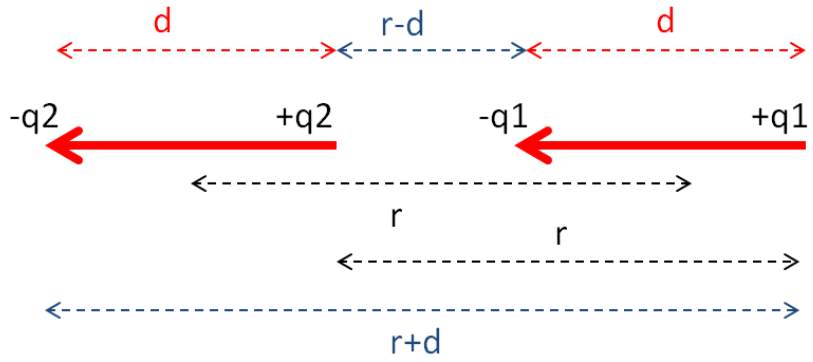

Figure D.4: Coupling between two longitudinal dipoles

$$U = \frac{1}{4\pi\varepsilon_0}\left[\frac{(q_1)(q_2)}{r} + \frac{(-q_1)q_2}{r-d} + \frac{q_1(-q_2)}{r+d} + \frac{(-q_1)(-q_2)}{r}\right]$$

$$= \frac{q_1 q_2}{4\pi\varepsilon_0}\left(\frac{2}{r} - \frac{1}{r-d} - \frac{1}{r+d}\right)$$

$$= \frac{-q_1 q_2}{4\pi\varepsilon_0 r}\left(-2 + \frac{1}{1-\frac{d}{r}} + \frac{1}{1+\frac{d}{r}}\right)$$

To simplify the expression, let $x = \frac{d}{r}$

Using Taylor Series Expansion,

$$\frac{1}{1-x} \approx (1-x)^{-1} \approx 1 + x + x^2 + x^3 + x^4 + O(x^5) \approx 1 + x + x^2$$

$$\frac{1}{1+x} \approx (1+x)^{-1} \approx 1 - x + x^2 - x^3 + x^4 + O(x^5) \approx 1 - x + x^2$$

Because d<<r, higher orders of $x^3$and above are neglected

$$U = \frac{-q_1 q_2}{4\pi\varepsilon_0 r}\left(-2 + \frac{1}{1-\frac{d}{r}} + \frac{1}{1+\frac{d}{r}}\right)$$

$$\approx -\frac{q_1 q_2}{4\pi\varepsilon_0 r}(-2 + 1 - x + x^2 + 1 + x + x^2)$$

$$\approx -\frac{2q_1 q_2 x^2}{4\pi\varepsilon_0 r} \approx -2\frac{q_1 d q_2 d}{4\pi\varepsilon_0 r^3} \approx -2\frac{p_1 p_2}{4\pi\varepsilon_0 r^3} \approx \gamma\frac{p_1 p_2}{4\pi\varepsilon_0 r^3}$$

where $p_1 = q_1 d$ and $p_2 = q_2 d$ and $\gamma = -2$ for longitudinal coupling. $p_{1,2}$ refers to the dipole moment of 1 and 2 respectively.

D.5: Interaction energy, U between a transverse dipole and a longitudinal dipole

x_1 is defined to be the distance between $-q_1$ and $-q_2$, x_2 to be the distance between $-q_1$ and $+q_2$, x_3 to be the distance between $+q_1$ and $-q_2$, and x_4 to be the distance between $+q_1$ and $+q_2$.

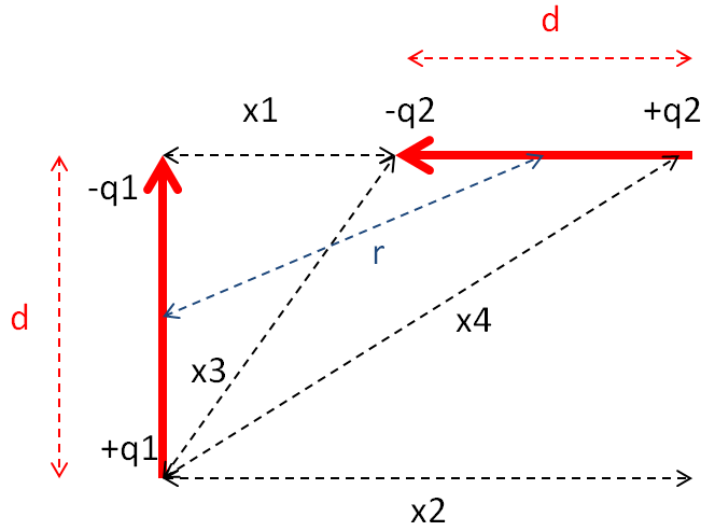

Figure D.5: Coupling between a transverse and a longitudinal dipole

$$U = \frac{1}{4\pi\varepsilon_0}\left[\frac{(-q_1)(-q_2)}{x_1} + \frac{(-q_1)q_2}{x_2} + \frac{q_1(-q_2)}{x_3} + \frac{q_1 q_2}{x_4}\right]$$

$$= \frac{q_1 q_2}{4\pi\varepsilon_0}\left(\frac{1}{x_1} - \frac{1}{x_2} - \frac{1}{x_3} + \frac{1}{x_4}\right)$$

To obtain values for x_1, x_2, x_3, and x_4, the Pythagoras theorem is used,

$$\left(x_1 + \frac{d}{2}\right)^2 + \left(\frac{d}{2}\right)^2 = r^2$$

$$x_1 = \sqrt{r^2 - \left(\frac{d}{2}\right)^2} - \frac{d}{2} = r\left(\sqrt{1 - \left(\frac{d}{2r}\right)^2} - \frac{d}{2r}\right)$$

$$x_2 = x_1 + d = r\left(\sqrt{1-\left(\frac{d}{2r}\right)^2} - \frac{d}{2r}\right) + d$$

$$= r\left(\sqrt{1-\left(\frac{d}{2r}\right)^2} + \frac{d}{2r}\right)$$

$$x_3{}^2 = d^2 + x_1{}^2 = d^2 + \left(\sqrt{r^2-\left(\frac{d}{2}\right)^2} - \frac{d}{2}\right)^2$$

$$= d^2 + r^2 - \left(\frac{d}{2}\right)^2 - d\sqrt{r^2-\left(\frac{d}{2}\right)^2} + \left(\frac{d}{2}\right)^2$$

$$= d^2 + r^2 - d\sqrt{r^2-\left(\frac{d}{2}\right)^2}$$

$$x_3 = \sqrt{d^2 + r^2 - d\sqrt{r^2-\left(\frac{d}{2}\right)^2}} = r\sqrt{\left(\frac{d}{r}\right)^2 + 1 - \frac{d}{r}\sqrt{1-\left(\frac{d}{2r}\right)^2}}$$

$$x_4{}^2 = d^2 + x_2{}^2 = d^2 + \left(\sqrt{r^2-\left(\frac{d}{2}\right)^2} + \frac{d}{2}\right)^2$$

$$= d^2 + r^2 - \left(\frac{d}{2}\right)^2 + d\sqrt{r^2-\left(\frac{d}{2}\right)^2} + \left(\frac{d}{2}\right)^2$$

$$= d^2 + r^2 + d\sqrt{r^2-\left(\frac{d}{2}\right)^2}$$

$$x_4 = \sqrt{d^2 + r^2 + d\sqrt{r^2-\left(\frac{d}{2}\right)^2}} = r\sqrt{\left(\frac{d}{r}\right)^2 + 1 + \frac{d}{r}\sqrt{1-\left(\frac{d}{2r}\right)^2}}$$

To simplify the expression, let $x = \frac{d}{2r}$

$$x_1 = r\left(\sqrt{1-x^2} - x\right)$$

$$x_2 = r\left(\sqrt{1-x^2}+x\right)$$

$$x_3 = r\sqrt{(2x)^2+1-2x\sqrt{1-x^2}} = r\sqrt{4x^2+1-2x\sqrt{1-x^2}}$$

$$x_4 = r\sqrt{4x^2+1+2x\sqrt{1-x^2}}$$

Using Taylor series expansion,

$$\frac{1}{x_1} \approx \frac{1}{r}\left\{1+x+\frac{3}{2}x^2+2x^3+\frac{23}{8}x^4+O(x^5)\right\}$$

$$\frac{1}{x_2} \approx \frac{1}{r}\left\{1-x+\frac{3}{2}x^2-2x^3+\frac{23}{8}x^4+O(x^5)\right\}$$

$$\frac{1}{x_3} \approx \frac{1}{r}\left\{1+x-\frac{1}{2}x^2-4x^3-\frac{49}{8}x^4+O(x^5)\right\}$$

$$\frac{1}{x_4} \approx \frac{1}{r}\left\{1-x-\frac{1}{2}x^2+4x^3-\frac{49}{8}x^4+O(x^5)\right\}$$

$$U = \frac{q_1q_2}{4\pi\varepsilon_0}\left(\frac{1}{x_1}-\frac{1}{x_2}-\frac{1}{x_3}+\frac{1}{x_4}\right) \approx \frac{q_1q_2}{4\pi\varepsilon_0 r}(12x^3)$$

$$U \approx \frac{q_1q_2}{4\pi\varepsilon_0 r}12\left(\frac{d}{2r}\right)^3 \approx \frac{\left(\frac{3}{2}\right)dq_1dq_2d}{4\pi\varepsilon_0 r^4} \approx \frac{\left(\frac{3}{2}d\right)p_1p_2}{4\pi\varepsilon_0 r^4}$$

Where $p_1 = q_1d$ and $p_2 = q_2d$. $p_{1,2}$ refers to the dipole moment of 1 and 2 respectively.

E: Relation between energy difference and wavelength difference

$$E = \frac{hc}{\lambda}$$

$$\frac{\partial E}{\partial \lambda} = -\frac{hc}{\lambda^2}$$

$$\partial\lambda = -\frac{\lambda^2}{hc}\partial E$$

When $\boldsymbol{\partial E}$ decreases, $\boldsymbol{\partial \lambda}$ decreases as well.